

UNIVERZITA KARLOVA
PŘÍRODOVĚDECKÁ FAKULTA

Studijní program:

Biologie

Studijní obor:

Buněčná a vývojová biologie – fyziologie buňky



Bc. Jan Majer

Dynamika modifikovaných diamantových nanokrystalů v živých buňkách

Dynamics of modified diamond nanocrystals in living cells

Diplomová práce

Školitelka: RNDr. Lenka Libusová, Ph.D.

Konzultant: Mgr. Petr Cígler, Ph.D.

Praha, 2019

Prohlášení:

Prohlašuji, že jsem závěrečnou práci zpracoval samostatně a že jsem uvedl všechny použité informační zdroje a literaturu. Tato práce ani její podstatná část nebyla předložena k získání jiného nebo stejného akademického titulu.

V Praze, 29. 4. 2019

Podpis:

Jan Majer

Abstract

Nanodiamonds (NDs) are an interesting platform in biological applications and disease treatment. Because of their photoluminescence properties and modifiable surface, they have been investigated as potential carriers for drugs and nucleic acids as well as fluorescent probes. In order to design NDs meeting specifically desired parameters, which would succeed in clinical trials and in medicinal therapy, understanding the mechanism of uptake and intracellular fate of NDs is crucial. The diploma thesis is focused on mechanistic investigation of ND-based nanoparticles delivering nucleic acids to human cells. First, NDs coated with a novel cationic co-polymer were prepared. NDs were then complexed with siRNA in order to transfect siRNA inside U-2 OS cells. NDs proved to be biocompatible and effective transfection particles as observed by qPCR and colorimetric cytotoxicity and cell viability tests. To examine ND uptake by cells, we inhibited endocytosis by specific inhibitors. Obtained results implicated that ND uptake was clathrin- and caveolin dependent. Nonetheless, more than half of NDs was internalized by cells in a different fashion. Some NDs colocalized with early endosomes, lysosomes and caveolin-derived endosomes after internalization. Other NDs resided either in unknown cell structures or escaped from endosomes to cytoplasm early after cell entry. In this work, we deepened our knowledge about NDs' cell uptake and their consecutive subcellular localization.

Abstrakt

Nanodiamanty (ND) jsou zajímavý nástroj, který nalézá uplatnění v biologii a v léčbě chorob. Jsou zkoumány pro svůj potenciál v doručování léčiv, nukleových kyselin a zároveň pro využití jako fluorescenční sondy na základě jejich modifikovatelného povrchu a fotoluminiscenčních vlastností. Objasnění mechanismu vstupu a intracelulárního osudu ND je stěžejní pro navržení ND, které mohou uspět v klinických studiích a v medicínské terapii. Tato práce se zaměřuje na mechanistické zkoumání nanočástic na bázi ND, které vnášejí nukleové kyseliny do lidských buněk. ND byly nejdřív obaleny vrstvou nově vyvinutého kopolymeru. Poté byla na ND navázána siRNA pro transfekci buněk U-2 OS. Získaná data z qPCR a kolorimetrických testů cytotoxicity a viability prokazují, že ND jsou biokompatibilní a efektivní transfekční částice. Specifické inhibitory endocytózy byly použity ke zkoumání mechanismu vstupu ND do buněk. Výsledky naznačují, že ND vstupují do buněk klatrinovou a kaveolinovou endocytózou. Nicméně více než polovina ND vstoupila do buněk jiným způsobem. Některé ND po vstupu do buňky kolokalizovaly s ranými endozómy, lysozómy a kaveolinovými endozómy. Ostatní ND se buď vyskytovaly v neidentifikovaných buněčných strukturách, nebo již v rané fázi po vstupu do buňky unikly z endozómů do cytoplazmy. Touto prací jsme prohloubili naše znalosti vstupu ND do buněk a jejich následné vnitrobuněčné lokalizaci.

Table of content:

1. Introduction: Put Nano in medicine	2
1.1. <i>An Ideal Nanoparticle for cell uptake</i>	2
1.2. <i>Nanodiamond properties</i>	5
1.2.1. Methods of preparation	6
1.2.2. Bright nanodiamonds	6
1.3. <i>Surface modifications</i>	8
1.3.1. Modifications towards cell specific targeting	9
1.4. <i>Nanodiamonds in the context of the living system</i>	10
1.4.1. Nanodiamonds <i>in vitro</i>	10
1.4.2. Nanodiamonds <i>in vivo</i>	11
1.5. <i>Endocytosis</i>	12
1.5.1. Clathrin-mediated endocytosis	13
1.5.2. Caveolae-mediated endocytosis	15
1.5.3. RNA interference and siRNA delivery	16
2. Study aims	19
3. Materials & methods	20
3.1. <i>Materials, solutions & buffers</i>	20
3.2. <i>Methods</i>	24
3.2.1. Surface silication	24
3.2.2. Surface polymerization	24
3.2.3. Gravimetry	25
3.2.4. ND:siRNA complex preparation	25
3.2.5. Particle diameter determination and ζ -potential	25
3.2.6. Free siRNA determination after ND:siRNA complexation	26
3.2.7. Human cell line culture	26
3.2.8. qPCR experiments	27
3.2.9. Cytotoxicity and proliferation assays	28
3.2.10. Endocytosis inhibition samples and time series samples	29
3.2.11. Immunofluorescent labelling	30
3.2.12. Microscopy	31
3.2.13. Microscopy image analysis	31
4. Results	32
4.1. <i>ND surface polymerization and characterization</i>	32
4.2. <i>ND:siRNA complex stability</i>	33
4.3. <i>Quantitative PCR</i>	34
4.4. <i>Cytotoxicity</i>	36
4.4.1. Nanodiamond endocytosis mechanism determination	37
4.4.2. Uptake and intracellular localization of ND:siRNA complexes	42
5. Discussion	52
5.1. <i>Transfection efficiency of NDs</i>	53
5.2. <i>Impact of NDs on cell physiology</i>	53
5.3. <i>Uptake mechanism</i>	54

5.3.1.	Clathrin-mediated endocytosis	55
5.3.2.	Caveolin-mediated endocytosis	56
5.4.	<i>Uptake rate and colocalization with intracellular structures</i>	56
5.5.	<i>Colocalization of NDs with siRNA: siRNA release</i>	60
6.	Conclusions	62
7.	Bibliography	64
8.	Supplementary data	74

List of abbreviations:

AIBN:	2,2'-azobis(2-methylpropionitrile)
Arp2/3:	Actin-Related Proteins 2 and 3
CALM:	Clathrin Assembly Lymphoid Myeloid Leukemia protein
Cav:	Caveolin
CavME:	caveolin-mediated endocytosis
CME:	clathrin-mediated endocytosis
CNT:	carbon nanotubes
ddH ₂ O:	distilled, deionized water
DLS:	diffraction light scattering
DMAEMA:	o 2-dimethylaminoethyl methacrylate
DMEM:	Dulbecco Modified Eagle Medium
DNA:	deoxyribonucleic acid
DND:	detonation nanodiamond
EHD:	Epsin Homology Domain
FA:	folic acid
GAG:	glycosaminoglycan
GMF:	glass microfiber filter
GOP:	graphene particles
GTP:	guanosinotriphosphate
HPHT:	high pressure, high temperature
HPMA:	N-(2-hydroxypropyl)methacrylamide
LB:	lysogeny broth
LDH:	lactate dehydrogenase
MLS:	mitochondria localizing signal
mRNA:	messenger ribonucleic acid
MSB:	microtubule stabilizing buffer
ND-Tf:	transferrin-conjugated nanodiamond
NIR:	near-infra-red
NP:	nanoparticle
NT siRNA	non-targeting siRNA
N-V:	Nitrogen-Vacancy
PBS:	phosphate buffer saline
PCC:	Pearson's Correlation Coefficient
PEG:	polyethylene glycol
PI(4,5)P ₂ :	phosphatidylinositol-4,5-bisphosphate
PVP:	polyvinylpyrrolidone
RNA:	ribonucleic acid
RNP:	ribonucleoprotein
ROS:	reactive oxygen species
SH3:	SRC homology 3 domain
siRNA:	small interfering ribonucleic acid
SOB:	super optimal broth
TEOS:	tetraethylorthosilicate
TMSPMA:	3-(trimethoxysilyl)propylmethacrylate
VS:	VectaShield
WASP:	Wiskott-Aldrich Syndrome Protein
WST-1:	Water Soluble Formazan 1

1. INTRODUCTION: PUT NANO IN MEDICINE

Nanotechnology has been commonly used in pre-modern era. For example cathedral windows across Europe owe gold chlorides for their vibrant and lasting colours (Rubio, 2015). This was achieved by empirical understanding and exploiting of material manipulation – heating commonly. In the 70's, we understood that plasmon resonance is the catalyst of this phenomenon (Cunningham *et al.*, 1974). Today, nanotechnology is undergoing a rapid expansion in various scientific fields and domains and in 2016, nanomachines brought Nobel Prize to researchers who studied and created simple molecular motors on submicronic scale.

Now, nanoparticles (NPs) in context of medical therapy already achieved effective drug delivery abilities. Criteria for approving a novel drug delivery platform are strict and rightfully so. NPs exhibit remarkable transfection and drug delivery properties, meaning that they are often used to transport nucleic acids (DNA, RNA) into cells. Additionally to just transporting aforementioned cargo, NPs can be utilized as fluorescent tags, mediate steady cargo release, act against exocytosis of drugs and more (Fang *et al.*, 2011; Lee *et al.*, 2009; Petrakova *et al.*, 2016; Wang *et al.*, 2015). To implement nanoparticles in medicinal therapy, their chemical and physical properties as well as their dynamics in living organisms should be understood to full extent in order to avoid unwanted and cytotoxic side-effects and *vice versa* to utilize some desirable properties such as, increase in drug half-life, enhanced permeation and retention, reduced cytotoxicity, imaging possibilities and targeting.(Castan *et al.*, 2018; Maeda, 2001; Petros and DeSimone, 2010; Zhao *et al.*, 2014)

1.1. An Ideal Nanoparticle for cell uptake

NPs exhibit vast potential in therapy and are in the spotlight because of their modularity and multiple exploitable properties which would allow us to tailor therapy to measure. NPs include lipid-based NPs (liposomes, micelles) (Itaka *et al.*, 2003; Spagnou *et al.*, 2004), cationic nanopolymers (Fox *et al.*, 2009), inorganic nanoparticles (Au, Ag, Fe, Si) (Boyer *et al.*, 2009; Gerion *et al.*, 2007; Lee *et al.*, 2009; Roh *et al.*, 2009), and carbon-based structures (nanodiamonds, nanotubes) (Karlsson *et al.*, 2008; Neburkova *et al.*, 2018).

As it was mentioned above, NPs withhold a great potential in carrying drugs (e. g. doxorubicin) and nucleic acids in order to treat a disease. Herein, the focus is specifically set on DNA and RNA transfection. Now, there is a multitude of methods to transport DNA and many forms of RNA and RNP molecules into the cell. However, most of these tools are limited by factors such as their target specificity, their overall toxicity and their ability to protect the cargo in “hostile” environment (e. g. mononuclear phagocyte system and omnipresent nucleases) in organisms. Commercially available lipid-based NPs and those made of polymer have become a standard in the field of transfection. However, these are often considered toxic. Nevertheless, some polymer-based transfection reagents, such as commercially available polyethylenimin (PEI), already overcame this hurdle (Yamano *et al.*, 2010).

Both organic and inorganic NPs are promising and the research on relationship between NP's properties and their therapeutic use and role in transfection are ever-growing.

For instance, lipid nanoparticles demonstrated interesting results in transfection in non-human primates and in clinical trials, too. Also, they were observed in receptor-mediated endocytosis (Frank-Kamenetsky *et al.*, 2008; Gilleron *et al.*, 2013). Polymer-based nanoparticles excel in the myriad of functions which can be achieved through well designed sizes and structures, lengths and branching of polymers (Andonova, 2017; Fox *et al.*, 2009). An undeniable advantage of organic NPs is their biodegradability and therefore there is no need for taking exocytosis into account in their design (Garbuzenko *et al.*, 2014).

Inorganic NPs, such as iron oxide NPs, silica NPs and nanodiamonds are all resistant to enzymatic degradation and their surfaces can be modified with polymers. Furthermore, they have interesting optical and electromagnetic properties (Boyer *et al.*, 2009; Neburkova *et al.*, 2018). Iron oxide NPs are utilized in magnetofection, which uses magnetic field to concentrate NPs on a cell membrane, easing NPs' uptake with the siRNA (Kim *et al.*, 2017). However, inorganic NPs are not biodegradable, therefore cell eventually release NPs through exocytosis or NPs remain stored inside the cells.

Nanoparticle's diameter is a crucial parameter. It was discovered that an uptake rate of a nanoparticle can vary within the range of 30 – 280 nm significantly. It is rational

to expect that deliberate size calibration leads towards variable uptake rates. Indeed, Ryu *et al.* proved that 50 nm NP diameter is ideal to achieve the highest cell uptake rate. It is more than two times higher in comparison to 100 nm large particles (Ryu *et al.*, 2017).

Mechanisms of interaction with cells are highly dependent on NP shape. Zheng *et al.* compared the process of internalization of differently shaped nanodiamonds (NDs) which are carbon-based NPs. They discovered that both the “prickly” (with sharp edges) and the round (etched prickly) NDs exhibit similar abilities to anchor onto the membrane. Interestingly, the rounded NDs exhibited higher ability to be internalized by the cell membrane. After computational modelling, Zheng *et al.* proposed that this is a result of higher energy penalty as the membrane curvature around the prickly NP requires more free energy and thus generates an energy penalty, favouring the rounded shape of NPs (Zhang *et al.*, 2017).

Interestingly, one study suggests that prickly shape of the nanoparticle enhances its ability to escape from the endosomes by punctuation of endosomal membranes. Chu *et al.* compared the endosomal escape of prickly and round silica nanoparticles and prickly and round NDs. They proposed and verified that round nanoparticles tend to stay inside of a vesicle and prickly particles escape the endosomes early on, before they reach lysosomes (Chu *et al.*, 2015).

Moreover, Hinde *et al.* compared various shapes of polymeric nanoparticles. Elongated rod- and worm-like shaped NPs were detected in the nucleus whereas, micelles and vesicular NPs were not. If they were observed in nucleus, they probably did not pass through nuclear envelope by diffusion, but during the nucleus division. During this process, nuclear lamina breaks down (Georgatos *et al.*, 1997) and stops preventing these particles to pass through. Furthermore, all shapes passed the cell membrane similarly through diffusion and through ATP-mediated endocytosis. All NPs were localized in early endosomes and rod-like shaped NPs in late endosomes (Hinde *et al.*, 2017).

In contrast to Hinde *et al.*, there was no report on significant difference in shape-dependent endosomal escape (Hinde *et al.*, 2017). Of course, this difference in their findings is plausible since nanoparticle dynamics in cells vary drastically depending on their size, shape, surface modification, material, cell line and its environment (Chu *et al.*, 2015; Ryu *et al.*, 2017; Zhang and Monteiro-Riviere, 2009).

In order to interact with the cell surface, an ideal nanoparticle should have a positive charge in order to move to and interact with negatively charged cell membrane. Indeed, positively charged NPs exhibited higher uptake (Harush-Frenkel *et al.*, 2007). However, in another study, the NP uptake was inversely in favor to negatively charged particles. It is noteworthy to mention, that negatively charged nanodiamonds were a few nanometers in size and thus different mechanisms and dynamics of cell membrane interactions could take place (Zhang and Monteiro-Riviere, 2009).

Secondly, the particle's surface charge is a major influence on its colloidal stability since the particles require to have sufficient repulsive interaction between each other. Otherwise the particles aggregate and render themselves unfit for therapeutic use (Gibson *et al.*, 2009; Havlik *et al.*, 2016; Zhang *et al.*, 2015; Zheng *et al.*, 2017).

1.2. Nanodiamond properties

NDs are exceptional carbon-based NPs with unmatched physical properties, such as the highest hardness and thermal conductivity (Jagannadham *et al.*, 2014; Rao *et al.*, 1997; Shenderova *et al.*, 2006b). Owing to their biocompatibility, low particle core chemical reactivity, variety of surface chemistry modifications and favorable fluorescence properties (Turcheniuk and Mochalin, 2017), NDs were already exploited as sensors of external magnetic resonance or temperature (Acosta *et al.*, 2010; Balasubramanian *et al.*, 2009) and as drug delivery platform (Huang *et al.*, 2007).

A myriad of experiments on ND-mediated cytotoxicity reached a consensus that NDs exhibit high biocompatibility properties both *in vitro* and *in vivo*. When compared with other nanoparticles, including other carbon-derived NPs (e. g. nanotubes), NDs exhibit the lowest cytotoxicity even after a long-term incubation (Lin *et al.*, 2016; Yuan *et al.*, 2010; Zhang *et al.*, 2012).

A well-known drawback regarding NDs is their tendency to aggregate into large clusters (Lee *et al.*, 2012). When sufficiently charged NDs are dissolved in water, they remain colloidally stable. On the other hand, when NDs are in a buffer and growth medium, oppositely charged ions in the solutions adhere to the ND surface based on their attractive electrostatic forces. This causes masking of NDs' surface charge. Therefore, electrostatic repulsive forces between ND particles decrease which may cause aggregates

formation. Therefore, the hydrodynamic diameter of the particle increases. This effect severely hinders NDs potential to be taken up by the cell (Hemelaar *et al.*, 2017).

1.2.1. Methods of preparation

Today, manufacturing of NDs is affordable and can be done by three approaches. First approach in creating NDs is through detonation of a mixture of hexogen and trinitrotoluene (Shenderova *et al.*, 2006a). This method delivers <10 nm particles. These NDs, however, have a propensity to cumulate defects and higher amount of metallic impurities in the structure of an ND lattice (Stehlik *et al.*, 2015). Second method is called chemical vapour deposition (CVD). During CVD, the carbon atoms contained in a gaseous form crystallizes on a specific substrate and creates a ND film (Gracio *et al.*, 2010). Lastly, nanodiamonds can be manufactured under high pressure and high temperature (HPHT). Although HPHT NDs were larger in diameter, recently, a significant size reduction was already achieved (<10 nm) (Stehlik *et al.*, 2015). Manufactured NDs' surface is commonly covered by graphene and further metallic and organic impurities (Pichot *et al.*, 2008). Therefore, ND clusters occur as there are non-sufficient repulsive forces present between the particles. It is necessary to remove these impurities, often done by oxidation of the ND surface in either acidic environment or heated to ~500°C with air access (Havlik *et al.*, 2016). Once this process is finished, the surface of an ND is covered by negatively charged groups (e. g. carboxyls). These groups partake in colloidal stability of the particle as they create a negative charge. Moreover, these charged groups can be then targeted for further chemical modifications (Schrand *et al.*, 2009).

1.2.2. Bright nanodiamonds

NDs are extensively utilized as fluorescent probes in living organisms since they exhibit remarkable optical properties. Upon laser excitation (approx. 520–550 nm) a fluorescence signal is emitted from ND fluorescence centers, which are irregularities in ND's crystal structure. These centers are scattered throughout the nanodiamond. The emitted wavelength begins at ~ 600 nm with a peak at ~ 700 nm wavelength and reaching into the far-red spectra. The near-infrared wavelength emission makes NDs favorable because cells' autofluorescence signal in this area of light spectrum is reduced (fig. 1a) (Petrankova *et al.*, 2016).

Fluorescence centers are called Nitrogen–Vacancy (N–V) centers. Vacancy is a carbon atom lacking position in the ND lattice. Nitrogen is a rare impurity. It is deposited in the lattice during the ND manufacturing. The amount of these lattice irregularities is scarce and to achieve enough electromagnetic signal, NDs are firstly irradiated. Irradiation generates significantly more vacancies in the lattice. During this process, NDs are targeted by so called “light ions.” These are high-energy protons (H^+) (Stursa *et al.*, 2016) and α particles (He^{2+}) (Waldermann *et al.*, 2007). Moreover, NDs can be irradiated with electrons and neutrons (Boudou *et al.*, 2009; Nöbauer *et al.*, 2013). Light ions are

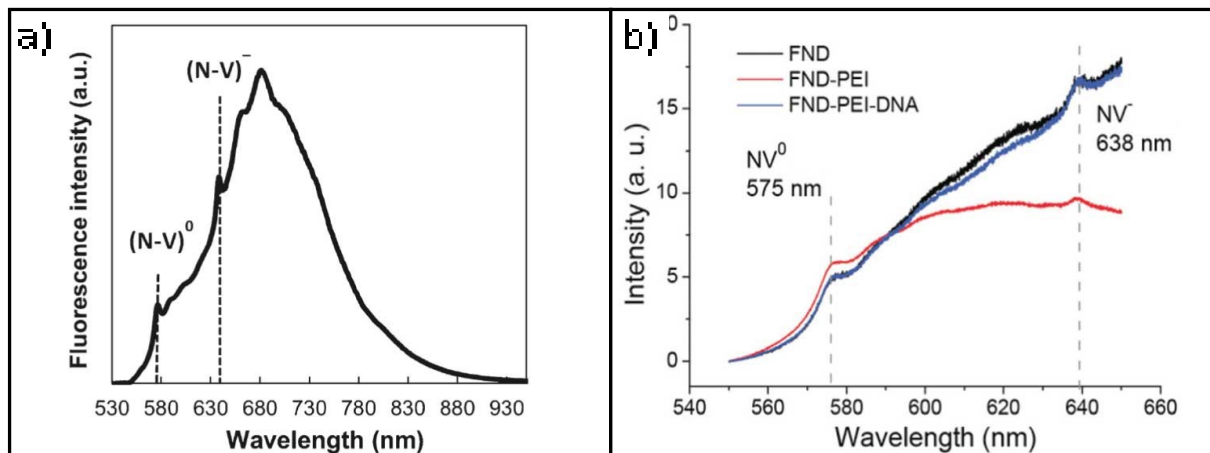


Figure 1: Fluorescent nanodiamond intensity spectra. a) Spectrum of NDs (Neburkova *et al.* 2018). b) Switch in NV⁰ – NV⁻ intensity ratio depending on surrounding charge of molecules. PEI = cationic, DNA = anionic (Petrankova *et al.* 2016).

preferred as they exhibit higher range of material penetration while being less destructive than heavier particles. Secondly, NDs undergo thermal annealing. During this process, these vacancies are moved through the ND crystal lattice until the vacancy meets and anneals with the nitrogen impurity. This process takes place in harsh conditions of approximately 800°C under inert gas (Ar) (Havlik *et al.*, 2016, 2018; Stursa *et al.*, 2016).

Because of their fluorescent properties, NDs function as probes. N–V centers occupy two different states – neutrally charged N–V⁰ and negatively charged N–V⁻. Depending on electrochemical properties of molecules in vicinity of each of NDs N–V center, the center changes to or remains in one of the afore-mentioned two states. This phenomenon manifests itself by specific offset in photoluminescence spectra. At 575 nm (N–V⁰) intensity approximately the same. On the other hand, intensity fluctuates at 638 nm (N–V⁻) depending on the properties of neighboring molecules (fig. 1b). These offsets can be spectroscopically visualized as true emission colors switch between “orange” and

NIR spectrum maxima. This would allow to observe real-time dissociation of cargo transported into the cell by NDs (Petrakova *et al.*, 2015, 2016; Wee *et al.*, 2007).

NDs are difficult yet feasible to visualize. To their advantage, NDs are not susceptible to photobleaching and photoblinking in contrast with today's routinely used organic fluorescent probes, making them an interesting tool in fluorescent labelling. Although their broad use is hindered by their low brightness (Havlik *et al.*, 2013; Stursa *et al.*, 2016), NDs NIR fluorescence emission ranges in light spectrum, where cellular autofluorescence is minimal (Cordina *et al.*, 2018).

1.3. Surface modifications

The multitude of options of chemical surface modifications allow drastic changes of the behavior and the fate of NDs by ligand-coupling. Furthermore, NDs can be coupled with fluorescent tags, a plethora of hydrophobic and hydrophilic molecules, such proteins, polymers, nucleic acids and ligands through surface modifications.

NDs exhibit broad amount of reactive residual groups, such as hydrogen, hydroxyl, carboxyl, epoxide, anhydride, alkene, anhydride, aldehyde, C-Cl, C-F and ketone groups and more, as researchers reviewed comprehensively (Mochalin *et al.*, 2012; Schrand *et al.*, 2007; Turcheniuk and Mochalin, 2017). Such groups represent targets for well-known chemical reactions to achieve desired chemical, colloidal and biocompatibility behavior. Meaning they are coated by various methods to obtain high yield surface modifications and extended stability in living systems. For example, silica coating was reported to enhance the yield of the subsequent chemical modifications through creating further locations for new moieties to covalently attach (Jana *et al.*, 2007).

Furthermore, under substantially extreme conditions (annealing at >900 °C), shell of graphene can be created. Graphene shell is then arylated and as such, NDs exhibit low propensity to re-aggregate (Liang *et al.*, 2011). Similarly, polyethylene glycol (PEG) shell is often used to dampen the adsorption processes of serum protein, salts and acids and thus preventing the aggregation of particles into clusters.

Finally, to prevent collapse of stable colloidal NDs, a recent study showed that introduction of NDs into full serum suspension coats and stabilizes the NDs in full serum medium (Hemelaar *et al.*, 2017).

1.3.1. Modifications towards cell specific targeting

Vascular Endothelial Growth Factor (VEGF) and other factors of hypoxic cancer cells induce angiogenesis in order to reach O_2 , release CO_2/HCO_3^- and lower both their environmental and intracellular pH. Such neovascular endothelium is susceptible to permeate small particles through. Their passage is made possible because this newly created tissue can be atypical and fenestrated. Permeation and retention of nanoparticles in neoendothelial is called enhanced permeability and retention effect (EPR). It has been firstly described in the 80s' (Matsumura and Maeda, 1986) and it is the main driving force of non-specific tumour targeting by NPs (Maeda, 2001; Maeda *et al.*, 2013; Nichols and Bae, 2014). A recent study suggests NDs induce further endothelial vascular leakiness and enforce further vascular permeability of the vasoendothelium in tumours. The leaking is generated by an increase in intracellular reactive oxygen species and Ca^{2+} . Therefore, the ND-mediated EPR could significantly assist in nanocarrier effectivity *in vivo* (Setyawati *et al.*, 2016).

According to Wilhelm *et al.* only 0.7% of nanoparticles find their way into the observed targeted sites (Wilhelm *et al.*, 2016). In order to maximize the rate of successful ND delivery, the research focuses also on specific targeting.

Many viruses are structurally simple and yet, they have a wide spectrum of antigens which bind to specific structures, such as cell membrane receptors and extracellular structures. Such modifications allow viruses to enter the cell in a highly specific manner and take an advantage of the host cells' endocytosis system and intrinsic transport pathways to reach their position of effect. Therefore, mimicking the viral antigens and coupling them with nanoparticles is a reasonable research pursuit in order to achieve cell specific transport system for *in vivo* drug and nucleic acid trafficking. Recently, such ND conjugated with virus envelope proteins were utilized to achieve specific ND binding (Pham *et al.*, 2017).

Apart from viral structures, cell specific binding can be achieved through binding of transferrin. Transferrin with transferrin receptors are a well-studied, widely used model system (Rodal *et al.*, 1999; West *et al.*, 1989). Conjugation of NDs with transferrin (ND-Tf) results in significantly higher uptake of the particles by cancer tissue in contrast to the normal cells. This is logical, since cancer cells exhibit larger amount of Tf receptors

in comparison with normal mammalian cells (Wang *et al.*, 2015). The exact same tactic can be used to target other cell specific receptors such as, CD44 and CD55 (Chang *et al.*, 2013) and folic acid (FA) receptor (Chan *et al.*, 2017).

In order to further increase the carrying capacity of NDs beyond cell membrane, ND's surface can be modified by specific organelle targeting molecules. Such a molecule can be a well-known intrinsic targeting peptide Mitochondria Localization Sequence (MLS). Exploiting the combination of attaching both FA and MLS peptide to the ND resulted in cancer specific ND uptake as well. Additionally, ND were observed in mitochondria. These modifications lay foundations to novel methods in drug delivery through highly specific pinpointing of desired organs, tumours, cells, and organelles of interest (Chan *et al.*, 2017).

1.4. Nanodiamonds in the context of the living system

1.4.1. Nanodiamonds *in vitro*

Since NDs are facing utilization in therapy, toxicity data is necessary to evaluate their safety in potential clinical and general use. NDs stand out among carbon nanoparticles with their low cytotoxicity. When NDs are compared with graphene oxide particles (GOPs) and carbon nanotubes (CNTs), NDs exhibit significantly greater ability in the context of cellular uptake while maintaining the lowest cytotoxic effect (Zhang *et al.*, 2012).

NDs were observed for example in the cytoplasm, lysosomes, even in mitochondria. However, high dose of NDs increases cytotoxicity, although still, this adverse effect exhibits itself in NDs incubation the least in comparison with other NPs. This has been proven by MTT and WST-1 assays, both of which are being broadly exploited colorimetric tests assessing cell's metabolic activity (Zhang *et al.*, 2012). In addition, introduction of NDs to cells do not cause reactive oxygen species (ROS) related genes upregulation (Hemelaar *et al.*, 2018).

Reports of carbon NPs induced cytotoxicity exist, too. Periasamy *et al.* claims the NDs, CNTs and GOPs (or black dots) greatly reduce the cell viability in human mesenchymal stem cells. Although, it is unclear which of the three mentioned carbon NPs

are being assessed since the particles are labelled and referred to as carbon NPs throughout the entire article (Periasamy 2016).

Moreover, NDs induce DNA repair mechanisms based on observations of p53 phosphorylation and increased gene expression of Rad51, MGG1 and XRCC-4 which point out to DNA damage (Rim *et al.*, 2013; Xing *et al.*, 2011).

The abovementioned cytotoxic effects are possibly the result of different cell lines, type, surface properties, and shape of NDs (Chu *et al.*, 2015; Hemelaar *et al.*, 2018; Hinde *et al.*, 2017). These factors play crucial roles in interaction between a cell and a ND. Commonly, the cytotoxicity of ND is evaluated as non-toxic in consensus with the results of Zhang *et al.* and across various cell lines (Petrankova *et al.*, 2016; Schrand *et al.*, 2007; Zhang *et al.*, 2012).

1.4.2. Nanodiamonds *in vivo*

Cytotoxicity and viability analysis only scope the adverse effects of NDs in an extent of cell and tissue cultures. Effects of NDs *in vivo* can be significantly different. For example, retention and internalization of NDs were observed in lungs, spleen, kidney, pharynx, and liver in murine models.

Moore *et al.* discovered that although NDs accumulate predominantly in liver tissue, liver's functionality remains intact. Interestingly, NDs remain in both blood and urine samples, days after their administration without significant raise in white blood cell count. Furthermore, NDs cause no inflammatory, toxic, and coagulant responses in murine models. NDs do not affect red blood cells oxygenated and deoxygenated state and the transition in between the states and renal system remains normally functioning as well. (Moore *et al.*, 2016; Tsai *et al.*, 2016).

Size and shape of NDs are reported as significant factors in organ-specific accumulation. Rojas *et al.* and Yuan *et al.* conducted filtration of particle aggregates prior to administration. This caused lower number of internalized particles residing in the spleen and lungs. Correlation between ND size and organ specific accumulation was suggested (Rojas *et al.*, 2011; Yuan *et al.*, 2010).

Furthermore, injecting ND solution into multiple areas of mice (Yuan *et al.*, 2010) and rats (Rojas *et al.*, 2011; Vaijayanthimala *et al.*, 2012) demonstrated no notable inflammatory reaction. Interestingly however, NDs engulfed by macrophages in the alveolar were reported migrating into pharynx, where they amassed (Yuan *et al.*, 2010).

Apart from murine models, a recent study was conducted on monkey models and showed promising and corresponding data to already conducted murine-model experiments (Moore *et al.*, 2016).

However, experiments in *Xenopus* (Marcon *et al.*, 2010) and in *Danio* (Lin *et al.*, 2016) models suggest teratogenic effects in early development stages. Interestingly, these adverse effects caused by NDs could be exploited in order to reduce blastoma invasivity (Wierzbicki *et al.*, 2017) and reduce angiogenesis (Grodzik *et al.*, 2011; Wierzbicki *et al.*, 2013).

Acquiring complete knowledge of the risks and advantages of ND use in organisms requires rigorous testing. Recent reviews put together comprehensive tables of already examined applications with respect to the aforementioned parameters (Tinwala and Wairkar, 2019; Turcheniuk and Mochalin, 2017).

1.5. Endocytosis

Cell membrane is a vital lipid-based barrier which protects the cell content from the harsh extracellular environment. Cell membrane is impassable for charged and large molecules. To facilitate passage of large molecules, the process of transport through the plasmatic membrane, inside the cell requires energy. Actually, high amount of free energy is necessary to utilize membrane invagination (Zhang *et al.*, 2017), encapsulation and ultimately pinching off of a membrane vesicle containing the molecule (Thomsen *et al.*, 2002).

Cells use process called endocytosis for uptake of myriad of nutrients, signaling molecules and growth factors and they utilize different uptake mechanisms, depending on the cell type and type of engulfed cargo. Although the number of internalization mechanisms is large, early endosomes serve as crossroads through which every pathway leads (fig. 2). Early endosomes are responsible for sorting of all passing cargo and sending them for degradation on plasma membrane, degradation in acidic lysosomes or delivery to Golgi network system (Jovic *et al.*, 2010). Indeed, NDs were already observed in early endosomes and lysosomes (Prabhakar *et al.*, 2017; Schrand *et al.*, 2011). The most studied clathrin-mediated endocytosis (CME) was first observed in a mosquito oocyte through electron microscope more than 50 years ago (Roth and Porter, 1964). CME, and Caveolin mediated endocytosis (CavME), one of clathrin-independent endocytic (CIE) mechanisms (fig. 2), are discussed as main contributors of ND uptake (Lin *et al.*, 2017; Zhao *et al.*,

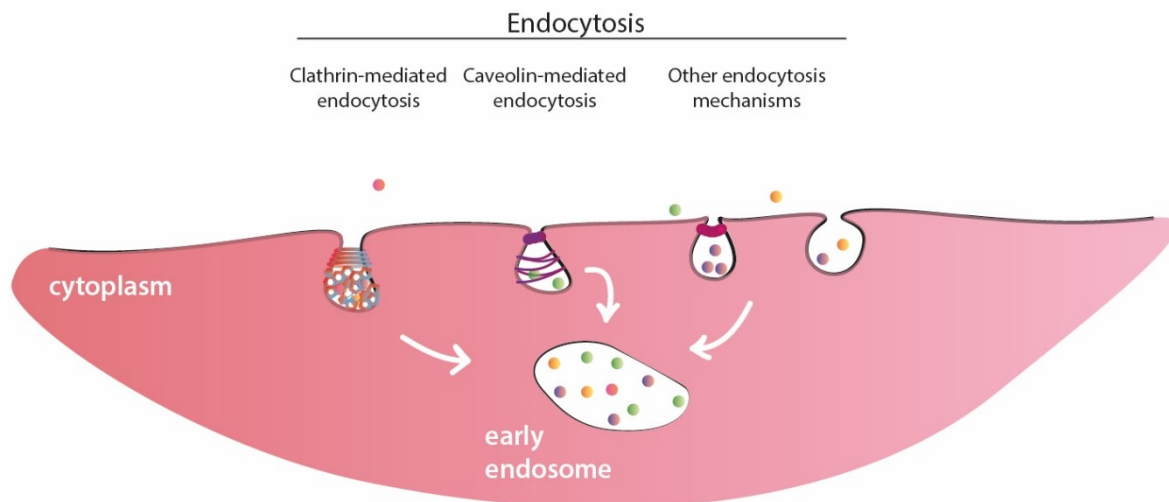


Figure 2: Overview of CME and CavME mechanisms (Conner and Schmid, 2003).

2017). Additionally, macropinocytosis was also reported as a contributor to ND uptake mechanism (Alhaddad *et al.*, 2012)

1.5.1. Clathrin-mediated endocytosis

Clathrin, is a monomer protein which creates a polygonal coat on an invaginated membrane on the intracellular side. Clathrin monomers merge into a triskelion structure. Triskelion consists of one heavy chain (~190kDa) and three light chains (~25kDa). These chains then interact between themselves and form pentagonal and hexagonal structures.

Polygonal shape of these structures hinders plane surface formation and promotes invagination of the cell membrane (Fotin *et al.*, 2004).

Firstly, specific cytosolic pool of proteins is recruited to form a clathrin coat on the

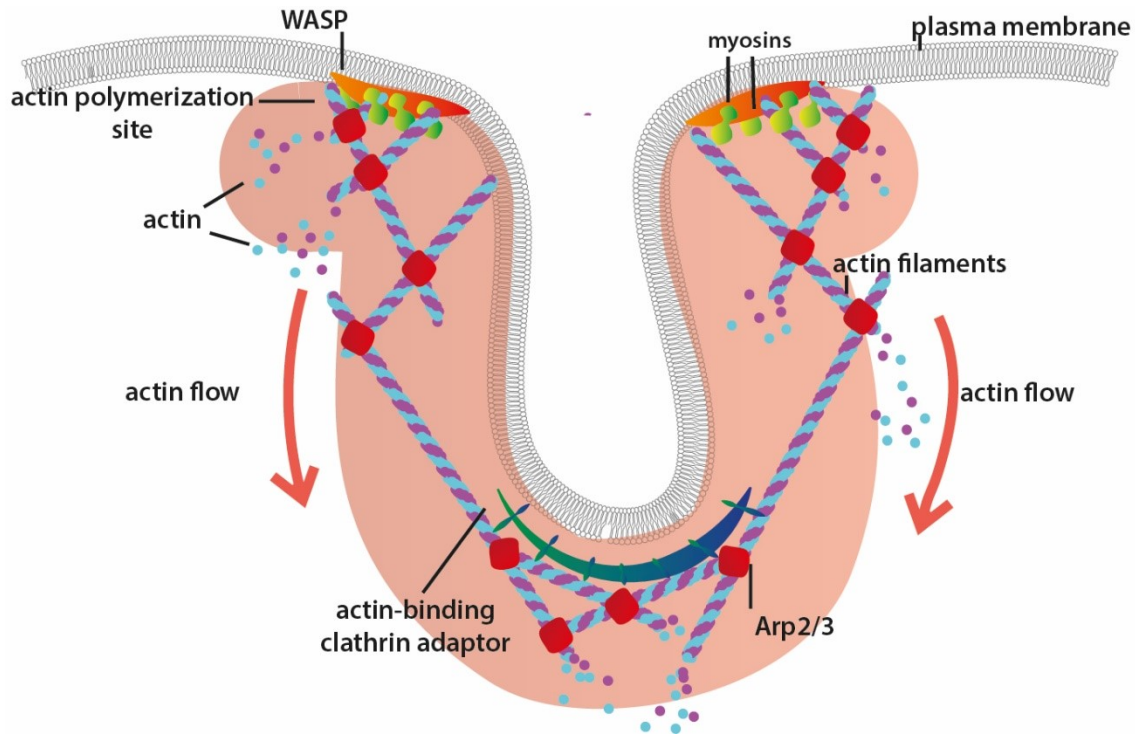


Figure 3: Clathrin pit elongation. Actin polymerizes in the vicinity of WASP. Actin filaments elongate along the vesicle neck, interacting with actin-binding clathrin adaptor. Arp2/3 branching point protein (Kaksonen and Roux, 2018).

cytosolic face of the membrane. Herein, the present proteins, apart from clathrin, are clathrin adaptor protein 2 (AP2) complex, Clathrin Assembly Lymphoid Myeloid Leukaemia protein (CALM), and a family of epsins. AP2 complex binds to phosphatidylinositol-4,5-bisphosphate (PI(4,5)P₂) on the membrane and changes its conformation. Clathrin is then recruited. CALM and epsins bind to the lipids of the membrane and to scaffold proteins which interact between each other and with clathrin to ultimately form a coat (fig. 3, Cocucci *et al.*, 2012; Ford *et al.*, 2002; Kadlecova *et al.*, 2017; Kaksonen and Roux, 2018; Miller *et al.*, 2015).

Once the coat is formed, actin polymerization takes place in the second module, also called “actin module.” Key proteins within this module (apart from actin) are myosin motor, Wiskott-Aldrich Syndrome protein (WASP), dynamin, and actin-related protein Arp2/3. WASP is an activator of actin nucleation. Arp2/3 protein is associated with branching points of actin filaments (Goode *et al.*, 2015; Sun *et al.*, 2006).

After cargo recruitment through cargo-binding membrane proteins, the invaginated membrane is bend and elongated further. Elongation process is a result of actin polymerization (fig. 3; Kadlecova *et al.*, 2017). Scission of the vesicle is canonically executed by dynamin. Dynamin is a ~100kDa GTPase, with lipid binding pleckstrin homology domain, GTP binding domain and a proline/arginine rich segment which binds SH3 domains of other proteins (Daumke *et al.*, 2014; Reubold *et al.*, 2015). Dynamin forms an oligomer around the neck of the prolonging neck of the invaginated to-be vesicle. Then, through hydrolysis, the dynamin initiates the fission of the vesicle from the donor membrane (Bashkirov *et al.*, 2008; Sweitzer and Hinshaw, 1998).

1.5.2. Caveolae-mediated endocytosis

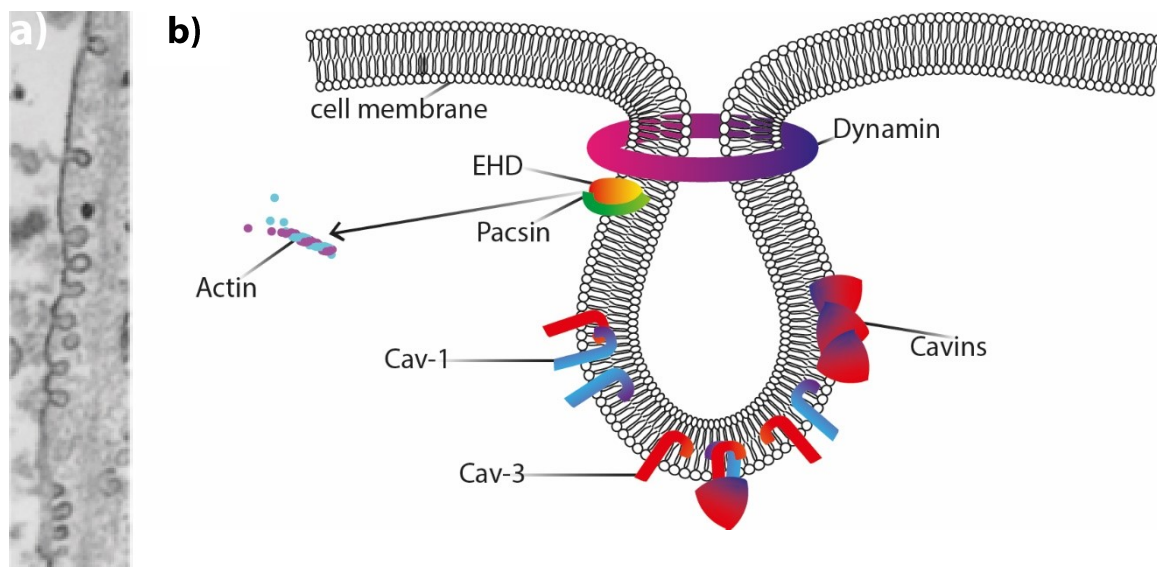


Figure 4: Caveolae structure. a) Membrane profile of TEM image of 3T3-L1 adipocytes.; b) Caveolae organization model. Cav-1 and -3 form scaffold around the curving membrane. Cavins partake in structure stabilization together with EHD which interacts with actin filaments. Dynamin is responsible for vesicle dissociation from cell membrane. (Echarri and Pozo, 2015).

Albumin is an abundant serum protein which cells ingest primarily through clathrin-independent, caveolae-mediated pathway (Chatterjee *et al.*, 2017). Caveolae are subdomains of lipid rafts, sequestering cholesterol and forming stable bulbs on the plasma membrane with cargo upper size limit reaching 80 - 100 nm (Rausch *et al.*, 2019; Wang *et al.*, 2009). Furthermore, unlike clathrin-coated vesicles which are formed dynamically in a short period of time, caveosomes have stable membrane architecture with distinctive neck region (fig. 4a) (Yeow *et al.*, 2017).

During caveolae pit formation, membrane-bound cholesterol binds to caveolin-1 (Cav-1) and Cav-3. Cav-1 can directly curve the membrane *in vitro*. *In vivo*, however caveolins require more partners to achieve membrane curvature. Cavins' presence is necessary for formation and stabilization of caveolae pits (Liu *et al.*, 2008). Cavins bind to PI(4,5)P₂ and phosphatidylserine in the membrane. Furthermore, EHD (Epsin 15 homology domain) proteins are utilized to keep a stable neck structure and to interact with actin filaments (Kostan *et al.*, 2014; Yeow *et al.*, 2017). Finally, pacsins take part in caveolae architecture and membrane bending too (fig. 4b, Seemann *et al.*, 2017). All the above-mentioned proteins have ability to create bumps in the membrane and *in vitro*, Cav-1 forms these caveolae without any other proteins present. In vertebrae, cooperation is necessary to achieve the same phenotype as *in vitro* experiments (Senju *et al.*, 2011).

Budding of the caveolae resolves into a endocytic vesicle. This vesicle contains both Cav-1 and cavins (Boucrot *et al.*, 2011). Dynamin divides caveolae buds from the plasma membrane (Stoeber *et al.*, 2012). The dissociated bud then re-merges with plasma membrane or it fuses with early endosomes in a Rab5 dependent activity (Pelkmans *et al.*, 2004).

To study endocytosis, inhibition of CME and CavME can be achieved through introduction of specific endocytosis-inhibiting drugs. Dynasore is often used as an inhibitor of CME. Dynasore affects two stages of the CME through yet unknown interaction with dynamin. Supposedly, inhibition is achieved when the clathrin-coated curvature structure reaches halfway (U-shape), just before the neck forms and also after full formation of the clathrin-coated vesicle (O-shape) (Macia *et al.*, 2006).

Inhibition of CavME can be achieved through introduction of Filipin, a sterol binding drug. Filipin binds and sequesters membrane cholesterol in the membrane raft regions. This causes the stable caveolae pits phenotype of the cell to diminish because there is no binding site for Cav-1 and associated proteins to interact with (Schnitzer *et al.*, 1994).

1.5.3. RNA interference and siRNA delivery

RNA interference (RNAi) is a gene knockdown method which exploits the natural intracellular mechanisms for transient gene expression downregulation. RNAi is induced

by siRNA in cytoplasm. There, already present enzymatic machinery is exploited to achieve highly specific and potent gene knockdown in cells. (McCaffrey *et al.*, 2002).

Process of RNAi begins with a transfection of short interfering RNA (siRNA) which is an exogenous molecule responsible for mRNA molecule specific binding. It is delivered inside a cell in a double-stranded form which is approximately 21 nucleotides long. Inside the cell, siRNA is recruited by RISC complex where one strand (passenger) leaves the complex and is degraded, while the other serves as a guiding strand. RISC, guided by the siRNA, cleaves target mRNA. Cleavage is initiated by the slicer, Ago2 protein (Meister *et al.*, 2004), which leads to mRNA degradation (fig. 5) and ultimately towards gene knock-down (Elbashir *et al.*, 2001).

Short interfering RNA (siRNA) is a promising therapeutic molecule which acts as a post-transcription gene expression regulator. For this reason, siRNA withholds strong potential in a field of cancer and genetic disorders treatment, where gene expression was altered. siRNA is a nucleic acid oligomer. It is a large molecule with negative charge because of the PO_4^{3-} backbone and therefore, requires a specific model of transport through cell membrane. Transfection reagents were developed specifically to transport RNA past cell membrane. Transfection reagents have overall positive charge which then through electrostatic interactions non-covalently bind the siRNA molecules and mask the net negative charge. Today, a vast surfeit of commercially available transfection reagents is present in every laboratory. Usually, it's either cationic polymers, such as polyethylene imine (PEI, JetPEI®) or cationic lipid carriers (Lipofectamine®). Although, it is fair to state that several PEI derived reagents already exhibit lowered toxic effects, polymer and lipid transfection reagents are still cytotoxic *in vitro* and *in vivo* (Castan *et al.*, 2018; Yamano *et al.*, 2010).

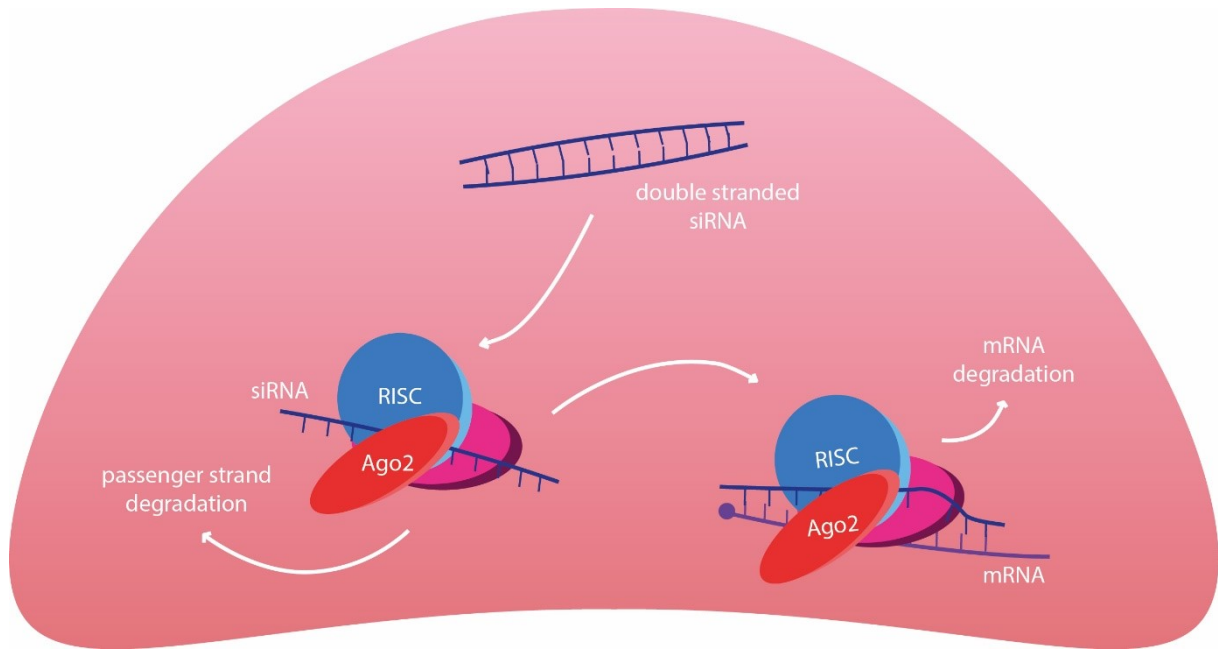


Fig. 5: RNAi process. siRNA enters the cell in a double stranded form. After introduction and binding to RISC complex, passenger strand is degraded. Remaining strand leads RISC towards targeted mRNA which is then cleaved by Ago2 nuclease (Elbashir *et al.*, 2001; Arenz and Schepers, 2003).

2. STUDY AIMS

NDs can be utilized as probes and nucleic acid carriers at the same time. They are in a focus for their potential roles in siRNA transfection and human disease treatment. The aim of this study was to bring us closer to understanding on how NDs enter cells and how NDs interact with intracellular trafficking system. To achieve this, NDs with novel surface polymers, which may interact with cell's trafficking system in a yet unknown fashion, were developed. The study divides into these main research aims:

- I. Examine the transfection efficiency of NDs complexed with siRNA and their effects on cell physiology
- II. Determine the mechanism of ND:siRNA complexes uptake
- III. Observe intracellular fate of ND:siRNA complexes

Following experiments were designed to achieve these aims:

- × Conjugation of NDs with novel polymer coating (I, II, III)
- × Gene expression silencing efficiency measurement through qPCR method (I)
- × Cytotoxicity and cell viability measurement through colorimetric assays (I)
- × Endocytosis inhibitor experiments (II)
- × Confocal microscopy observation of ND:siRNA complexes in fixed cells (II, III)

3. MATERIALS & METHODS

3.1. Materials, solutions & buffers

Unless stated otherwise, all materials were acquired from Sigma-Aldrich (now Merck) (USA).

- *Polyvinyl pyrrolidone (PVP)*
- *tetraethylorthosilicate (TEOS)*
- *3-(trimethoxysilyl)propylmethacrylate (TMSPMA)*
- *2-dimethylaminoethyl methacrylate (DMAEMA)*
- *N-(2-hydroxypropyl)methacrylamide (HPMA)* prepared according to published procedures (Rehor *et al.*, 2014)
- *Aqueous ammonia (25% w/w) (Penta Chemicals, Czech Republic)*
- *dimethylsulfoxide (DMSO)*
- *2,2'-azobis(2-methylpropionitrile) (AIBN)*
- *Lysogeny Broth (LB) medium (1 litre)*
 - × 5 g yeast extract (AppliChem, Germany)
 - × 10 g tryptone (Becton, Dickinson and Co., France)
 - × 10 g NaCl (Penta Chemicals, Czech Republic)equilibrated to pH 7.4 and autoclaved
- *Super Optimal Broth (SOB) medium (0.5 litre)*
 - × 10 g tryptone
 - × 2.5 g yeast extract
 - × 0.25 g NaCl
 - × 2.5 ml KCl [0.5M]equilibrated to pH 7, autoclaved, supplemented with 20ml of glucose [1M]
- *Phosphate Buffer Saline (PBS)*
 - × Disodium phosphate (Na_2HPO_4), [10mM], (Lachema, Czech Republic)
 - × Monopotassium phosphate (KH_2PO_4), [1.8mM], (Spolana, Czech Republic)
 - × Potassium chloride (KCl), [2.7mM] (Lachema, Czech Republic)
 - × Sodium chloride (NaCl), [137mM] (Penta Chemicals, Czech Republic)

filtered and equilibrated to pH 7.4

- *PBS for cell culture*
- *Trypsin for cell culture (GE Healthcare Life Sciences, USA)*
- *Dulbecco Modified Eagle Medium (DMEM) for cell culture with GlutaMAX, pyruvate, phenol red and D-glucose (Gibco, USA)*
 - 10% fetal bovine serum (FBS), (Gibco, USA) and 1% penicillin/streptomycin (Biowest, USA) added
- *Dulbecco Modified Eagle Medium (DMEM) for cell culture with D-glucose (Gibco, USA)*
 - 10% fetal bovine serum (FBS), (Gibco, USA), glutamine [2mM], (PAA Laboratories, Austria) and 1% penicillin/streptomycin, (Biowest, USA) added
- *TAE electrophoresis buffer*
 - × Acetic acid [20mM], (Penta, Czech Republic)
 - × Tris pH 8.0
 - × Ethylenediaminetetraacetic acid (EDTA)
- *Hank's Buffered Salt Solution (HBSS)*
 - × NaCl [137mM]
 - × KCl [5mM]
 - × Na₂HPO₄ [1.1mM]
 - × KH₂PO₄ [0.4mM]
 - × Glucose [5.5mM]
 - × Sodium bicarbonate (NaHCO₃), [4mM], (Lachema, Czech Republic)autoclaved
- *Microtubule Stabilizing Buffer (MSB)*
 - × 2-(*N*-morpholino)ethanesulfonic acid (MES), [20 mM]
 - × 2 mM ethylene glycol tetraacetic acid (EGTA), [2 mM], (Fluka, Germany)

- × Magnesium chloride (MgCl₂), [2 mM]
- × 4% (w/v) polyethylene glycol 6000 (PEG)
- *X-treme Gene HP transfection reagent (Roche, Germany)*
- *Lipofectamine® RNAiMAX Reagent (Invitrogen, USA)*
- *RNeasy Mini Kit (Qiagen, Netherlands)*
- *SuperScript III™ Reverse Transcriptase (ThermoFisher Scientific, USA)*
- *5x HOT FIREPol® EvaGreen® qPCR Supermix (Solis BioDyne, Estonia)*
- *Cell Proliferation Reagent WST-1 (Roche, Germany)*
- *Cytotoxicity Detection Kit^{PLUS} (LDH) (Roche, Germany)*
- *Filipin*
- *Dynasore*
- *Triton X-100*
- *Bovine Serum Albumin (Roth, Germany)*
- *Mowiol*
- *DAPI*
- *Vectashield® Antifade Mounting Medium (Vector Laboratories, USA)*
- *Qubit® microRNA Reagent (Invitrogen, USA)*
- *Qubit® microRNA Buffer (Invitrogen, USA)*
- *Alexa 594 conjugated Transferrin (Life Technologies, USA)*

PRIMER NAME	SEQUENCE	AMPLICON
GAPDH forward	accacagtccatgccatcact	100
GAPDH reverse	gtccaccaccctgttgctgta	
β-actin forward	gccctgaggcactcttcca	450
β-actin reverse	cggatgtccacgtcacacttc	

Table 1: List of primers for qPCR reactions

SPECIFICITY	TYPE	SPECIES	COMPANY	CAT. NO.	DILUTION
EEA1	prim. monoclonal	rabbit	Cell Signalling	#3288	1:500
LAMP1	prim. monoclonal	rabbit	Cell Signalling	#9019	1:500
Caveolin-1	prim. polyclonal	rabbit	BD Biosciences	#610059	1:500
Anti-rabbit/A488	sec. monoclonal	donkey	Jackson Immunores./Spinchem	#A11001	1:500

Table 2: List of antibodies for fluorescent microscopy experiments

OLIGO NAME	SEQUENCE	CAT. NO.
hGAPDH sense	GGUCAUCCAUGACAACUUU(dT)(dT)	8024362959-000020
hGAPDH antisense	AAAGUUGUCAUGGAUGACC(dT)(dT)	8024362959-000030
hNT sense	UAAGGCUAUGAAGAGAUAC(dT)(dT)	8024362959-000050
β -actin antisense	GUAUCUCUUCAUAGCCUUA(dT)(dT)	8024362959-000060

Table 3: List of siRNAs. Purchased from ThermoFisher Scientific, USA. hGAPDH and non-targeting (NT) were purchased both with and without blue Atto425 tag.

3.2. Methods

3.2.1. Surface silication

In order to create ND colloidal suspension, ND powder (48 mg) dissolved in 24 ml of H₂O was sonicated on a sonication tip for 60 mins (amplitude 40%, timer 30 min, 1 s on, 1 s off) and filtrated through 0.45 µm glass microfiber filter (GMF) to prepare ND colloidal suspension. Polyvinylpyrrolidin (PVP, 10 kDa, 136 mg,) was dissolved in H₂O and sonicated for 10 min in a sonication bath. PVP suspension and ND suspension were mixed together and stirred for 24 h.

Mixture was centrifuged (40 kG, 1 h). Supernatant was removed and the pellets were re-dispersed by sonication and subsequently centrifuged again (30 kG, 30 min). Pellets were re-dispersed in ethanol (30 ml, spectroscopic quality) in round bottom flask. 225 µl of tetraethylorthosilicate (TEOS) and 75 µl 3-(trimethoxysilyl)propylmethacrylate were added into the mixture and shortly sonicated in a sonication bath (~30 s). Finally, concentrated ammonia (NH₃) solution was added. The complete mixture was intensively stirred for 14 h (Rehor *et al.*, 2014).

Afterwards, the mixture was centrifuged again. Each centrifugation was done in two steps. Firstly, at 15 kG, 15 min. Supernatant was removed and centrifuged as well (20 kG, 20 min). Pellets were re-dissolved and mixed together. This step was repeated 3 times. Then, the sample was washed 3 times with methanol (HPLC quality, 20 min, 20 kG + 20 min, 40 kG) and stored in a freezer (-20 °C).

3.2.2. Surface polymerization

N-(2-hydroxypropyl)methacrylamide (HPMA) was firstly purified through re-crystallization. To achieve re-crystallization, HPMA was dissolved in acetone. Solvent was evaporated at 70°C and replaced with hexane. Homogenous mixture was re-crystallized in a freezer (-20 °C) overnight. HPMA crystals were dried on a rotary evaporator. Alternatively, AIBN was purified by re-crystallization from ethanol.

Mixture of HPMA (164 mg), 2,2'-azobis(2-methylpropionitrile) (AIBN, 188 mg) and 2-dimethylaminoethyl methacrylate (DMAEMA, 492 mg) were dissolved in 1 875 µl of DMSO. Methacrylate-terminated NDs (30 mg) were transferred into 188 µl of DMSO using rotary evaporator. Finally, NDs were added to the mixture. The reaction proceeded for 3

days under Ar atmosphere at 55 °C. Afterwards, NDs were centrifuged (21 kG, 30 min) and washed with methanol 3 times (20 kG, 20 min + supernatant 20 kG + 40 min).

The same washing process was used to change ND solvent (D₂O for NMR, H₂O for most applications) (Rehor *et al.*, 2014).

3.2.3. Gravimetry

To-be-used Eppendorf tubes were weighed before approximately 1.5 – 2 mg of NDs in H₂O was added. Then, the ND solution was dried by Speedvac Vacuum Concentrator (ThermoFisher Scientific, USA). The tubes were weighed again, and the concentration of NDs in H₂O was determined from the weight difference.

3.2.4. ND:siRNA complex preparation

To find the most stable and effective siRNA:ND weight ratio between siRNA and NDs, siRNA [100mM] was first diluted in deionized and distilled water (ddH₂O). The volume of H₂O equaled the volume of ND solution which was added to the mixture in the next step. Then, the Eppendorf tube with diluted siRNA was submerged in sonication bath. While moving the tube over a cavitation hotspot, ND solution (4.14 mg/ml) was slowly pipetted into the siRNA Eppendorf tube. Sample was kept submerged and sonicated for one minute. e. g. 0.506 µl siRNA was diluted in 4.28 µl of H₂O. During sonication 4.28 µl of ND solution was added.

3.2.5. Particle diameter determination and ζ-potential

Stability assessment based on Dynamic Light Scattering (DLS) was conducted with a Zetasizer Nano ZS system (Malvern Instruments) as well as the measurement of ζ-potential.

In order to assess the colloidal stability and the state of aggregation, ND:siRNA complexes were tested in H₂O, PBS, DMEM with and without serum, and RPMI with or without supplement at an ambient temperature (25°C) and physiological temperature (37 °C). ND concentration was 0.3 µg/µl.

3.2.6. Free siRNA determination after ND:siRNA complexation

Complexes of siRNA were prepared by aforementioned procedure in weight ratio 25:1 (ND:siRNA) in water. 1.28 μl of siRNA was diluted with 10.58 μl of H_2O . Diluted siRNA was mixed with 10.58 μl of NDs. Colloidal complex was centrifuged (40 min, 30 kG) and 10 μl of supernatant was aspirated. During centrifugation, working concentration Qubit solution was prepared in RNase-free environment. 2 μl of stock Qubit® microRNA reagent (200 \times) was diluted in 398 μl of Qubit® microRNA buffer. 10 μl of supernatant was mixed with 190 μl of diluted Qubit® reagent. After 2 min incubation at room temperature, concentration of free siRNA was measured on Qubit® 2.0 Fluorometer (Invitrogen, USA).

3.2.7. Human cell line culture

Experiments were conducted on U-2 OS (ATCC HTB-96, osteosarcoma) cell lines. Cell lines were routinely cultivated at 37 °C in 5% CO_2 atmosphere in 25 cm^2 culture flasks, 60 mm, and 100 mm petri dishes (TPP, Switzerland). Cells were grown in full DMEM culture medium with antibiotics and supplemented with 10% serum. To prevent cells reaching fully confluent state, cells were periodically passaged.

During cell passaging, medium was aspirated, cells were washed gently with PBS (cell culturing purity), incubated with trypsin. When suspended, fresh DMEM was added and cells were centrifuged (120 G, 25 °C, 4 min). 1/8 of the original cell amount was resuspended and transferred to a flask or a dish.

3.2.8. qPCR experiments

Cells were seeded on 12-well plates. When confluency of ~70% was achieved, cells were treated with combinations or standalone aliquotes of ND, RNAiMAX, and siRNA accordingly to fig. 6. ND:siRNA complexes were prepared in consensus with chapter 3.2.1.4.

Both Atto425-tagged hGAPDH and hNT siRNA were diluted and complexed as follows. 0.5 μ l of 100 μ M siRNA was mixed with 4.28 μ l of ddH₂O. Then in sonication bath, 4.28 μ l NDs (4.14 mg/ml) was slowly added to the mixture. Correspondingly with the Invitrogen manual, 3 μ l of RNAiMAX was diluted in 30 μ l of serum-free DMEM. 0.5 μ l of siRNA [100 μ M] was added to another Eppendorf tube with 30 μ l of serum-free DMEM. Both tubes were mixed and incubated for 5-10 minutes. ND and RNAiMAX mixtures were diluted with DMEM to final volume of 500 μ l ($c_{ND} = 35.4 \mu\text{g/ml}$, $c_{siRNA} = 100 \text{ nM}$) and finally transferred to the according wells. 4.28 μ l of ND and 3 μ l of RNAiMAX were transferred to the according wells, too (fig. 6).

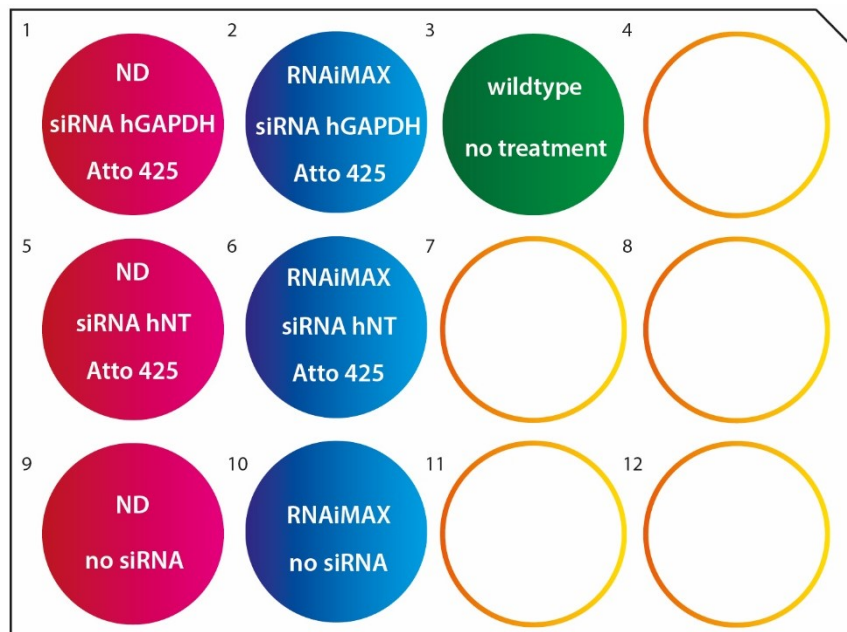


Figure 6: 12-well plate layout for transfection efficiency assessment.

After 36 hours, cells were harvested with trypsin and washed in PBS. From this point forward, samples in Eppendorf tubes were kept on ice. Total RNA was extracted using RNeasy Mini Kit. Total RNA concentration was established with NanoDrop ND-1000 Spectrophotometer (ThermoFisher Scientific, USA). Subsequently, ~500 ng of total RNA was transcribed to cDNA with SuperScript III™ according to the manufacturer's manual. cDNA was diluted 60 \times . For qPCR reaction (15 μ l per well) 5x HOT FIREPol® EvaGreen®

qPCR Supermix was used. Furthermore, GAPDH and β -actin primers and H₂O were added (see fig. 7). Experiments were conducted in repeated three times in technical triplicates. Reactions were executed in iQ5 Multicolor RT PCR Detection System (Biorad, USA). Expression levels of each sample was related and normalized to housekeeping gene β -actin. Relative mRNA quantitative levels were calculated by $\Delta\Delta C_t$ method (Livak and Schmittgen, 2001).

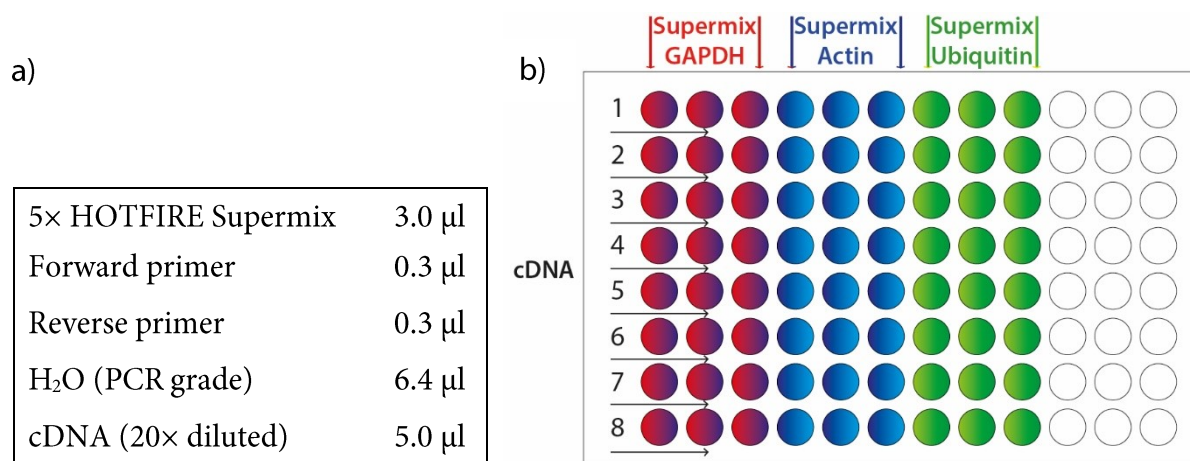


Figure 7: qPCR a) table on single well reagents (. b) Distribution of cDNA (1-8 rows) and triplicates of Supermix with primers (columns) in 96-well plate. Glycereraldehyde 3-phosphate dehydrogenase (GAPDH), Beta-actin (Actin) Ubiquitin-B (Ubiquitin)

3.2.9. Cytotoxicity and proliferation assays

Cytotoxicity and viability tests are important steps in determination of biocompatibility of any NP, including NDs. To measure cytotoxicity, LDH kit was used according to the manufacturer's protocol. LDH kit measures enzymatic activity of lactate dehydrogenase (LDH), which escapes to culture medium when cells' membranes are damaged. Wells in 96-well plates were seeded with 10 000 cells in DMEM (100 μ l). Cells were counted with Countess II Automated Cell Counter (ThermoFisher Scientific, USA). After 12 h, cells were treated with ND:siRNA and RNAiMAX:siRNA (see tab. 4 for information about concentration) complexes in 59 μ l of DMEM. Two wells were filled only with DMEM for blank measurements. After 36 h (37 °C, 5% CO₂), negative controls were treated with 4% (v/v) Triton X-100 for 10 min. Afterwards, supernatants from all wells were aspirated and transferred to new 96-well plate and diluted to final volume of 100 μ l per well. 100 μ l of LDH mix, LDH catalyst (2.17 μ l) + LDH dye (97.83 μ l) was added and

incubated (15 min, 37 °C, 5% CO₂). Then, in order to terminate the reaction, stop buffer (50 µl) was added (Shah *et al.*, 2017). Measured data was automatically

subtracted from blank wells. All experiments were conducted on U2OS cells at least 3× in triplicates.

Cell viability assays are used to quantify the adverse effect of NDs on physiology of the cell by testing mitochondrial enzymes within the cells. Cell viability can be changed even though cell membrane is intact. Viability was measured with WST-1 assay. WST-1 colorimetric assay measures intracellular enzymatic activity. Intact cells exhibit high enzymatic activity, damaged cells exhibit low enzymatic activity. Cells were treated equally with ND and RNAiMAX complexes. Positive controls were untreated and negative control cells were incubated with paclitaxel [40nM]. After 36 hours, WST-1 (10 µl) was added. After 45 minutes (37 °C, 5% CO₂), plates were measured with a plate reader ELx800 (emission 450 nm/ background 630 nm, Dynex, Czech Republic) (Shah *et al.*, 2017). Measured data was automatically subtracted from blank wells. All experiments were conducted on U2OS cells at least 3× in triplicates.

Sample	Carrier concentration	siRNA concentration
ND:siRNA _{standard qPCR}	50.5 µg/ml	125 nM
ND:siRNA _{4× qPCR}	202.0 µg/ml	500 nM
RNAiMAX:siRNA	8%	125 nM

Table 4: Concentration of NDs, RNAiMAX, and siRNA for cytotoxicity assays. Standard qPCR and RNAiMAX contain the same concentrations as in qPCR experiments

3.2.10. Endocytosis inhibition samples and time series samples

U-2 OS cells were grown to 60% confluency on glass cover slips in 24-well plates in DMEM (350 µl). In order to lower endocytosis rate of cells, plates were cooled down for 3 minutes. Subsequently, ND:siRNA complexes were added to corresponding wells. To keep low endocytosis rate and to promote ND:siRNA complex stability, plates were promptly returned to cool down (7 °C, 5 min). In every timepoint, corresponding cells were washed with PBS, fixed with 3% PFA in MSB and washed with PBS again.

Old medium was replaced with fresh full serum medium (350 µl). ND:siRNA_{4×qPCR} complexes were prepared (see tab. 4)

Old medium was replaced with serum-free DMEM (350 μ l) before the start of incubation with inhibitors. Fresh aliquots of Filipin [7.64mM] and Dynasore [31mM] in DMSO were prepared for each experiment. Final concentrations of inhibitors were 400 μ M and 7.64 μ M of Dynasore and Filipin, respectively. ND:siRNA_{4x} qPCR (see tab. 4) was prepared. Fluorescent transferrin A594 (TfA594) was used as positive control for Dynasore downregulated CME experiments (Macia *et al.*, 2006). Cells were incubated for 20 minutes with inhibitors (37 °C, 5% CO₂) and cooled down for 3 minutes (7 °C). Then, cargo was added to the corresponding wells while maintaining low temperature (7 °C, 5 min). The plate was put in cell incubator (37 °C, 55 min). Cells were then quickly washed with PBS and fixed in 3% paraformaldehyde (PFA) in MSB (37 °C, 15 min).

3.2.11. Immunofluorescent labelling

Cells were washed with PBS three times after fixing with PFA. Then, 0.1% Tx-100 was added to permeate cell membranes. Cover slips were washed again with PBS three times. Antibodies were diluted (see tab. 2) in 2% BSA in PBS. 20 μ l droplets which were pipetted on Parafilm M (Bemis Company, USA). Coverslips were incubated (cells facing the parafilm/droplet surface) in the droplets of primary antibodies for 1 h. Coverslips were washed with PBS three times, incubated with secondary antibodies and washed with PBS three times. To remove salts and impurities, coverslips were washed in distilled, deionized H₂O. Coverslips were then mounted in adequate droplets of Mowiol (0.1% DAPI) or in Vectashield® Antifade Mounting Medium (VS). VS does not dry, therefore nail polish was used to fix the coverslips in place.

3.2.12. Microscopy

All samples were fixed and mounted in either Mowiol with DAPI or in Vectashield. All images in this work were acquired by Zeiss LSM 880 confocal microscope (Carl Zeiss AG, Germany) with Zen Black software. 63× objective with immersion oil was used. Excitation of Atto425-modified siRNA, A488-labeled cell structures, and NDs was carried out with 405 nm, 488 nm, 561 nm lasers with corresponding filters. However, high noise was detected and in order to acquire true signal, lambda scans of single fluorophore samples were acquired. Their lambda profiles were detected and saved to database. Lambda scans were conducted on every sample.

3.2.13. Microscopy image analysis

Saved lambda profiles were then extracted from local Zen database. Linear unmixing analysis in Zen Black was then conducted in order to gain most reliable images (see supplementary fig. 1). Linear unmixing analysis determines relative contribution from fluorophores for every single pixel in the image.

Further analysis and adjustments were executed in Fiji ImageJ software. All images were acquired under the same conditions and their contrast was adjusted for the purpose of this thesis with the same script (see supplementary script 1).

In order to recognise cell edges, script using contrast either from brightfield images or fluorescence images was utilized (supplementary script 2). These cell edges defined regions of interest (ROIs). Fluorescent signal from NDs was auto-thresholded by Triangle method. Particles were then measured through Fiji plugin Analyse particle within the ROI boundaries with a size range 5-500 pixels. Output of this plugin was an area percentage of ROI which NDs occupied.

Background noise was subtracted. Then, colocalization analysis data of NDs, siRNA and endosomal structures were acquired from Fiji Coloc 2 plugin Coloc 2. Point spread function was set to 2.8. Coloc 2 calculated Pearson's Correlation Coefficient (PCC) which was selected for colocalization data interpretation.

4. RESULTS

4.1. ND surface polymerization and characterization

Surfaces of NDs were successfully modified with silica layer tetraethylorthosilicate (TEOS). Onto this layer, hydroxypropylmethacrylamide and dimethylaminoethyl methacrylate HPMA:DMAEMA (fig. 8a) in 4 different monomer weight ratios: 1:0 (= 0% DMAEMA), 3:1, 1:1, 1:3, 0:1 (= 100% DMAEMA) were grafted, respectively. In order to determine their stability, NDs' hydrodynamic diameter and ζ -potential in pH 7.4, 8, 9, and 10 were measured (figs. 8b, c.).

25% polymer ratio kept its diameter around 100 nm in all tests (fig. 8b.) and was selected for further experiments. Overall, two more batches of 25% (3 HPMA: 1 DMAEMA)

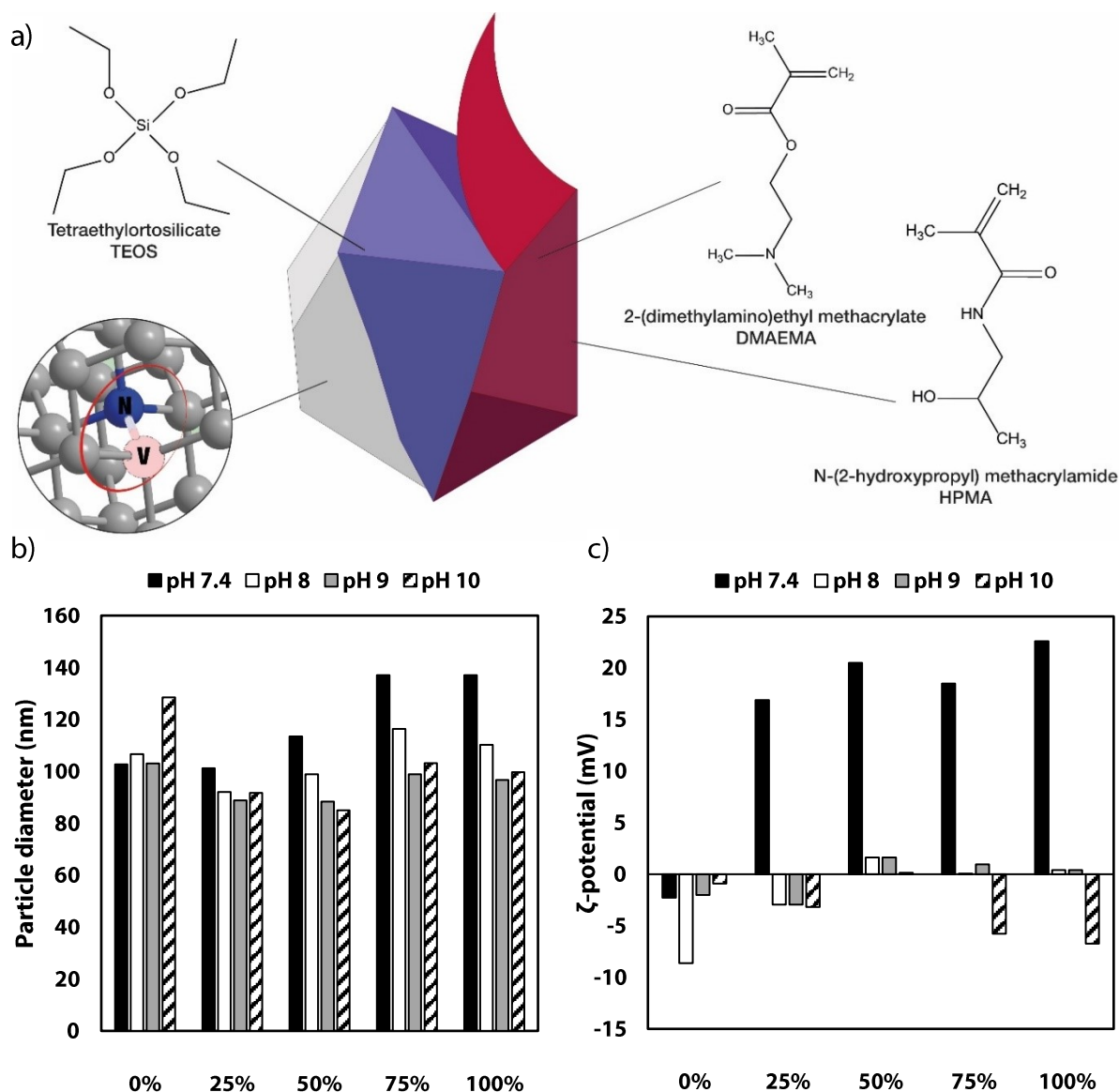


Figure 8: ND characterization. a) Model of ND with TEOS and polymers HPMA, DMAEMA and N-V center structure. Diameter (b) and surface charge (c) of NDs with 5 DMAEMA:HPMA ratios in multiple pH environment.

polymer-modified NDs were prepared for upcoming experiments. Through gravimetry, concentration of stock solution of NDs with polymers was determined to 4.14 mg/ml. Mean zeta-potential of NDs was +45.5 mV in ddH₂O.

4.2. ND:siRNA complex stability

In order to transport stable ~100nm ND:siRNA complexes (fig. 9) into cells, specific N:P weight ratio between N (ND, cationic monomer) and siRNA (P, phosphate) was established to 25:1.

ND:siRNA complexes formed stable colloids in water and in PBS. However, when introduced into culture media, complexes formed clusters overtime (fig. 10). Effect of serum was observed overtime, but no significant shift in stability was observed at first.

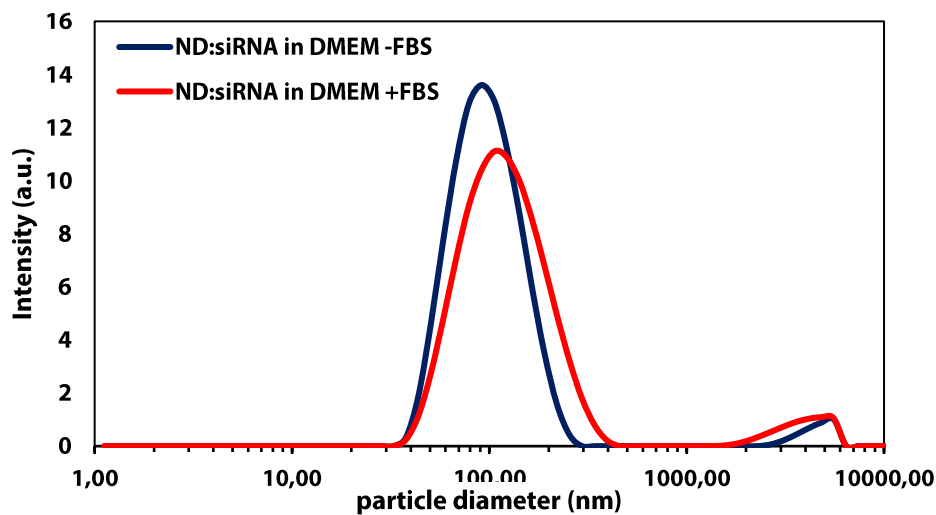


Figure 9: ZetaSizer size distribution plot. ND:siRNA complexes in both serum positive) and serum negative remained stable (100nm.)

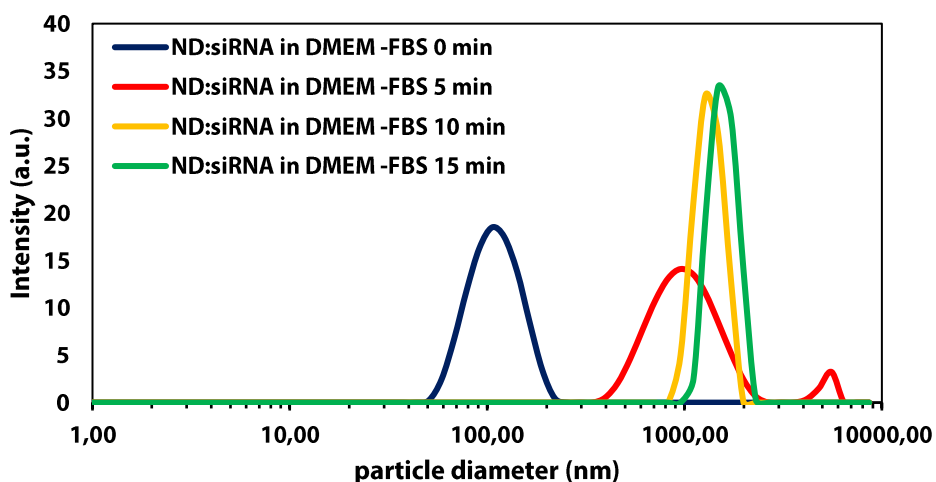


Figure 10: ZetaSizer size distribution plot of aggregates. ND:siRNA complexes begin to cluster when in medium without serum. Overtime, clusters grow.

However, when temperature was raised, suddenly, complexes clustered up and precipitated. This was not observed in medium with 10% serum (fig. 11a). Although when microscopy images were acquired, small fraction of complexes still formed clusters (fig. 11b). Overtime these clusters disappeared from the measured area because they likely sedimented and stable colloid complexes were observed again (~80–150 nm.)

Determination of the unbound fraction of siRNA to ND was assessed with fluorometer Qubit 2.0 (Thermofisher Scientific, USA). Fraction of free (unbound) siRNA was as small as 0.4%.

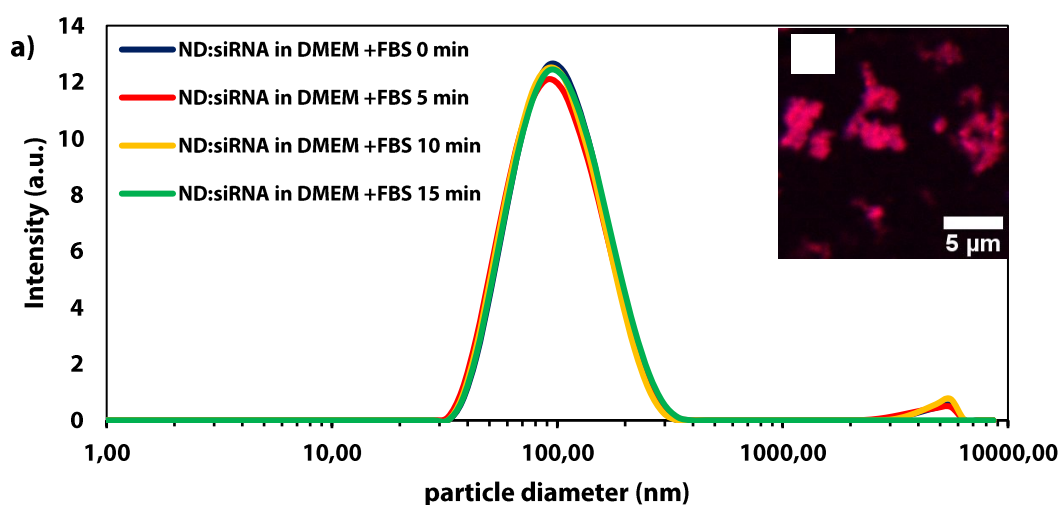


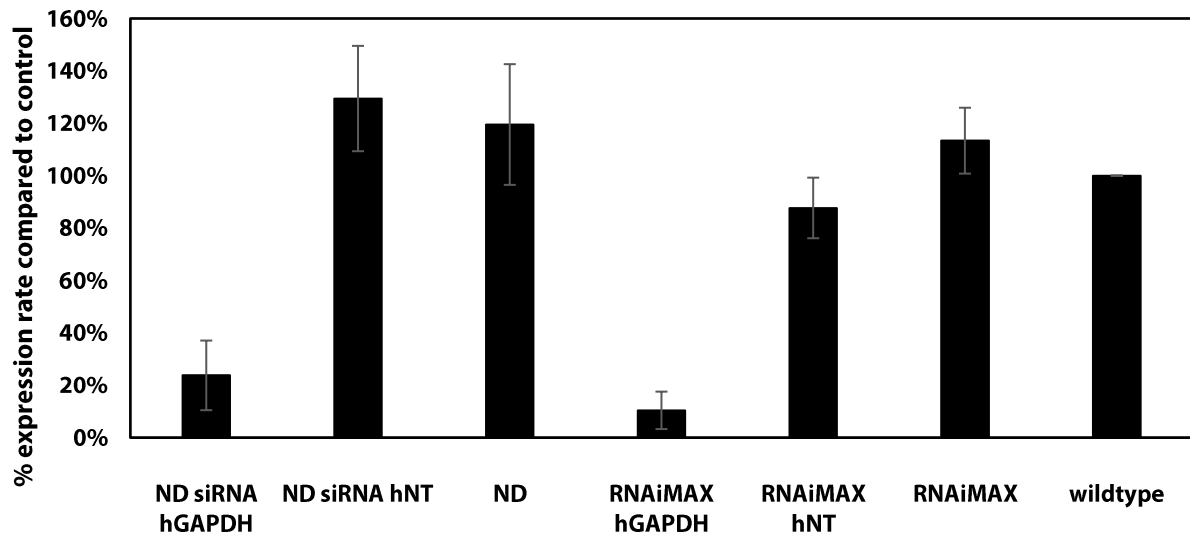
Figure 11 Serum stability of NDs. a) ND:siRNA complexes remain stable when in medium with serum at 37 °C. Overtime, no clusters grow. b) However a fraction of ND:siRNA complexes (overlap of red and blue) creates cluster and sediments.

4.3. Quantitative PCR

In order to determine the efficiency of NDs in delivering siRNA into cells, where siRNA should dissociate and bind RISC and finally induce knockdown RNAi, qPCR method was selected. The housekeeping gene GAPDH was targeted by siRNA. siRNA was covalently modified with Atto425, a blue fluorescent label. This modification allowed us to examine siRNA dissociation from NDs during confocal microscopy imaging. Atto425-modified GAPDH siRNA and Atto425-modified control (non-targeting) siRNA were used in order to minimize as many potential discrepancies as possible between all experiments. All data was related to housekeeping genes β -actin of non-treated wild type cells. The siRNA molecules were delivered in the same concentration either by Lipofectamine® RNAiMAX or by NDs for comparison.

NDs exhibited significant transfection efficiency. siRNA delivered by NDs exhibited 76% gene knockdown in U-2 OS cells. RNAiMAX:siRNA complexes-treated cells exhibited 90% gene knockdown, as expected from a commercial transfection kit. To determine carrier effects on gene expression, ND and RNAiMAX alone or with complexed non-targeting siRNA were measured as well and showed no decrease in GAPDH gene

a)



b)

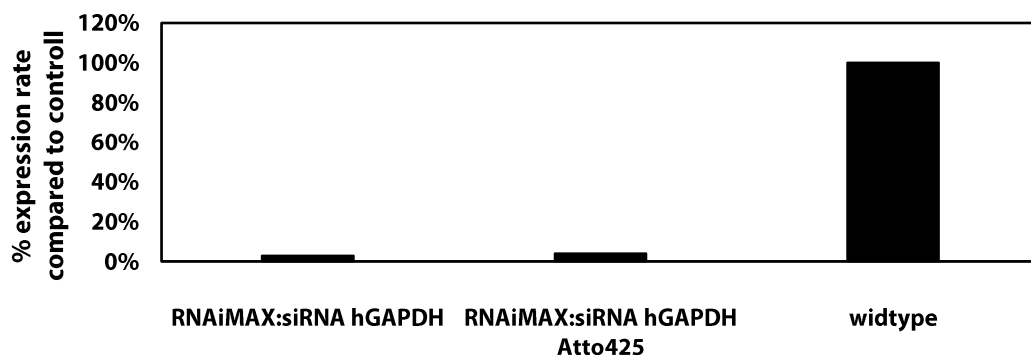


Figure 12: qPCR assays of gene expression knockdowns. a) In U-2 OS cells, NDs with GAPDH targeting siRNA exhibited 76% transfection efficiency. RNAiMAX (iMAX) mediated transfection achieved 90% decrease in GAPDH expression rate. Carriers alone or complexed with non-targeting (NT) siRNA mediated no gene knockdown in cells. b) Difference in **RNAi potential** between Atto425 tagged (blue) siRNA and siRNA without this tag measurement shows no significant difference.

expression in cells (fig. 12a). In order to test if siRNA induced gene knockdown properly, GAPDH targeting, tagged and non-tagged siRNAs were compared with RNAiMAX. No significant differences were measured (fig 12b.)

4.4. Cytotoxicity

Introduction of transfection agents may cause negative effects on cell physiology. Furthermore, gene expression alteration may be caused by transfection agent-mediated damage.

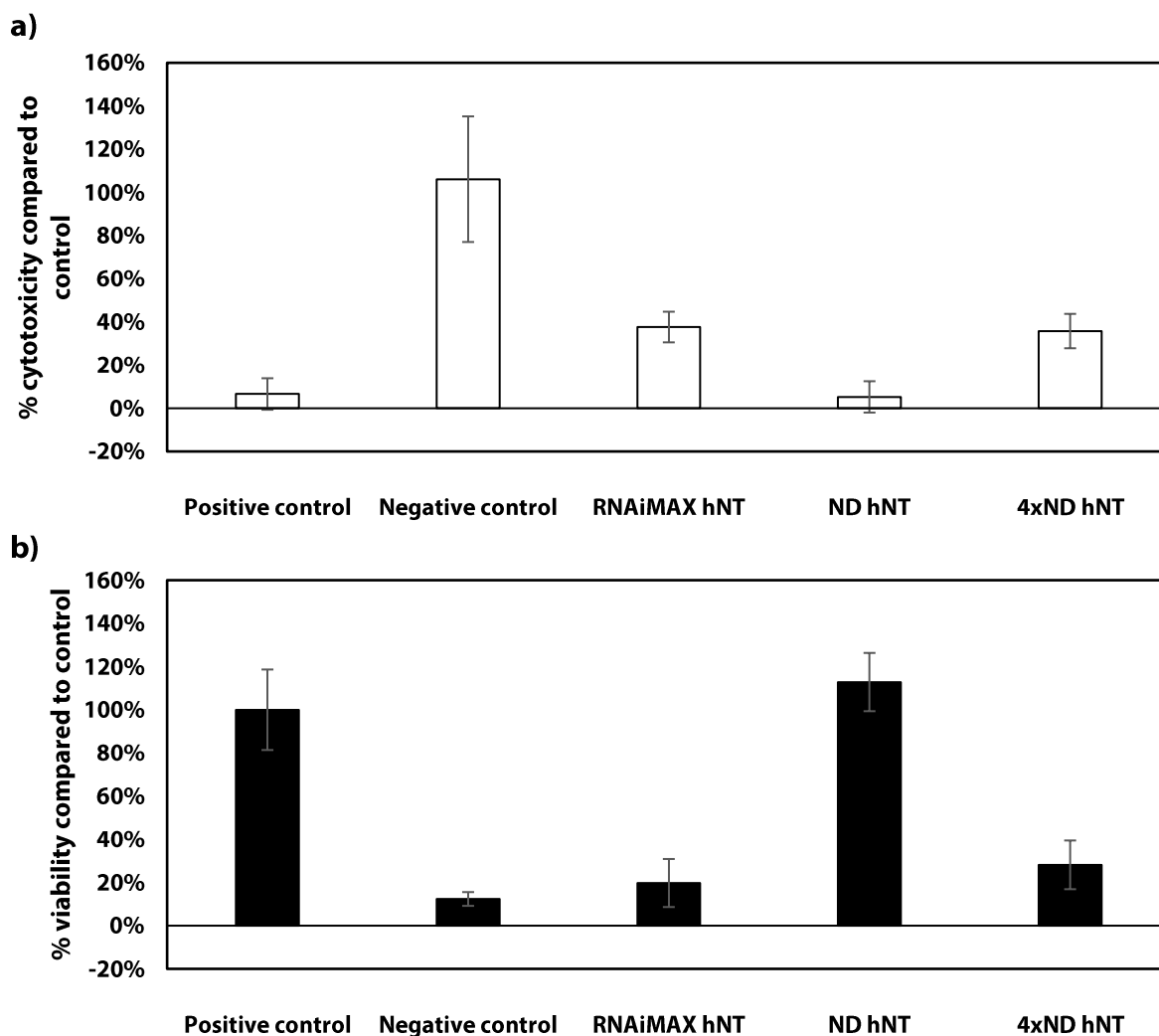


Figure 13: Cytotoxicity and proliferation assays. a) High LDH results indicate perturbations and cell death as lactate dehydrogenase exit cell and cleave tetrazolium salts into dyes. b) High WST-1 results indicate high cell viability, because enzymes effectively cleave tetrazolium salts to visible dyes. Positive controls are untreated cells. Negative controls are treated with paclitaxel (WST-1) or by triton-100 (LDH). Herein, NDs cause no adverse effect on cell fitness when administered in qPCR-like concentration, unlike RNAiMAX. Equally, 4× higher qPCR-like ND concentration results in adverse effect on an overall cell fitness.

In order to determine the cytotoxic effects, LDH cytotoxicity assay was used. LDH colorimetric assay measures enzymatic activity of typically intracellular lactate dehydrogenase (LDH). However, in cells with damaged cell membrane, these enzymes escape. Triton-treated negative control resulted in cell membrane damage and cell death. Large portion of LDH then is located in the medium, therefore, colorimetric scan resulted

in high signal. Medium activity from positive control cells (full serum medium treated only) was minimal. NDs-treated cells exhibited low extracellular activity. However, 4× higher concentration than standard qPCR concentration results in an increase in medium activity, indicating cell membranes damage. Similarly, RNAiMAX induced membrane damage as well (fig. 13a).

Although it was discovered that NDs do not inherently cause cytotoxicity through LDH assay, the results did not indicate if the intracellular processes were intact, too. In order to examine viability of cells on intracellular level, WST-1 assay was used. This method exploits mitochondrial enzymes which in viable cells cleave WST-1 salts to formazan dyes, which were measured on plate reader ELx800. Data show in consensus with LDH assay that NDs at qPCR concentration level cause no adverse effects on cell viability. RNAiMAX and high ND concentration resulted in low intracellular enzymatic activity and indicated adverse effects on cell viability (fig. 13b).

4.4.1. Nanodiamond endocytosis mechanism determination

Understanding cell entry mechanism of NDs is required in order to achieve maximum specificity and effectivity of NDs cell uptake. Herein, we used specific pathway inhibitors – Dynasore to inhibit CME and Filipin to inhibit CavME. Since both inhibitors were diluted in DMSO, additionally to cells treated only with medium, DMSO controls were examined as well. Data was acquired through confocal microscopy.

Experiments were divided into two groups. Positive control cells (fig. 14a) and DMSO (fig. 15a) treated cells in Dynasore group exhibited strong uptake of fluorescently labelled transferrin. When treated with Dynasore, uptake of transferrin was significantly hindered (fig. 16a). Correspondingly, ND uptake was similar in DMSO treated (fig. 15b) and control cells (fig. 14b). When Dynasore was present, the uptake of NDs was hindered as well (fig. 16b). To quantify, total area of NDs inside the cells was measured with ImageJ Fiji's Analyze Particle plugin. Analysis shows that uptake of NDs in Dynasore lowered by >30% (fig. 17). Second group was inhibited with Filipin and exhibited the same reduction in total intracellular area fluorescence signal (figs. 17-18).

Albumin with fluorescent tag (Chatterjee *et al.*, 2017) and fluorescently labelled Cholera Toxin subunit (Orlandi and Fishman, 1998) were expected to enter the cell

through CavME and were intended as controls. However, albumin did not enter the cell and Cholera toxin was observed only on cell membrane.

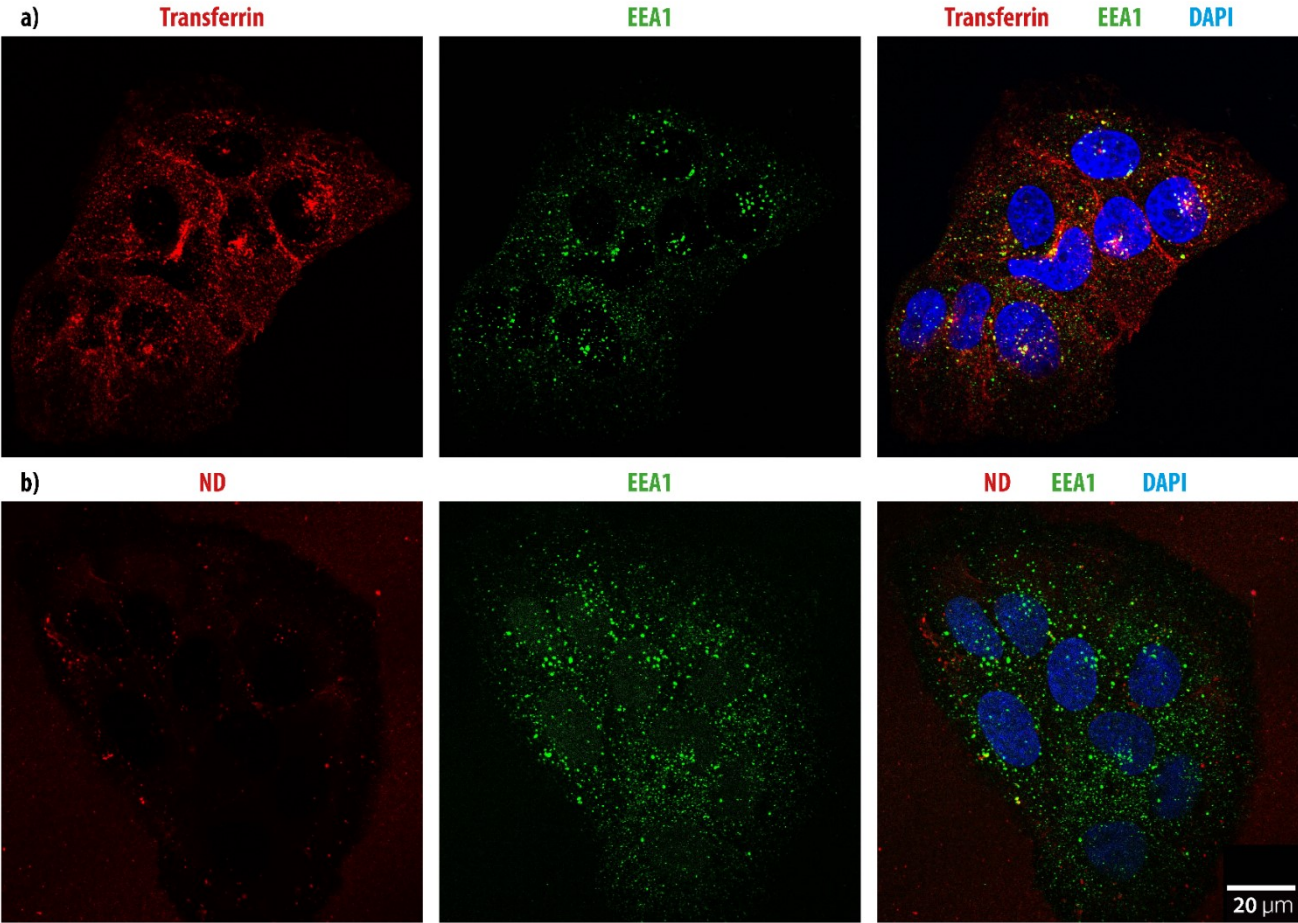


Figure 14: Positive control cells in Dynasore group: a) Cells exhibit strong internal signal of transferrin (red) after 60 minutes of incubation time. b) NDs (red) are present in the intracellular space.

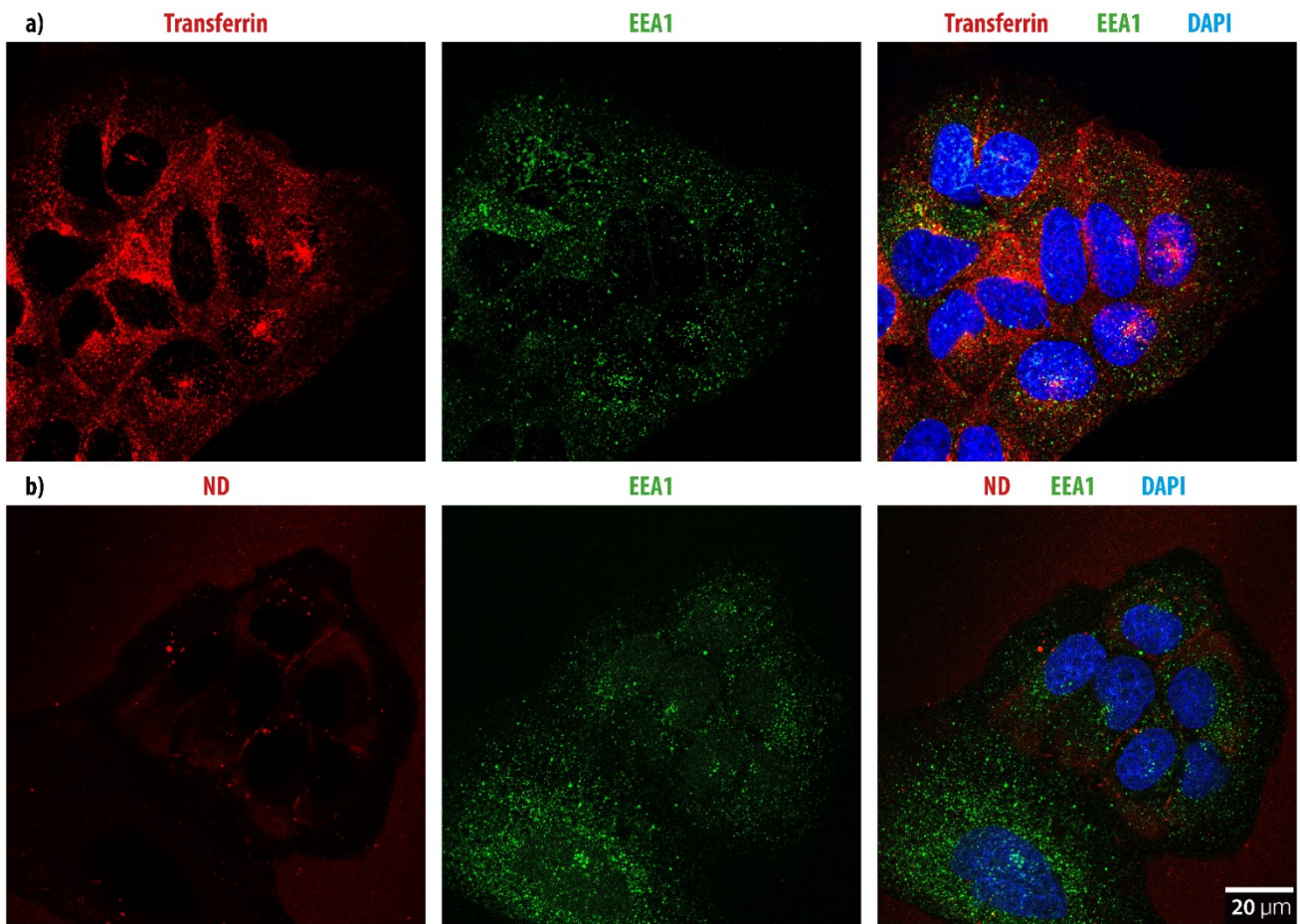


Figure 15: DMSO control in Dynasore group. a) Strong transferrin signal (red) is present inside the cells. b) ND (red) signal is well observable inside of the cells as well, suggesting equal particle uptake in comparison with control cells.

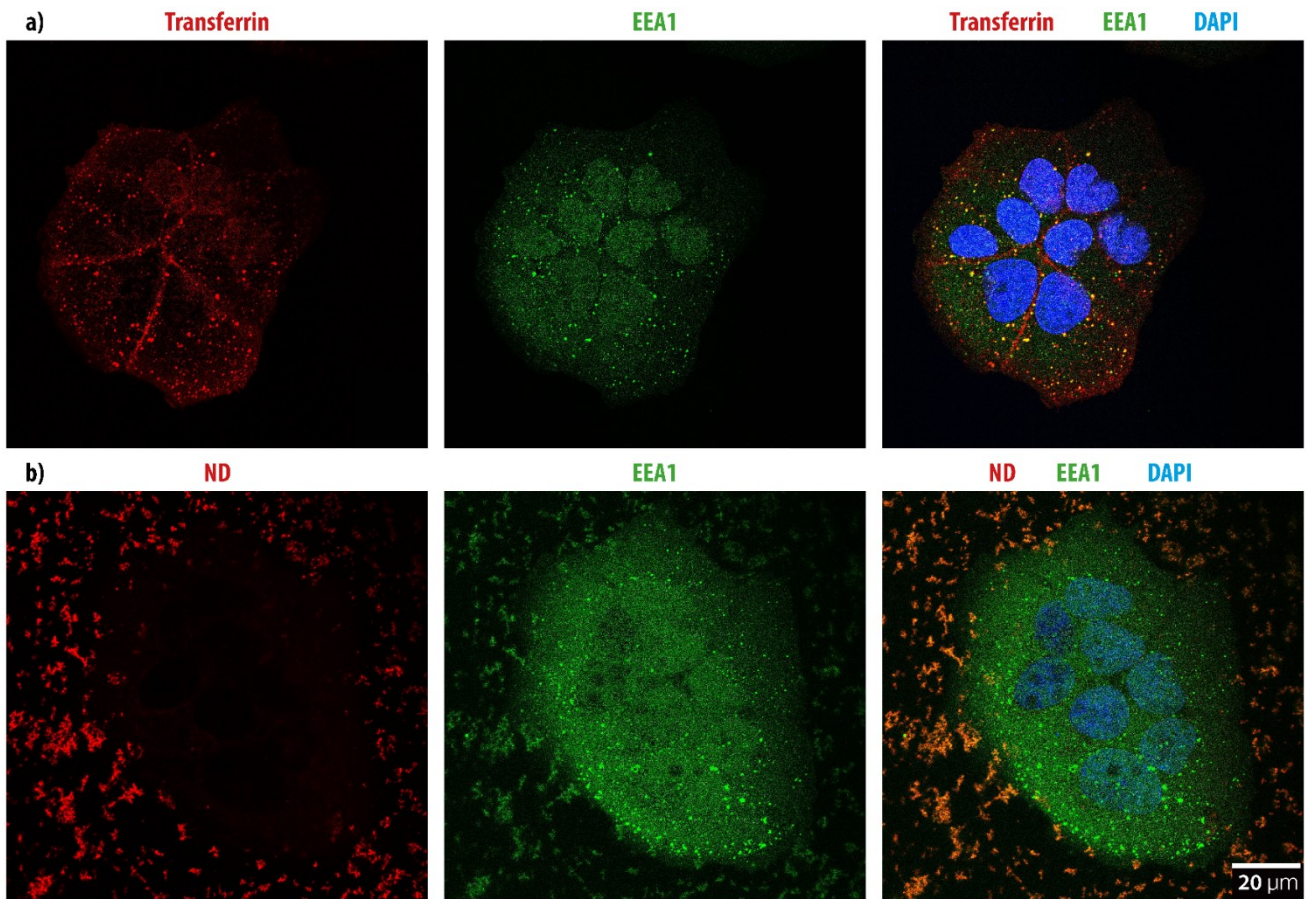


Figure 16: Dynasore treated cells in Dynasore group. a) Presence of transferrin (red) inside of the cells is distinctly reduced. b) ND signal within the cell is correspondingly lowered. In both (a, b) situations a significant green fluorescence noise is detected.

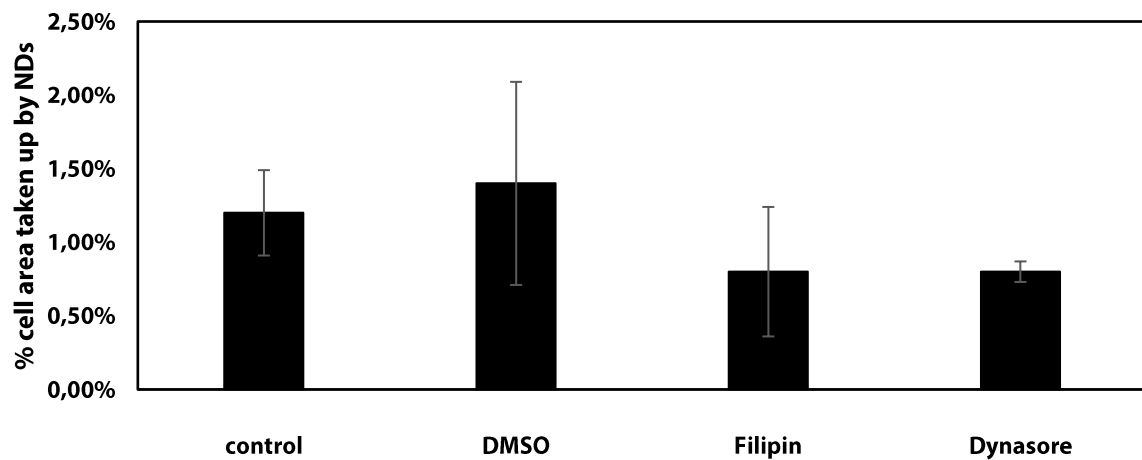


Figure 17: Inhibitor effect on ND uptake. Through confocal microscopy, ND signal was detected in 1.2% and 1.4% of a total cell area in untreated control cells and DMSO treated cells, respectively. 0.8% signal was detected in both Filipin and Dynasore treated cells.

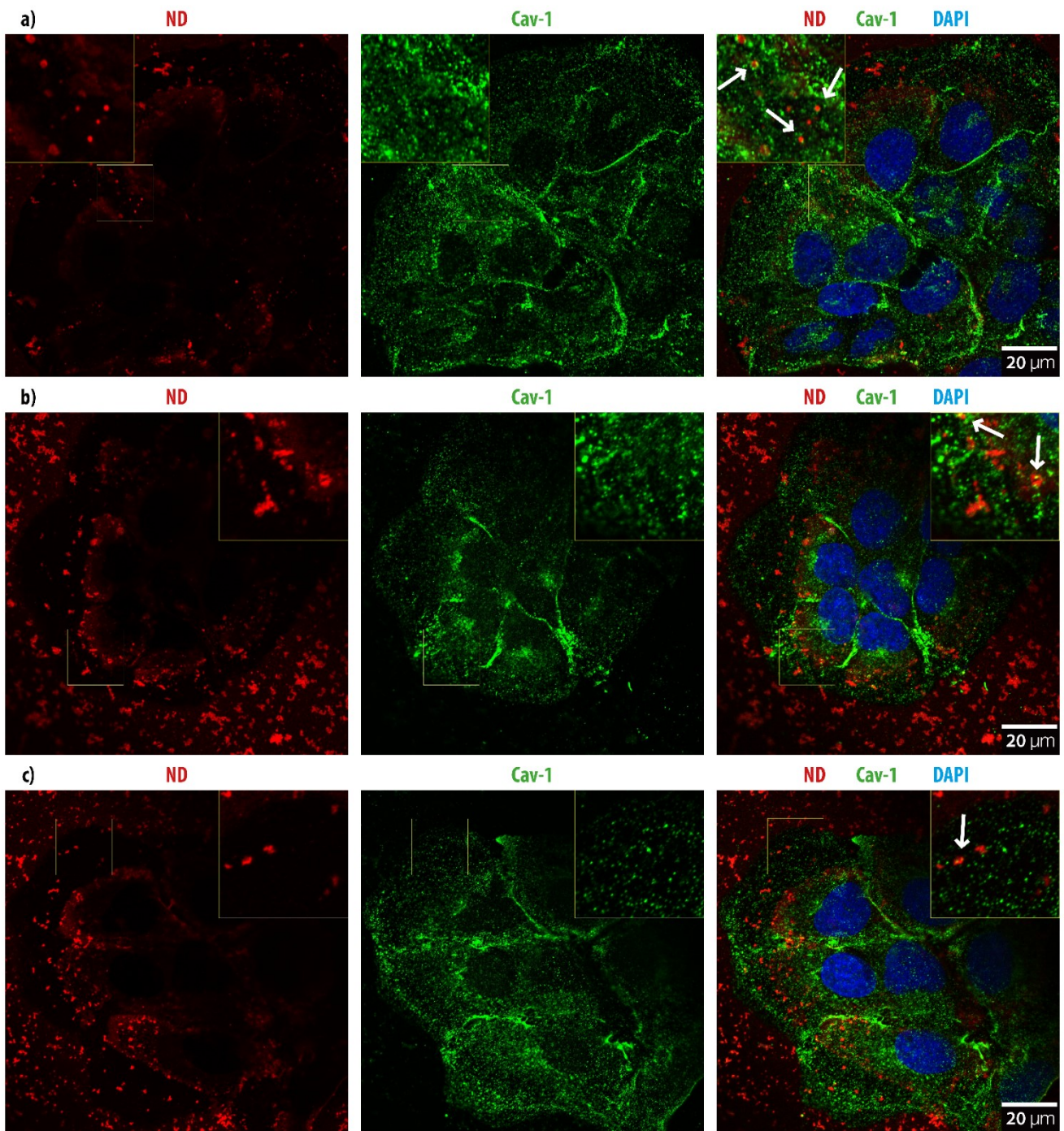


Figure 18: Filipin group cells. NDs (red) are visible inside positive control cells (a) and colocalize with markers Cav-1 (green). Colocalization (arrows) between green and red channel is observed in DMSO (b) and filipin (c) treated cells. Moreover, uptake is detected in all cell samples in filipin group.

4.4.2. Uptake and intracellular localization of ND:siRNA complexes

In order to observe advance of NDs through cell's endocytic pathways, time points 15, 45, 90 and 120 minutes were set. At 0 minutes, ND:siRNA complexes were introduced to cells under low temperature. After 5 minutes, samples were moved into an incubator (37 °C, 5% CO₂). Complexes of NDs (red signal) and siRNA (blue signal) were observed in cells stained with either LAMP1 or EEA1. In 15 minutes, NDs sedimented on the glass surface and where present on the cells' peripheries, albeit not likely entering the cells, since observed NDs were often too large for endocytosis. After 45 minutes, amount of NDs residing within the cell (measured in percentage of total cell area) raised slightly from approximately 0.6 to 0.9%. In peripheries, NDs inside cells were observed. Then, amount of NDs significantly raised to 2.04% of cells inner area in 90 minutes. Herein, NDs were further observable inside the cells. Finally, in 120 minutes the amount of NDs raised no more and remained at 1.66% (fig. 19).

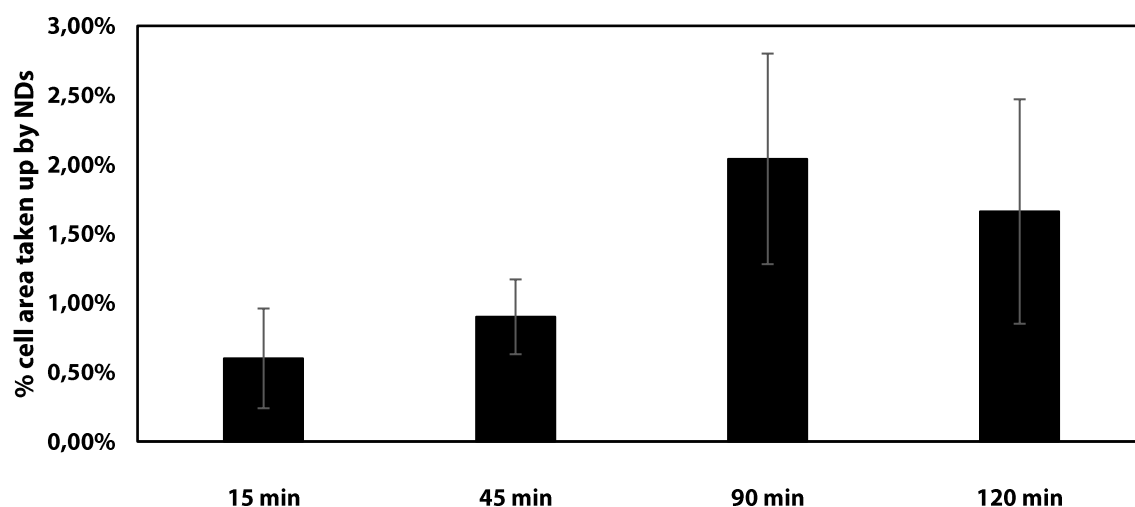


Figure 19: Intracellular area ND distribution. At 15 minutes, total surface of NDs in a confocal plane equals 0.6% of total cell confocal plane area. With time, this percentage rises to 0.9% at 45 minutes, 2% at 90 minutes and does not rise further in 120 minutes.

7% colocalization of NDs with A488 secondary antibody labelled EEA1 was detected already 15 minutes after ND:siRNA complexes introduction to cells' medium. 45 minutes into incubation, the colocalization raised to 9%. 90 and 120 minutes after the beginning of incubation, increase of colocalization began to presumably reach a 15% plateau (fig. 27a), however data from further time points are necessary. Though, no overlap or proximity between green and red channel was observed in 15 minutes into incubation (fig. 20). After 45 minutes of incubation and further, however, these signals

exhibited some degree of overlap, but predominantly, these signals were observed in close proximity (figs. 21-23).

Colocalization with lysosomal structures (LAMP1) was measured 45, 90 and 120 minutes after the start of the incubation with ND complexes. Herein, 7%, 12% and 14% colocalization was measured and described with PCC, respectively (fig. 27b). However, on acquired images (figs. 24-26), there was no overlap between red channel (NDs) and green channel (LAMP1). However, NDs often resided in close proximity with LAMP1-labeled lysosomes.

Results of inhibitor experiments, where ND signal visibly overlapped with green Cav-1 signal (fig. 18) were followed up. Quantification of colocalization resulted in 23% PCC value.

Finally, colocalization was calculated also between red channel of NDs and blue channel of siRNA molecules in extracellular and intracellular environment. Intracellular PCC values were then subtracted from extracellular values to observe difference in colocalization. Already after 15 minutes of incubation, colocalization difference reached 8%. Both extra- and intracellular PCC values reached 62% and 32%, respectively after 45 minutes ($\Delta 30\%$). Afterwards, both extra- and intracellular colocalization levels reached equality and decreased in 90 and 120 minutes (fig. 28).

ND EEA1 siRNA

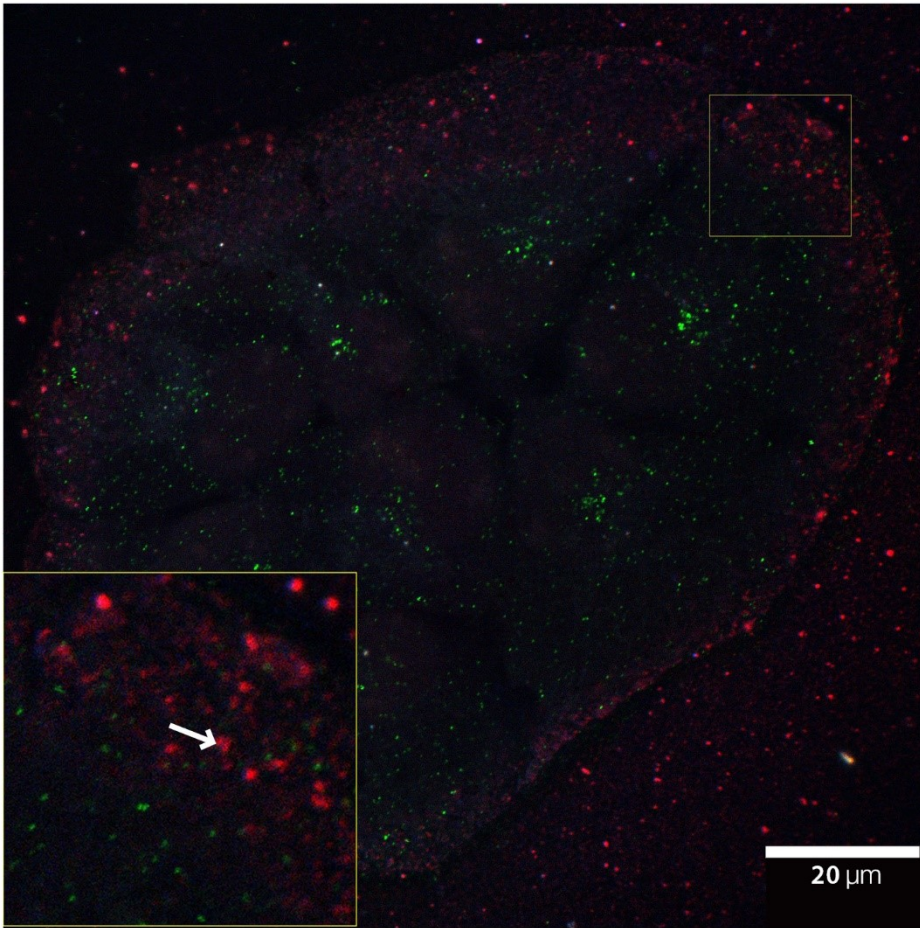


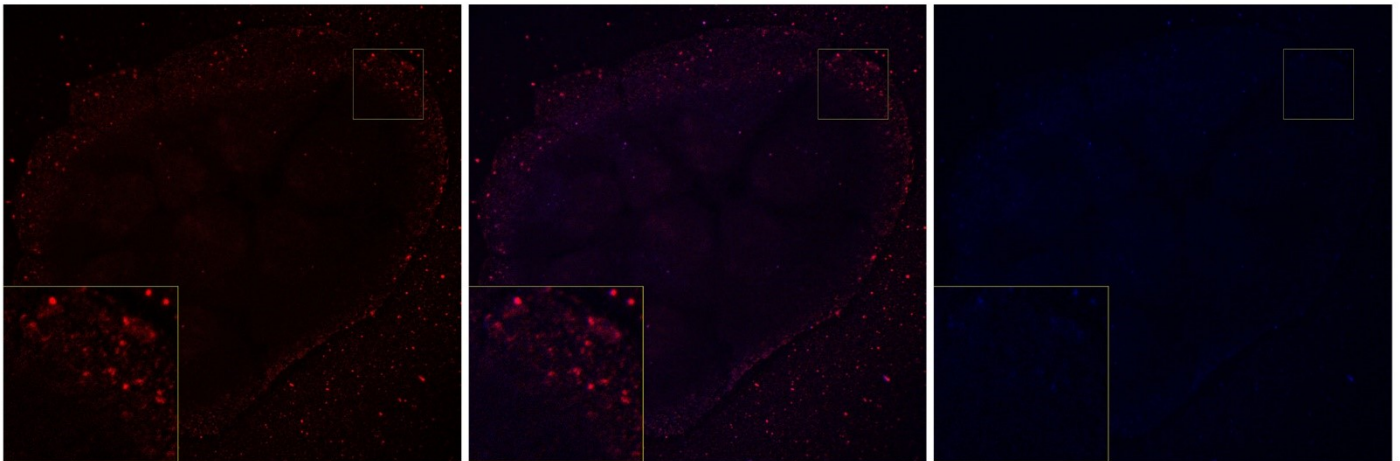
Figure 20: Time series EEA1, 15 minutes.

No significant colocalization between red NDs and green EEA1 was observed. Nanoparticles are mostly adhered around and on the cell membrane surface. None, however, are further inside the cells. Red NDs and siRNA tagged with blue dye are however significantly overlapping, indicating expected colocalization. Arrow indicates no overlapping between red and green signal.

ND

ND siRNA

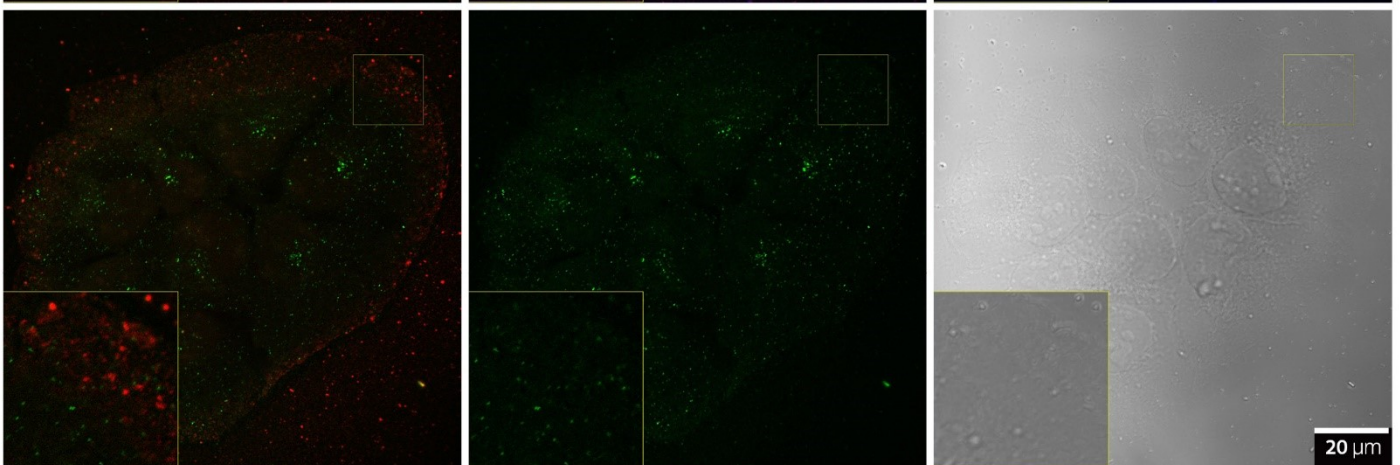
siRNA



ND EEA1

EEA1

BF



ND EEA1 siRNA

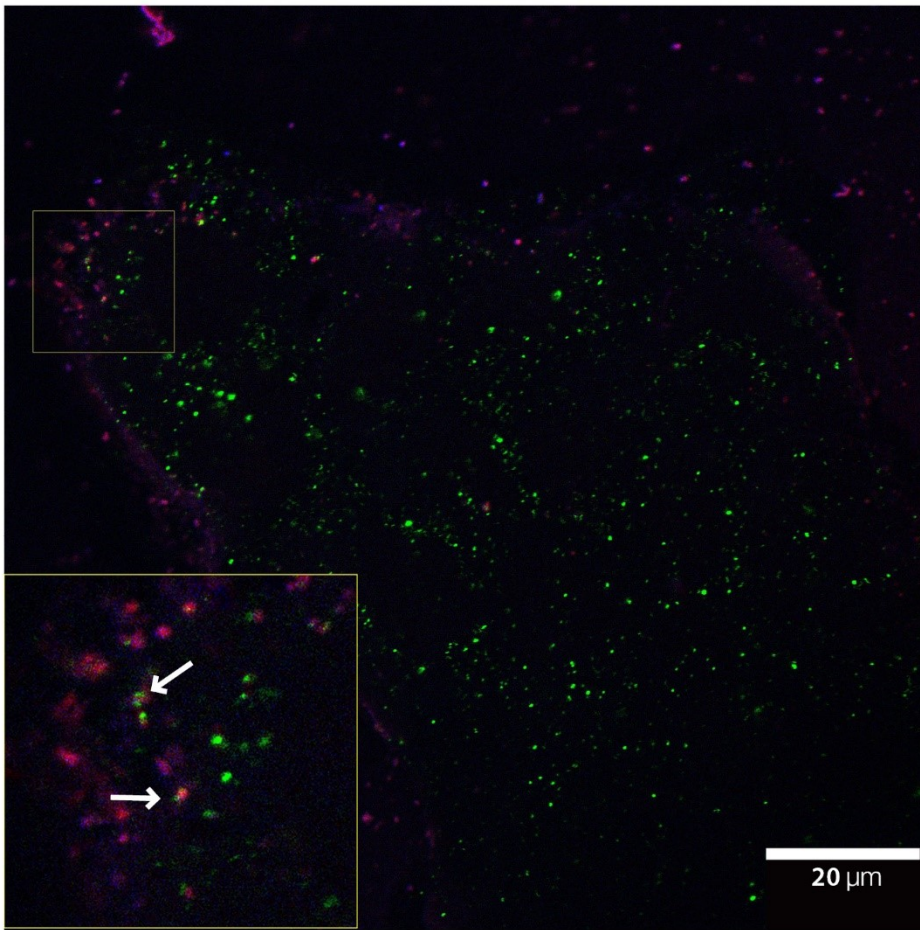


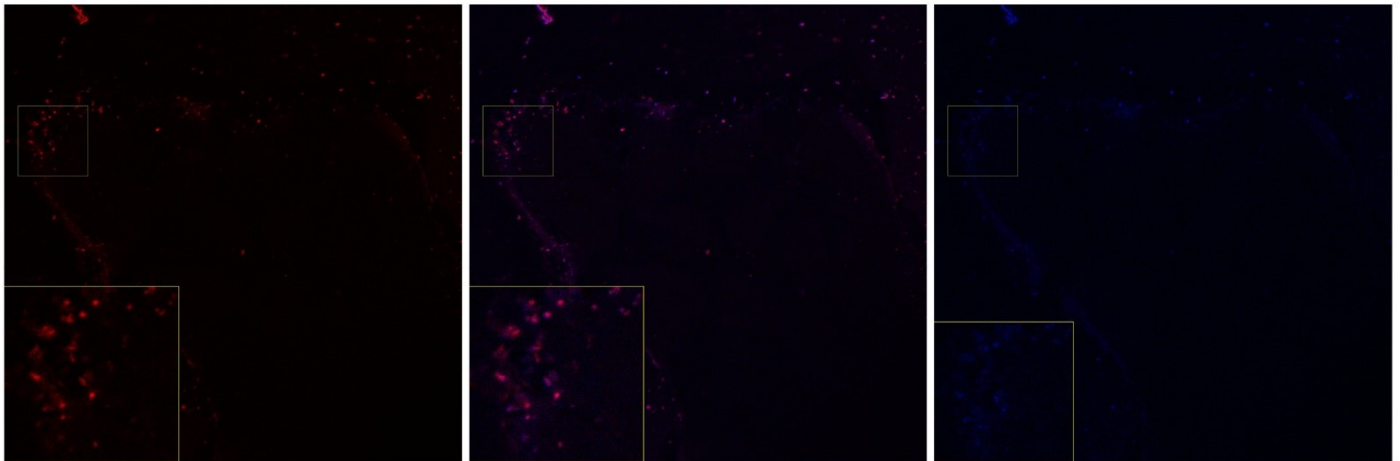
Figure 21: Time series EEA1, 45 minutes.

Red signal from NDs begins to overlap with green EEA1 signal of cell's early endosomes as indicated by the arrows inside the inlay. Dominantly, ND:siRNA complexes overlap with green EEA1s. Red ND signal and blue siRNA signal remain overlapping. ND and siRNA complexes were observed further inside the cells.

ND

ND siRNA

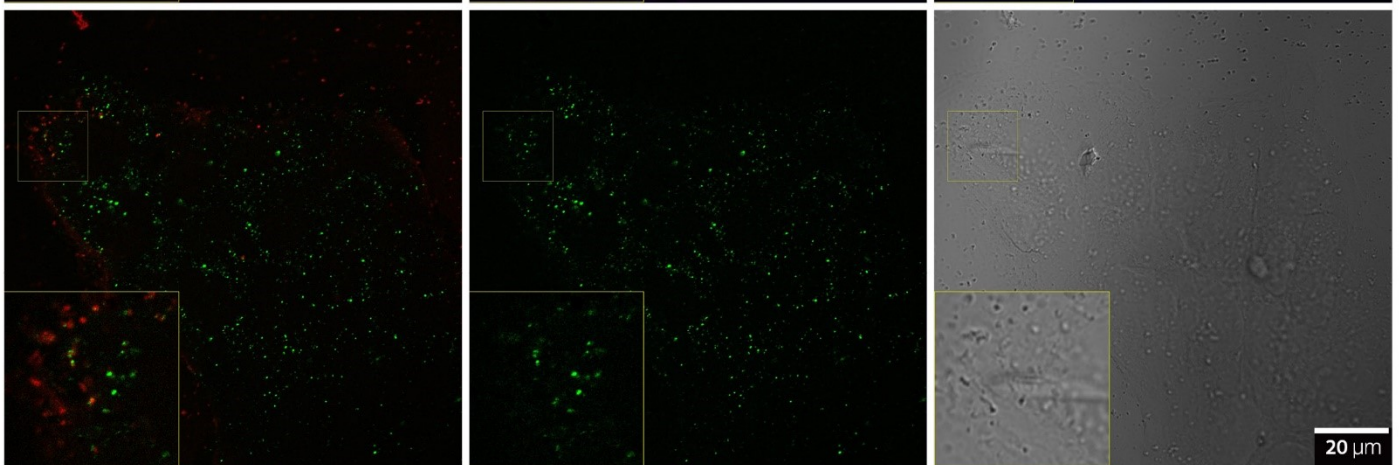
siRNA



ND EEA1

EEA1

BF



ND EEA1 siRNA

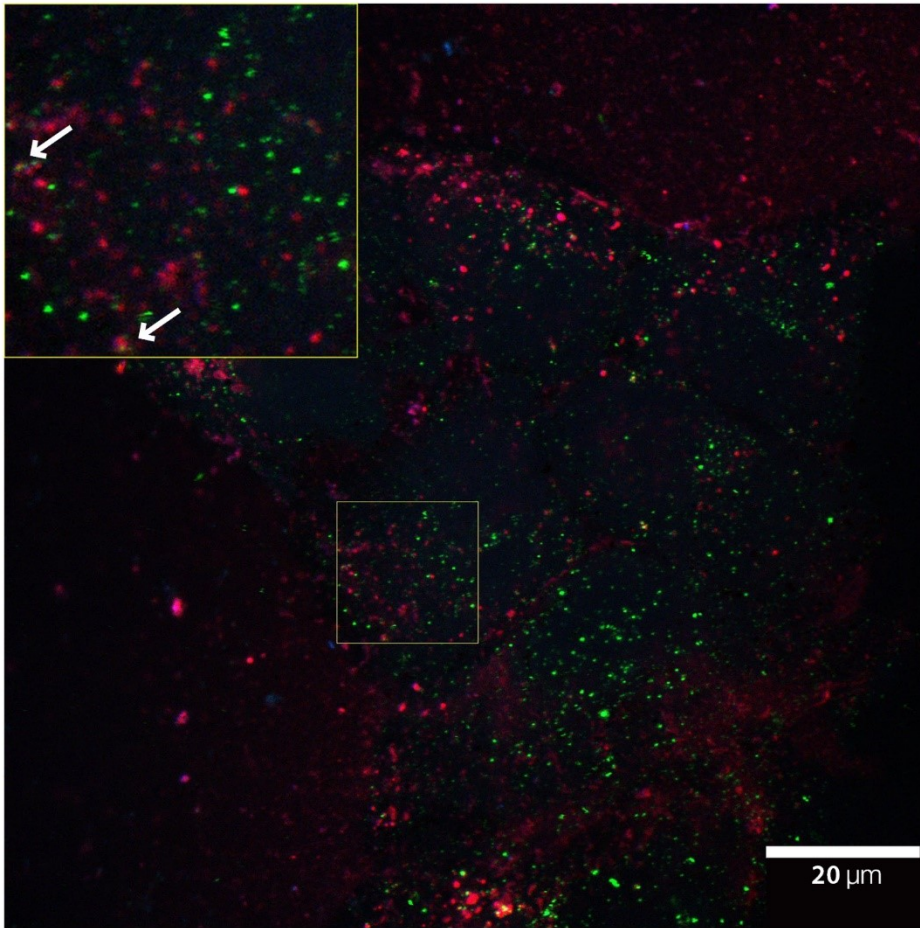


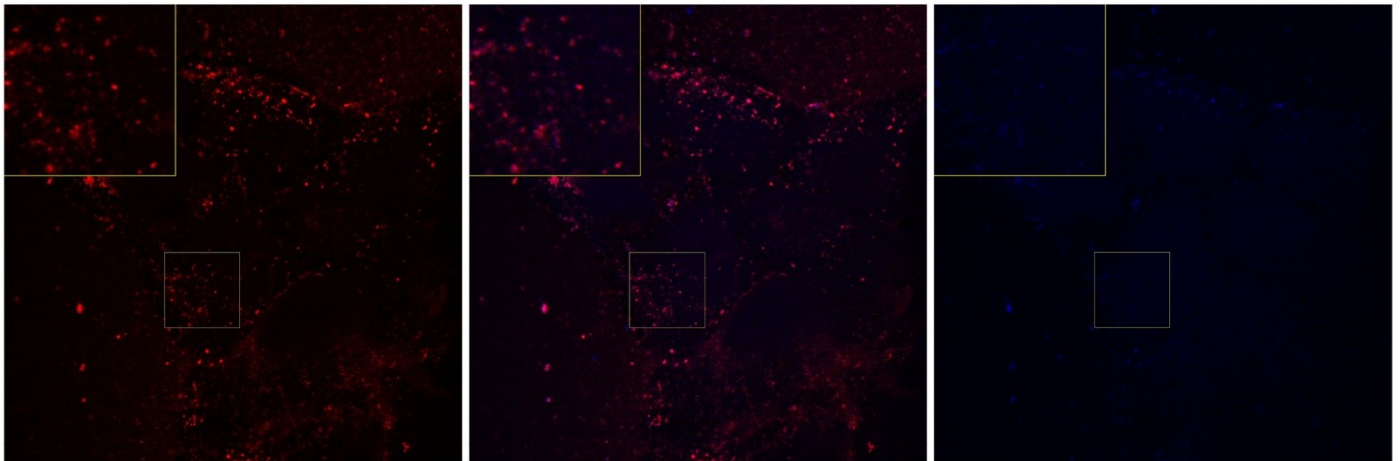
Figure 22: Time series EEA1, 90 minutes.

Red fluorescent NDs still overlap strongly with blue-labeled siRNA and also with green EEA1. However, Many NDs are free of green EEA1 as well and far more inside the cells in comparison with cells from previous time windows. White arrows point out overlaps in green and red channels.

ND

ND siRNA

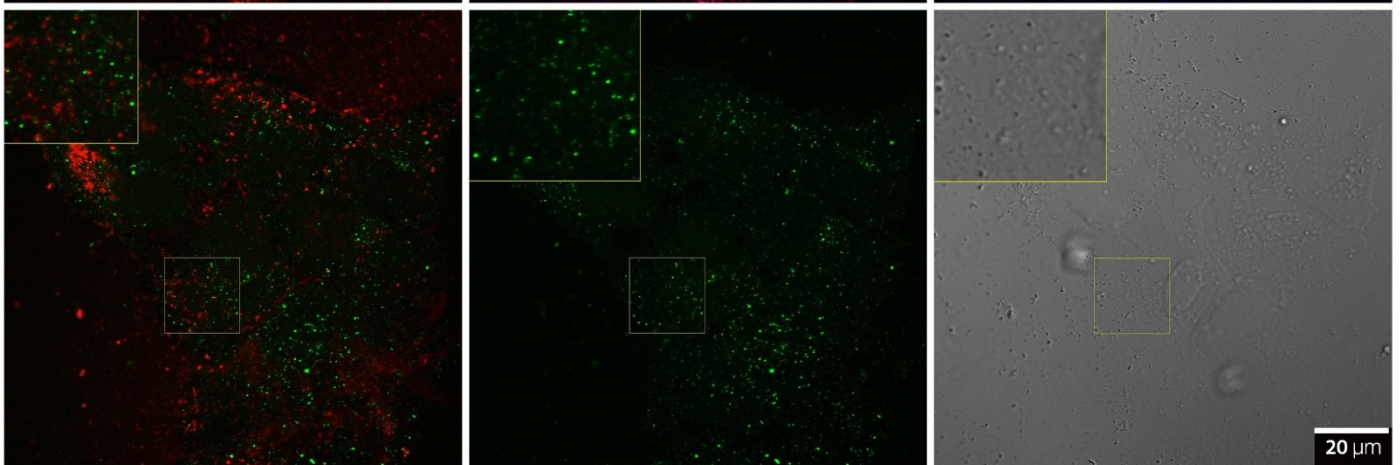
siRNA



ND EEA1

EEA1

BF



ND EEA1 siRNA

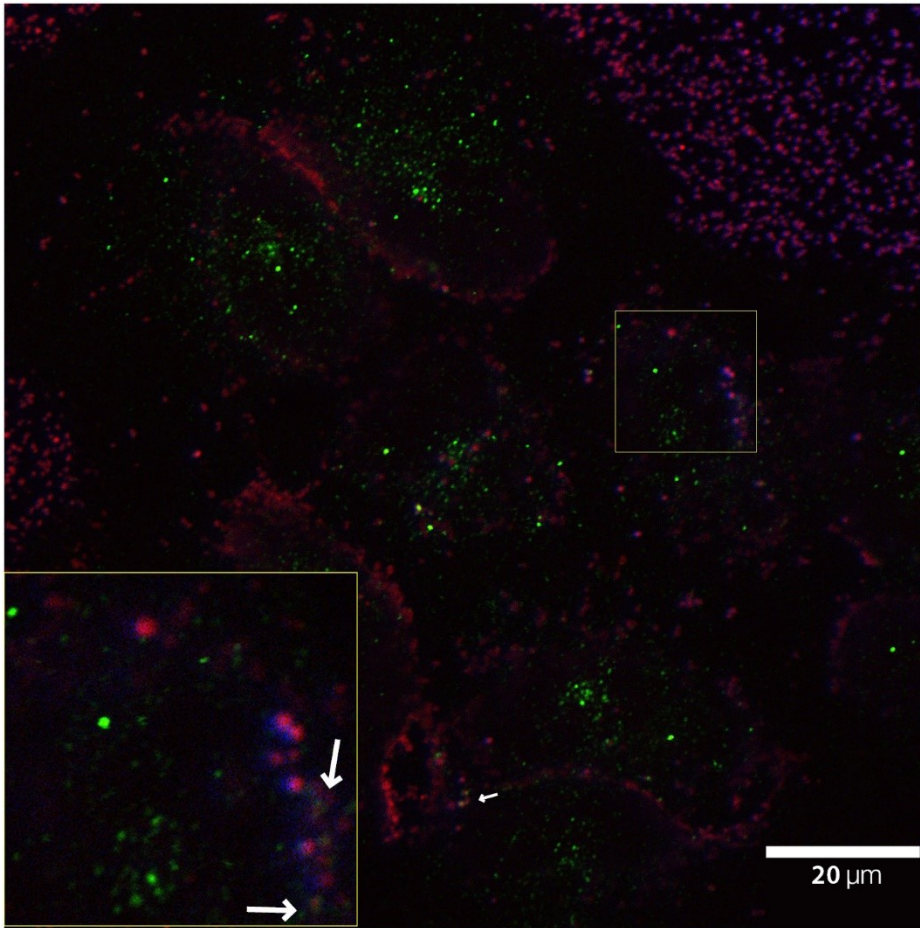


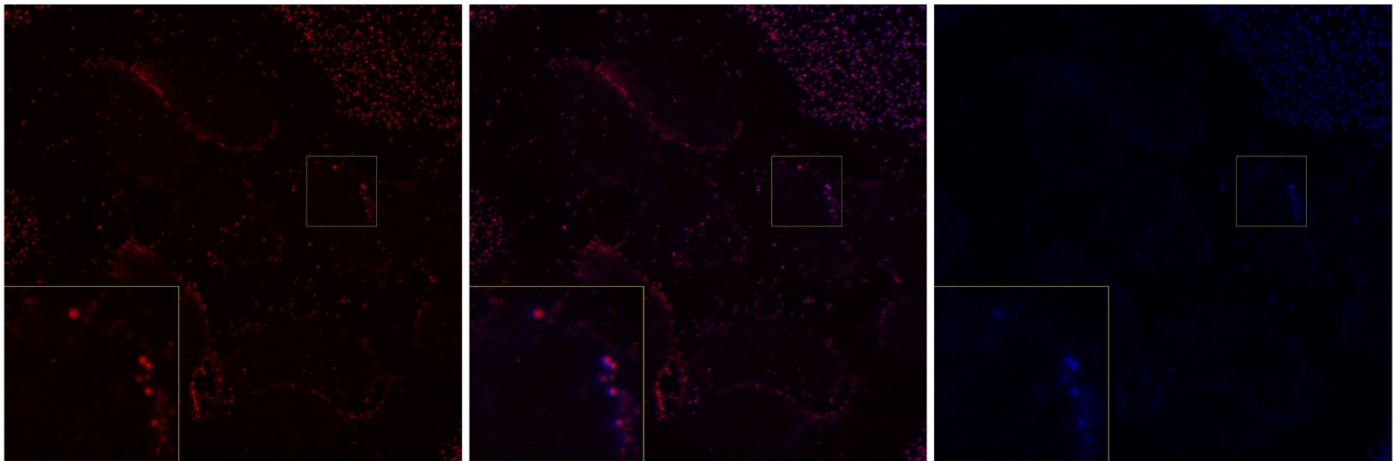
Figure 23: Time series EEA1, 120 minutes.

Similarly as in 90 minutes, NDs reach further from cell membrane inside the cell. Red ND signal overlaps with green EEA1s and still strongly with blue siRNA fluorescence signal.

ND

ND siRNA

siRNA



ND EEA1

EEA1

BF

20 μm

ND LAMP1 siRNA

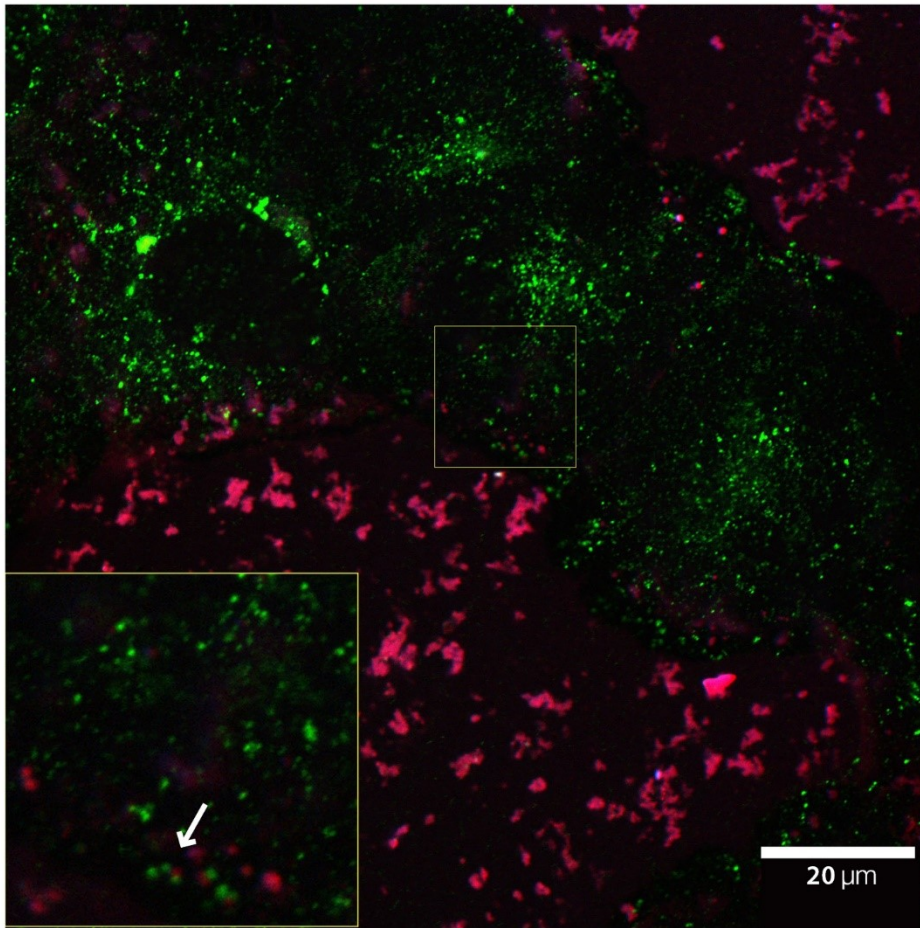


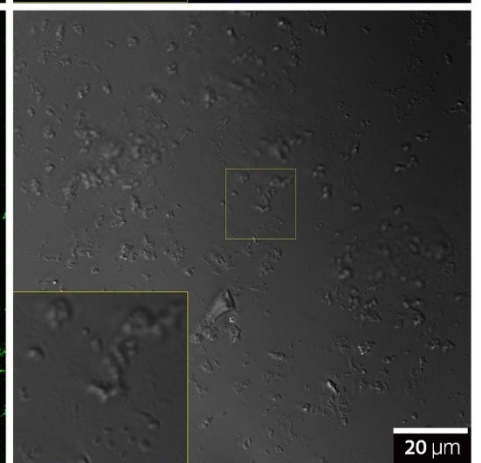
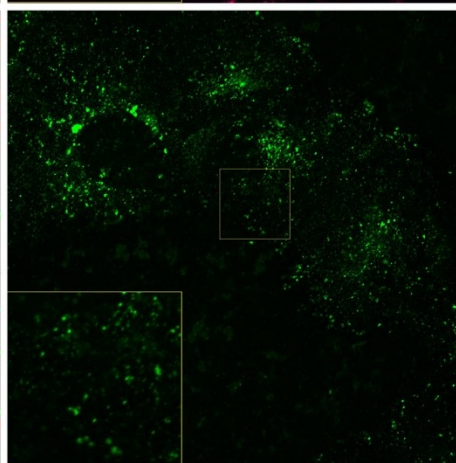
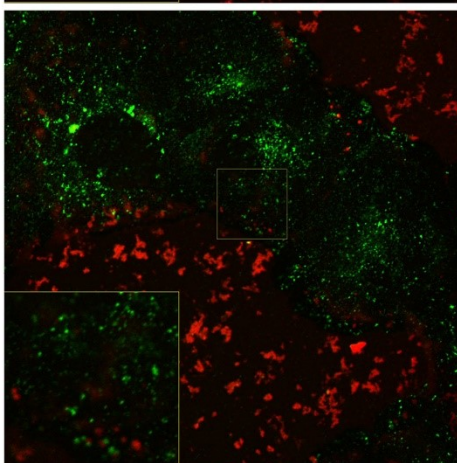
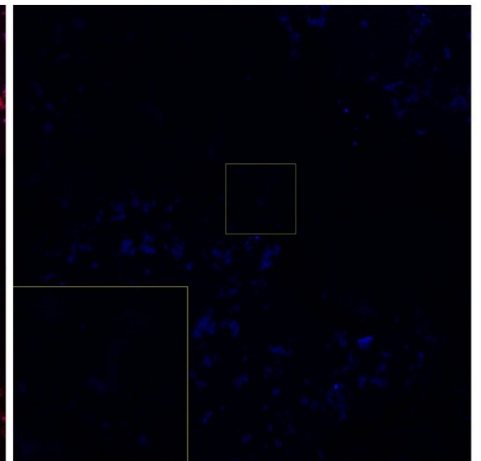
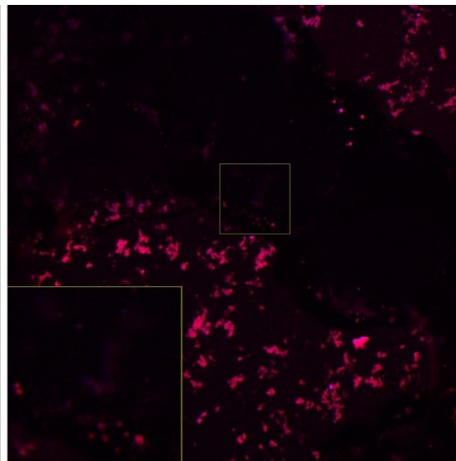
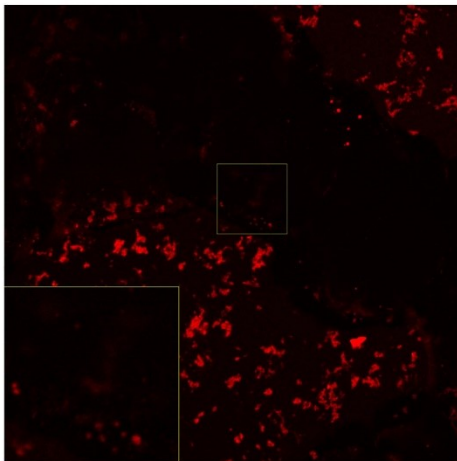
Figure 24: Time series LAMP1, 45 minutes.

Red NDs were observed within the cells, however no signal overlap was present. Nevertheless, red ND signal and blue siRNA signal were in a very close position to LAMP1 lysosomal markers as indicated by white arrow. Blue and red signal again colocalized strongly. Furthermore, large overlapping red and blue signals outside the cells were complex precipitates which seldomly form.

ND

ND siRNA

siRNA



ND LAMP1

LAMP1

BF

ND LAMP1 siRNA

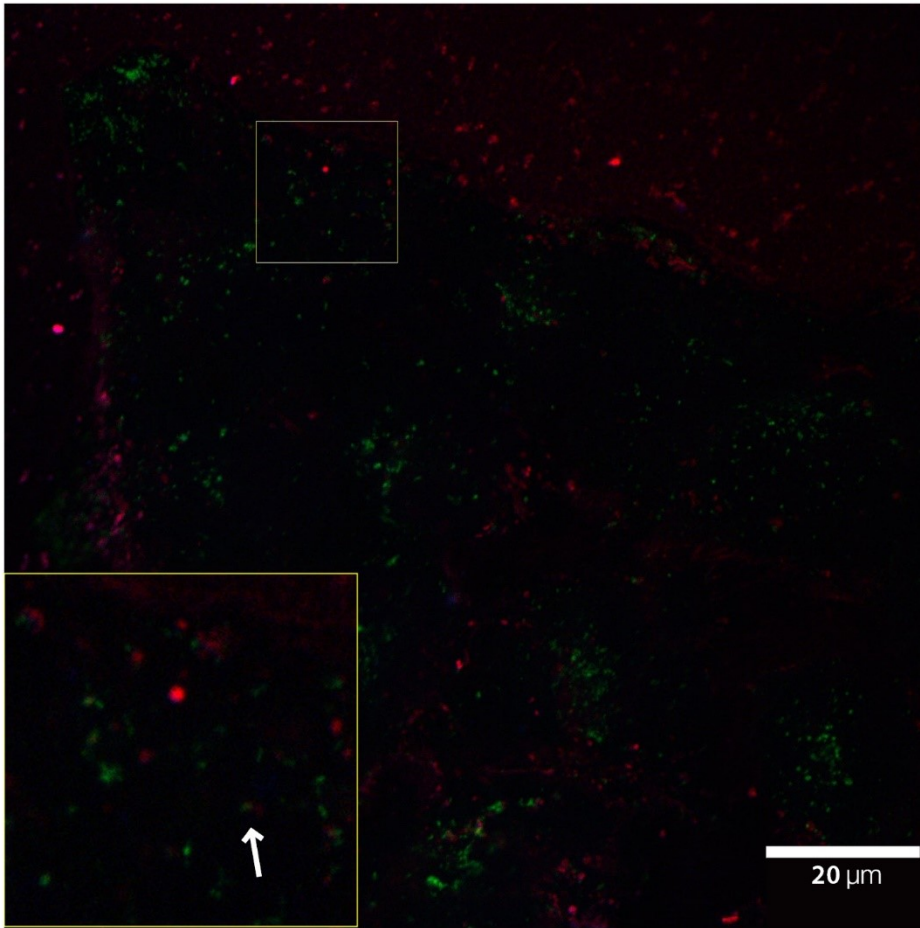
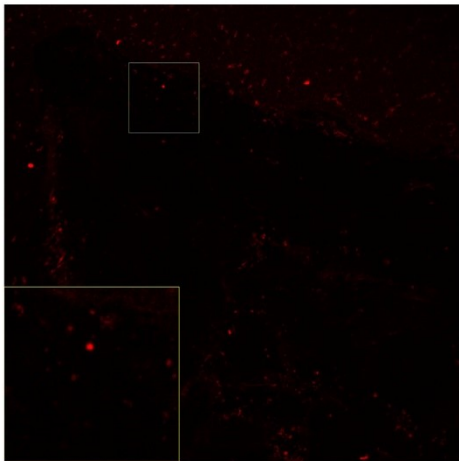


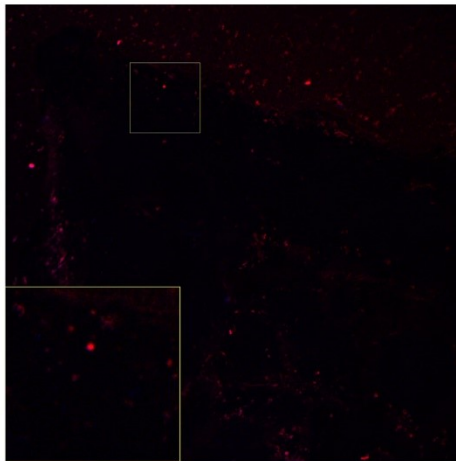
Figure 25: Time series LAMP1, 90 minutes.

Red and blue overlapping signals of NDs and siRNAs, respectively protruded inside the cells. Again, however, there was no significant signal overlap with green LAMP1, but similarly to previous time-point, often red and blue signals were in close vicinity of LAMP1 signals (white arrow.)

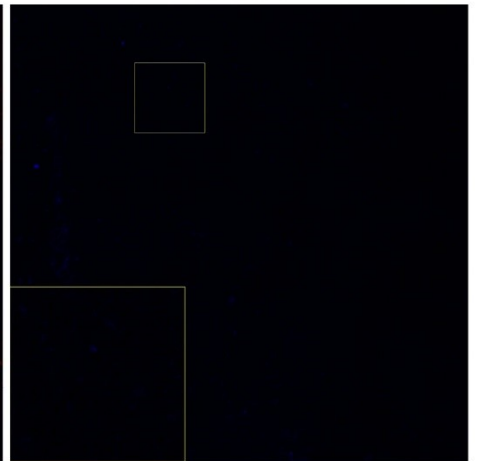
ND



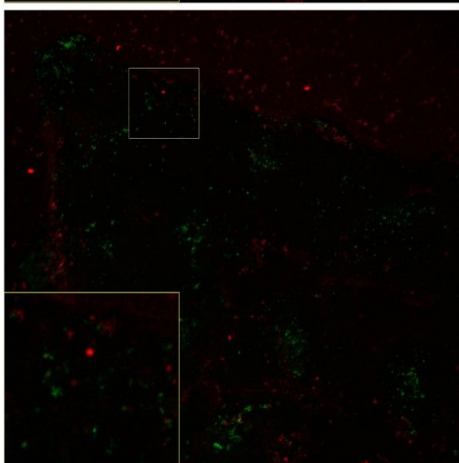
ND siRNA



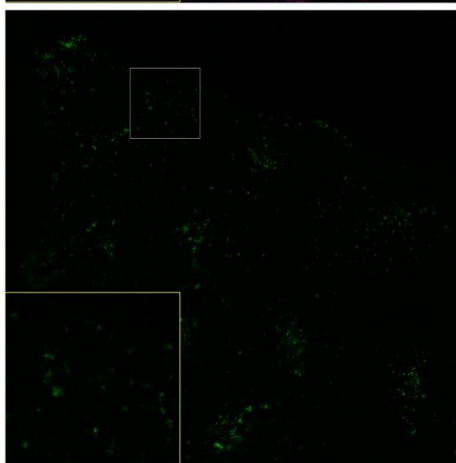
siRNA



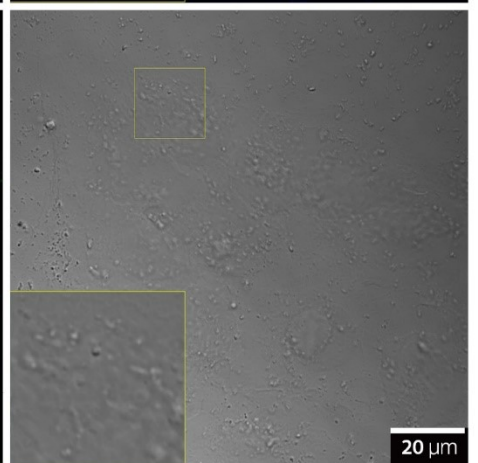
ND LAMP1



LAMP1



BF



ND LAMP1 siRNA

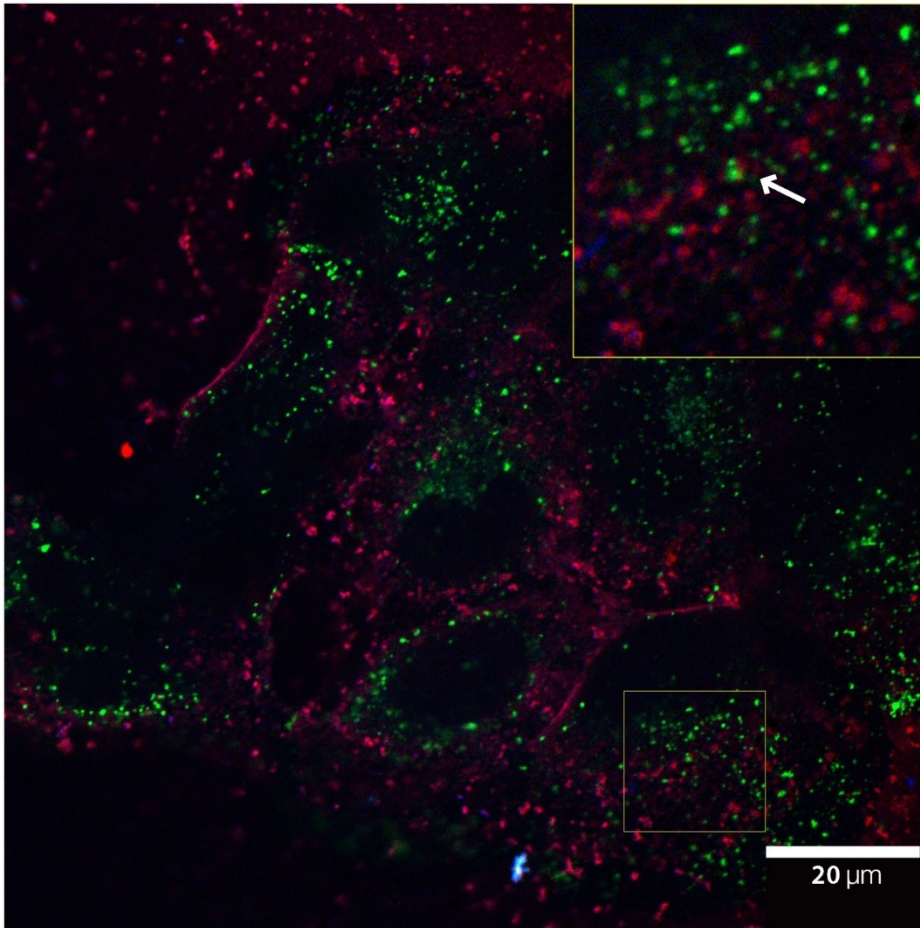
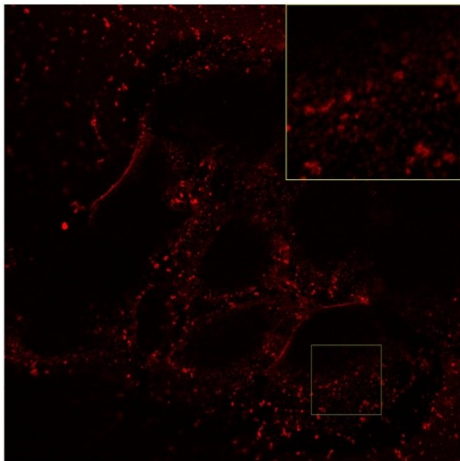


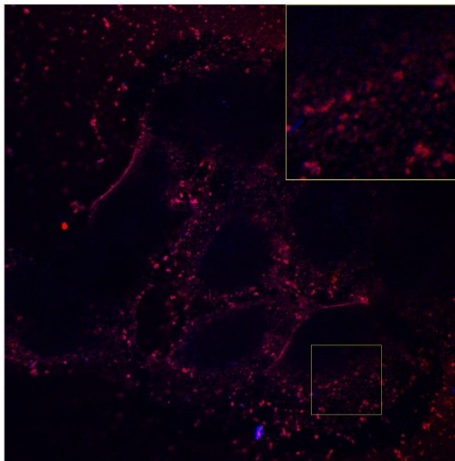
Figure 26: Time series LAMP1, 120 minutes.

Red ND and blue siRNA signals overlap outside and inside the cell similarly. There is no visible overlap between red and blue complexes with LAMP1 in green channel, however these signals are in a very close proximity from each other (white arrow.) ND and siRNA signal was observed throughout the cells.

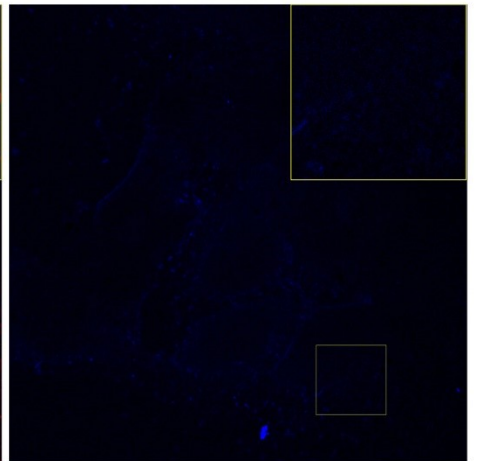
ND



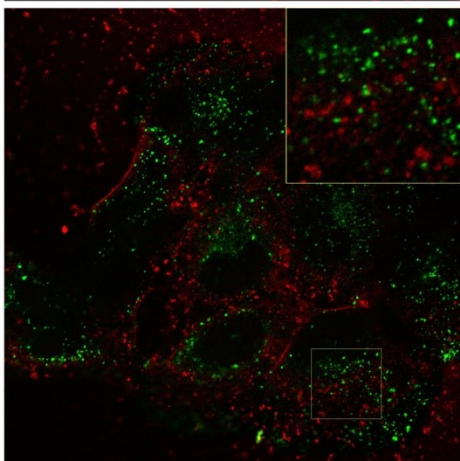
ND siRNA



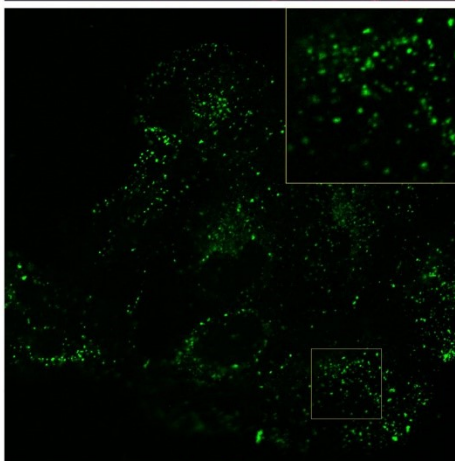
siRNA



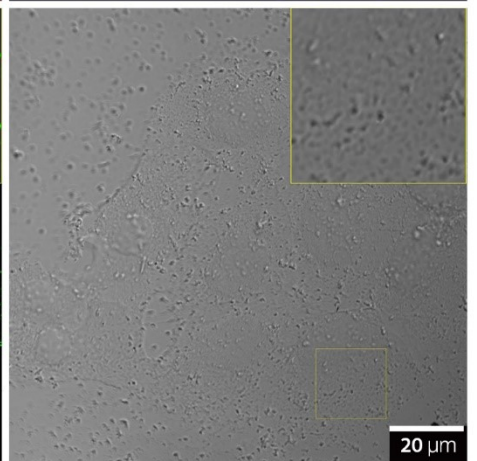
ND LAMP1



LAMP1



BF



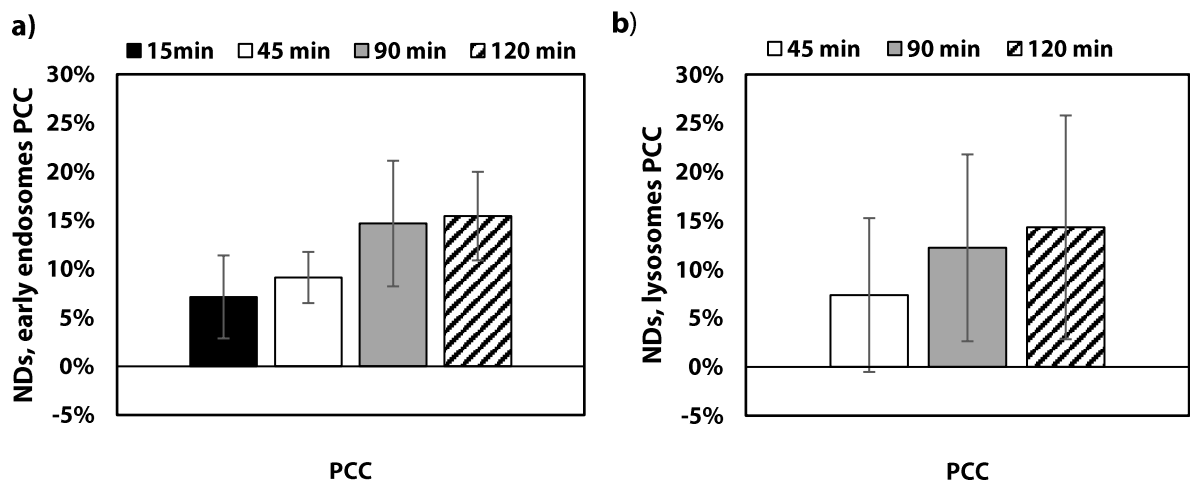


Figure 27: Quantified colocalization of NDs with endosomal structures. a) Colocalization expressed again with PCC between NDs and EEA1 raised from 7% (15 min) to 9% (45 min) and reached its maximum – 15% (90, 120 min). b) Correlation between NDs and LAMP1 followed a similar trend. 45 minutes into incubation, correlation reached 7%. After 90 and 120 minutes, correlation increased to 12% and 14%, respectively.

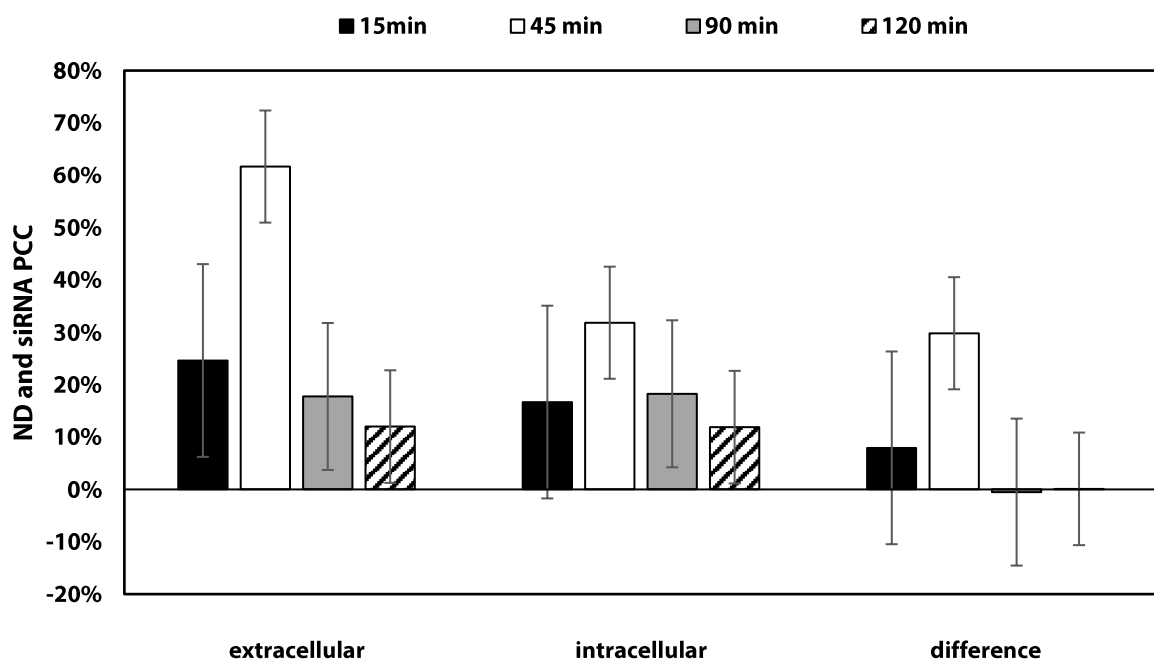


Figure 28: Extra- and intracellular colocalization of NDs and siRNA. Extracellular colocalization reached higher PCC than intracellular ND:siRNA colocalization in 15 min ($\Delta 8\%$) and 45 min ($\Delta 30\%$). However, in 90 min and 120 min both extracellular and intracellular colocalization levels equalized ($\Delta 0-1\%$) and decreased.

5. DISCUSSION

It has been well established that in order to achieve successful cell entry of NDs, size, and net charge of NDs must be taken into account (Harush-Frenkel *et al.*, 2007; Ryu *et al.*, 2017; Zhang *et al.*, 2017). Herein, 100 nm large NDs with novel polymer coating of a 1:3 ratio of DMAEMA and HPMA, respectively were prepared. Size of ND is crucial, because uptake of NDs is highly dependent on its diameter. CME poses upper limit of 280 nm for NDs and CavME sets the upper limit around 80 – 100 nm (Rausch *et al.*, 2019; Ryu *et al.*, 2017; Wang *et al.*, 2009). These NDs were well within the aforementioned diameter range of 30 – 280 nm for CME and CavME. Positive net charge of 45,5 mV in H₂O is sufficient enough to allow NDs to be captured on negatively charged cell membranes (Harush-Frenkel *et al.*, 2007) and also strong enough to create sufficient repulsive interactions between particles in colloidal solution (Zhang and Monteiro-Riviere, 2009). Our polymer coated NDs exhibited stable colloidal properties even after complexing with negatively charged siRNA in cell culture medium, as measured using dynamic light scattering (DLS). Similarly, Bertrand *et al.* prepared NDs with different polymer, although with similar surface charge and their complexes exhibited colloiddally stable properties as well (Bertrand *et al.*, 2015). However, during confocal microscopy imaging, clusters adhering to sample coverslips were observed. Extensive colloidal stability tests showed, that although NDs were colloiddally stable in medium, when temperature was raised to physiological level (37 °C), clusters began to form overtime. When fetal bovine serum was present in medium, measurements showed again 100nm stable particles. This finding is consistent with Hemelaar *et al.* findings. They proposed that introduction of NDs into a 100% serum solution creates a layer of coat which stabilized the ND complexes in cells (Hemelaar *et al.*, 2017). Despite these measurements, particle of heterogenous sizes (often well over 1 µm) were also occasionally observed in microscopy experiments. These sizes were over the limit for both examined types of endocytosis. Therefore, their endocytosis was highly improbable. Nonetheless, it still provides convincing proof that a large portion of ND complexes remains stable. Therefore, the majority of ND complexes remained colloiddally stable and was eligible for cell uptake.

5.1. Transfection efficiency of NDs

When U-2 OS cells were transfected with ND:siRNA complexes, the expression rate of GAPDH gene dropped down by 76%. Even though is not as effective as 90% gene knockdown mediated by RNAiMAX transfection, 76% GAPDH knockdown is within the range of well accepted levels of knockdown efficiencies (Andersen *et al.*, 2010; Phadke *et al.*, 2009). Furthermore, although NDs fell behind RNAiMAX by 14%, through modifications and further fine-tuning, such as aforementioned stabilization of complexes with FBS (Hemelaar *et al.*, 2017), NDs' transfection effectivity in U-2 OS cells could be boosted. Moreover, in starved cells, tranfection efficiency would likely increase since serum-free experiment and starvation of cells was reported to increase uptake of NDs (Fang *et al.*, 2011)

5.2. Impact of NDs on cell physiology

Even though RNAiMAX, a Lipofectamine® derivate, exhibited better transfection properties, Lipofectamine® is known for its adverse effects on cell viability (Yamano *et al.*, 2010). NDs are mostly referred to as non-toxic and biocompatible NPs (Moore *et al.*, 2016; Vaijayanthimala *et al.*, 2012). Herein, both statements were put to test and were proved true.

Both cytotoxicity and cell viability were assessed. Cytotoxicity was measured through LDH assay which indirectly measures cell membrane damage. WST-1 assay mediated results which on the other hand shed light on intracellular metabolic processes. NDs, in a concentration equal to qPCR experiments (35.4 µg/ml) exhibited the same results as positive controls within both LDH and WST-1 experiments. Positive controls in LDH assay exhibited low activity, because cell membranes were not damaged and did not leak enzymes into the medium. WST-1 positive controls exhibited high activity because intracellular enzymatic activity was measured. Therefore, they were evaluated as non-toxic to cells in consensus with previous studies.

qPCR-like concentration of RNAiMAX caused significant cytotoxic and antiproliferative effects on U-2 OS cells which was also in consensus with abovementioned study. Moreover, toxic effect equal to RNAiMAX was observed when high concentration of

NDs (141.6 µg/ml), used for microscopy imaging experiments, was introduced to cells. Although functional concentration of NDs was proved safe and non-toxic with two different methods, it is still possible adverse effects, can take place. Nonetheless, correspondingly to our results, other studies reported no cytotoxic effect of NDs by measuring of generating of reactive oxygen species and observing of stress-related genes upregulation (Hemelaar *et al.*, 2018; Solarska *et al.*, 2012). Long-term experiments are an option which already provided convincing data (Prabhakar *et al.*, 2017).

5.3. Uptake mechanism

qPCR experiments proved that NDs enter U-2 OS cells, where siRNA is released and through RNAi induces highly specific and effective gene knockdown. Release of siRNA molecules from the carrier is crucial. Otherwise RISC complex could not recruit siRNA for targeted mRNA degradation (Elbashir *et al.*, 2001; Meister *et al.*, 2004). Degradation causes gene expression downregulation which can then be measured through qPCR. Discrepancies between studies however point out that it is still unclear in which mechanism of uptake NDs partake. Generally accepted theory is that uptake is not exclusive to a single mechanism, but to several of them. Most discussed are CME and CavME (Faklaris *et al.*, 2010; Lin *et al.*, 2017; Zhao *et al.*, 2017). The different outcomes of previous studies could be well dependant on the previously mentioned NP parameters – size, shape and their charge, and cargo which is bound (DNA, siRNA, paclitaxel), as well as cell line used in the experiment and the coat which interacts with cell surfaces. For example, it was proved that albumin cell entry is dependent on CavME (Chatterjee *et al.*, 2017). Because serum albumin was used to boost ND stability in medium (Hemelaar *et al.*, 2017), it is plausible that because of the serum albumin coat on ND surface, the results were shifted towards CavME. Following this hypothesis, serum-free medium experiments could exhibit very different results, although Vaijayanthimala *et al.* observed no significant difference in ND uptake in serum-free and serum-supplemented media (Vaijayanthimala *et al.*, 2009).

5.3.1. Clathrin-mediated endocytosis

Dynasore-mediated endocytosis inhibition was successful since transferrin, which prevalently enters the cells through CME (Rodal *et al.*, 1999), was not present in Dynasore-treated cells in contrast with control cells. Based on these results, Dynasore was judged as effective enough inhibitor and therefore was used to inhibit clathrin endocytosis

. Based on visible reduction of NDs inside the cells treated with Dynasore. We judged that NDs in fact enter the cell by CME. CME was reported as a major contributor to uptake of lipid NPs, silica NPs and viruses (Gilleron *et al.*, 2013; Kapur *et al.*, 2012; Slowing *et al.*, 2008). Indeed, this conclusion was reached in numerous studies, where CME is considered as the main cell entry mechanism (Alhaddad *et al.*, 2012; Faklaris *et al.*, 2009; Vijayanthimala *et al.*, 2009).

However, the Dynasore concentration was extremely high in contrast with other studies, where effective concentration revolved around 40 – 80 μM (Girard *et al.*, 2011; Kälin *et al.*, 2010). This fact raised a question. Does the extremely high concentration inhibit all forms of endocytosis? Although Dynasore should be CME specific, it's not fully clear whether mechanism of action interferes with dynamin (Macia *et al.*, 2006). Moreover, dynamin could be required in CavME as well to cut off the elongating caveolae bulbs. Furthermore, it was already reported that in high concentration Dynasore tends to bind membrane cholesterol molecules and thus interfere with proper membrane raft assembly (Preta *et al.*, 2015). This effect supports the plausible non-specific inhibition caused by Dynasore. Lastly, quantified data on both Filipin-treated and Dynasore-treated cells exhibited the same approximately 30% downregulation of ND uptake. Therefore, if Filipin's specific inhibition was responsible, for larger portion of ND endocytosis inhibition, Dynasore's potential nonspecific effect would render Dynasore as falsely positive CME endocytosis inhibitor. Interesting follow-up strategy to test this hypothesis would be using both inhibitors at the same time. Hypothetically, the inhibition should increase or even double. However, previous studies often concluded only CME or CavME as uptake contributors. Nonetheless, they used different inhibitors (e. g. methylated- β -cyclodextrin and sucrose) (Zhao *et al.*, 2017), therefore different results could be

reached with different inhibitors even when they should target against the same endocytic pathways. Because most of the ND uptake was not inhibited, other cell uptake mechanisms should be examined. Secondly, the prepared NDs were close to the upper limit of both CME and CavME. Therefore, macropinocytosis should be examined as a perspective option on ND cell entry. For example, it was proved that endosomal structures formed from macropinocytosis cell uptake ranged in sizes between 0.2 – 5 μm (Swanson and Watts, 1995) and within which NDs were already observed (Bertrand *et al.*, 2015)

5.3.2. Caveolin-mediated endocytosis

Filipin was successfully used to inhibit caveolae-mediated cell entry of NDs. In contrast with Dynasore concentration, final concentration was well within concentration range of already published work (Bissig *et al.*, 2012; Rejman *et al.*, 2005) However, inhibitory effect was not well visible on microscopy images, because fluorescent signal from NDs is still well visible inside the cells and in colocalization with cytoplasmic Cav-1 even in Filipin treated cells. Albeit, recent research showed that U-2 OS cells express caveolin-1 and utilize CavME (Rausch *et al.*, 2019). Nevertheless, after quantification a conclusion was reached that roughly 30% of NDs entered the cell through CavME.

In order to follow this hypothesis a positive control is necessary. Probes albumin with fluorescent tag (Chatterjee *et al.*, 2017) and fluorescently labelled Cholera Toxin subunit (Orlandi and Fishman, 1998) which were expected to enter the cell through CavME were either not entering the cell at all or were observed only on cell membrane, respectively. Because fluorescent controls were not observed inside cells, either cell line or albumin require substitution in order to thoroughly execute the experiment.

5.4. Uptake rate and colocalization with intracellular structures

Although there are many divergent opinions on endocytosis mechanism of NDs, their colocalization with intracellular structures was almost uniformly proved. After endocytosis, NDs were observed in early endosomes and subsequently in lysosomes (Alhaddad *et al.*, 2012;

Wang *et al.*, 2015; Zhao *et al.*, 2017). However, Shvets *et al.* discussed the possibility that at least partially endosomes of CavME follow different pathway and never interact with early endosomes (Shvets *et al.*, 2015). Our results confirm that partial colocalization between NDs and early endosomes, and NDs and lysosomes is indeed present. In the context of intracellular membrane vesicles, the ND shape is hypothesized to be crucial. Chu *et al.* proposed that NDs escape vesicular sorting system before it reaches lysosomes through membrane penetration (Chu *et al.*, 2015). Herein, NDs complexed with siRNA were observed on a fixed time scale, to determine at which point of ND:siRNA complexes route endosomal escape occurs.

Rather than using total fluorescence intensity for measurement of uptake (Lin *et al.*, 2017; Vaijayanthimala *et al.*, 2009; Zhang *et al.*, 2017), each particle was analysed through ImageJ Fiji plugin Analyse particle, within which minimal and maximal size parameters for particles were set up (Hemelaar *et al.*, 2018). This setup excluded any background to be accounted for as ND. This was done after background subtraction and fluorescence threshold setting. After 15 minutes, the data showed already 0.6% of total cell area taken with NDs, which was already 30% of the particle count maximum which took place at 90 minutes timepoint. Rather than early rise in endocytosis in the first 15 minutes, this could be a methodical or technical error. An error, it was impossible to distinguish between particles adhered to cell membranes in the medium and particles already internalized, based on confocal microscopy images, even though cell edges were precisely determined. Studies reported visibly internalized NDs after 1 hour of incubation (Alhaddad *et al.*, 2012; Schrand *et al.*, 2011), Zhang *et al.* reported intracellular ND signal 30 minutes after incubation (Zhang *et al.*, 2017). Our results exhibit that uptake started between 15 and 45 minutes. Largest uptake rate was then observed between 45 and 90 minutes. At 120 minutes, the signal decreased, indicating that NDs can exit the cells through exocytosis. This is plausible because observations of ND exocytosis were reported 1-48 hours after incubation with NDs in previous studies (Fang *et al.*, 2011; Prabhakar *et al.*, 2017).

In order to measure colocalization of NDs with early endosomes and lysosomes, immunofluorescence staining was executed with antibodies against Early Endosome Antigen-1

and Lysosomal Associated Membrane Protein-1, respectively. Nevertheless, partial overlap and close proximity between NDs and endosomes were visible already after 15 minutes of incubation. We presumed that these events could indicate colocalization. Even though labelled endosomal tag did not overlap directly with NDs, marked endosomal structure could still encapsulate ND. Number of these close proximity events increased with time, likely because of increasing ND occurrence due to ND uptake. Indeed, after quantification of PCC calculation, colocalization of NDs with early endosomes raised with time and started reaching plateau in 90 minutes. These results also correlate with increased uptake of ND. Following the same increasing trend, colocalization rate between NDs and lysosomes raised with time as well. Furthermore, with the decrease in intracellular ND particle count at 120 minutes, colocalization with early endosomes possibly reached plateau. With decrease in ND uptake rate, the number of NDs passing through early endosomes most likely lowered, too. However, this trend was not observed in colocalization quantification of lysosomes and NDs. The concentration of NDs inside lysosomes was presumably not changing because there was obviously a time period before NDs from early endosomes reached lysosomes.

We know that early endosomes act as sorting points of all endocytic processes before the cargo reaches late endosomes and finally lysosomes (Jovic *et al.*, 2010). Interestingly, the maximum colocalization values suggested that 16% of NDs was present in endosomes and 14% in lysosomes after 120 minutes of incubation. These results were surprisingly low since early endosomes were expected to be responsible for most of post-endocytosis sorting. These results indicate that a large percentage of NDs entered the cell through different mechanism or that NDs escaped the endosomes in very early stages after endocytosis. However in another study, NDs were observed to colocalize up to 80% in the first hour of incubation with early endosomes. In this study, cells were pre-treated with NaN₃ or starved in serum-free medium at 4°C for 3 hours. These harsh conditions (in contrast to our established methods) could have had significantly adverse effect on cell physiology (Chu *et al.*, 2014). Similarly to our 16% PCC results, Faklaris *et al.* reported 21% colocalization with early endosomes. Lysosomes were proposed to be another cellular compartment where NDs could agglomerate (Faklaris *et al.*,

2008). However, our results proved that lysosomes are not organelles in which NDs were abundantly observed. On the other hand, multiple studies show that NDs indeed travel to lysosomes after 3 to 6 hours after start of incubation (Prabhakar *et al.*, 2017; Wang *et al.*, 2015; Zhao *et al.*, 2017). Hence, in order to achieve colocalization of NDs with lysosomes, experiments with longer incubation times are necessary. Moreover, early escape of NDs could be associated with their irregular and “pointy” shape (supplementary fig. 2) in consensus with already published findings on difference between irregular, “pointy” and etched, smoothed shapes of NDs (Chu *et al.*, 2015).

Furthermore, during filipin experiments, protein Caveolin-1 was observed as an endogenous marker. Acquired confocal microscopy images showed that after 60 minutes of incubation with NDs, control cells and DMSO-treated cells, NDs’ fluorescent signal visibly overlapped with Caveolin-1. Indeed, image data quantification showed that NDs colocalized with Cav-1 in 23% which is in fact about 10% higher than PCC correlation data on early endosomes colocalization. Correspondingly, Zhao *et al.* reached conclusion that NDs indeed enter the cell through clathrin-independent pathway, specifically through caveolae (Zhao *et al.*, 2017). However, caveolae vesicle derivatives should still pass through early endosomes (He *et al.*, 2015), although a sizeable group of Cav-1 positive vesicles was hypothesized to follow a pathway which does not involve early endosomes (Shvets *et al.*, 2015). A reason which could explain these results is that most of the NDs escape in between Caveolin-tagged vesicle and early endosome. Lesser amount would then escape during their advance between early endosome and lysosome. Still, more than 50% of NDs inside cells is not found to colocalize with expected and examined intracellular structures. Although Chu *et al.* reported 80% signal overlap between NDs and early endosomes, unlike our setup, they starved their cells prior to ND incubation (Chu *et al.*, 2014). If the early escape hypothesis was in fact true, this would be highly beneficial for further ND research in drug delivery owing to NDs’ hypothetical highly effective cytoplasm localization and escape from degradation pathway (Bertrand *et al.*, 2015; Lim *et al.*, 2016).

5.5. Colocalization of NDs with siRNA: siRNA release

In order to induce knockdown through RNAi, siRNA must escape endosomes dissociate from NDs to be recruited by RISC complex which is localized outside endosomal structures (Liu *et al.*, 2005). Similarly, it was proven that DNA, which is delivered to nucleus, dissociates from nanoparticles and subsequently undergoes transcription (Roy *et al.*, 2005). siRNA was bound to NDs through electrostatic interaction. In order to observe dissociation of siRNA from NDs, siRNA covalently modified with Atto425 was used. Prior to confocal microscopy experiments, modified siRNAs' gene knockdown properties were compared to those of non-modified siRNA. Both resulted in a comparable gene silencing effectivity. In order to gain insight on siRNA release of NDs, again colocalization between ND and siRNA was quantified in time.

For siRNA dissociation analysis, we decided to measure the decrease in colocalization of siRNA and NDs outside and inside the cell. We normalized the intracellular colocalization data to the extracellular colocalization data, i. e. we subtracted the PCC values of intracellular PCC from extracellular PCC values. Difference in colocalization intensity showed that colocalization dropped by 30% after 45 minutes of incubation inside the cells. This suggests that siRNA is either released during this period or cells simply engulfed lower amount of NDs in comparison to newly sedimented NDs. However, siRNA clearly started to dissociate from NDs between 45 and 90 minutes. Petrakova *et al.* observed this release already after 30 minutes of incubation (Petrakova *et al.*, 2016). This early time of release is interesting in contrast to already observed DNA release from polymers and particles. He *et al.* observed significant fluorescently labelled DNA dissociation from NPs after 3 hours. González-Domínguez *et al.* observed 66% PCC of PEI with fluorescently labelled DNA dissociation after 10 hours (González-Domínguez *et al.*, 2019; Roy *et al.*, 2005). It is impossible to confirm or confute this because of the sudden increase in colocalization in 45 minutes time point. It is not clear why the outside colocalization rate decreases in the next 45 minutes to the same level as intracellular colocalization values and why the total colocalization of both outside and intracellular complexes remains very similar – around 20% - later on. Early release and reaching of plateau state of PCC could be likely attributed to a prompt cargo release after endocytosis (He *et al.*, 2016). Moreover, after 15

minutes of incubation, both extra- and intracellular colocalization values are very low, while suddenly 30 minutes later, colocalization shoots up in extracellular environment and in smaller leap inside the intracellular environment, too. Then total colocalization rates on both sides of cell membrane steeply decrease in time. There are two possible explanations. Sudden increase of absolute PCC values was presumably caused by already discussed overtime cluster formation in the field of view. siRNA did not likely bind to NDs homogenously; i. e. siRNA did not form complexes with all the NDs equally. Because it was shown that a fraction of ND:siRNA complexes collapsed and sedimented even in serum supplemented medium overtime, first NDs taken up by the cell (15 minutes) were more stable because less siRNA molecules was bound to them. Later (45 minutes), clusters could comprise of higher amount of fluorescently labelled siRNA than colloiddally stable complexes. Colocalization evaluation conducted in Fiji would then hypothetically, assign higher values to NDs with more labelled siRNA molecules attached. Presumably, these complexes were taken up by cells too. Second and non-contradictory explanation is that Atto425, fluorophore covalently attached to each siRNA molecule emitted fluorescence signal far into the green light spectrum in addition to the blue light spectrum. This could not be sufficiently unmixed through linear unmixing upon creating lambda scans. This resulted in bleed-through in both green and blue channel. Therefore, even at the earliest time point, seeming siRNA signal in blue channel could have been for example signal of early endosome and *vice versa*. Both of these reasons could partially clarify, why ND:siRNA complexes did not reach full 100% PCC value. Notably, in study using PEI polymer, near-100% PPC values were achieved. Inside cells, this value decreased only to 66% after 10 hours. This slow release could likely be attributed to different binding forces and sizes in PEI:DNA complexes (González-Domínguez *et al.*, 2019). Another reason why 100% colocalization was never reached is that the blue and the rest of channels are shifted to one another. This is because of a different positioning of UV excitation laser and laser exciting other than blue fluorophores. For further experiments, best possible solution would be to divide experiments into two with only two probes present in order to avoid bleed-through. However, this experiment plan does not allow for direct endosomal escape of siRNA.

Method avoiding the necessity to label siRNA is measurement based on shift in ND emission spectrum based on switching two charged states of NV-centers. The particular state is influenced by the charge of nearby molecules. Therefore, presence or absence of siRNA would cause fluctuation in intensity approximately at 638 nm in this spectrum (Petrankova *et al.*, 2015). However, this was impossible to achieve using available microscopy setup, albeit the observed fluorescence intensity should fluctuate by approximately 1/3 of its lower intensity state (Petrankova *et al.*, 2016).

6. CONCLUSIONS

NDs are in a spotlight owing to their interesting physical attributes. Herein, we utilized NDs NIR photoluminescence properties which make them a promising bioimaging platform in nanomedicine. Furthermore, NDs were already used as probes and cargo carriers in drug and nucleic acid delivery. In this study, transfection efficiency and biocompatibility of NDs were examined. Additionally, endocytosis of NDs and their subsequent intracellular fate were analyzed.

We have successfully prepared biocompatible NDs with a novel mixture of polymers which can electrostatically complex with siRNA. These complexes mediated significant gene expression knockdown in U-2 OS cells. Moreover, NDs exhibited high biocompatibility as shown by cytotoxicity and cell viability assays and are in fact suitable for further development towards clinical applications.

Furthermore, we observed NDs in fixed cells in order to determine mechanism of entry and their intracellular fate. Through specific endocytosis inhibition in U-2 OS cells, we observed an equal decrease in uptake of NDs when we inhibited both CME and CavME. Hence, we propose that NDs could enter the cell through CavME and CME comparably well. Nevertheless, the concentration of CME inhibitor Dynasore was extremely high in comparison with previous studies. Despite this, entry mechanism of more than 50% of intracellular NDs is still unknown, but based on a thorough literature review, we hypothesize that macropinocytosis is responsible for ND uptake, too.

After endocytosis, NDs with siRNA are engulfed in vesicles, particularly in early endosomes. In order to induce gene expression knockdown through RNAi, siRNA must be

recruited by cytosolic RISC complex. We proved that NDs indeed colocalize with early endosomes and lysosomes. Moreover, we observed slightly higher colocalization of NDs in caveolin-derived endosomal structures. This observation supports the hypothesis NDs enter cells through CavME which does not follow conclusions of most recent studies on ND uptake. Additionally, we propose that these NDs could escape endosomes early after internalization, as we did not observe a large portion of NDs in any labelled endosomal structure. This would be highly beneficial for their further development in disease treatment. Finally, we observed significant dissociation of siRNA from NDs after 45 minutes of incubation. However, technical obstacles may have influenced the results and further research is required in order to reach clear conclusions.

In this work, we successfully determined entry mechanism of NDs and their subsequent intracellular localization. Based on demonstrated results, we believe NDs biocompatibility and transfection properties make NDs suitable candidates for further research and clinical use.

7. BIBLIOGRAPHY

- Acosta, V.M., Bauch, E., Ledbetter, M.P., Waxman, A., Bouchard, L.-S., and Budker, D. (2010). Temperature Dependence of the Nitrogen-Vacancy Magnetic Resonance in Diamond. *Phys. Rev. Lett.* *104*, 070801.
- Alhaddad, A., Durieu, C., Dantelle, G., Le Cam, E., Malvy, C., Treussart, F., and Bertrand, J.-R. (2012). Influence of the Internalization Pathway on the Efficacy of siRNA Delivery by Cationic Fluorescent Nanodiamonds in the Ewing Sarcoma Cell Model. *Plos One* *7*, e52207.
- Andersen, N.D., Chopra, A., Monahan, T.S., Malek, J.Y., Jain, M., Pradhan, L., Ferran, C., and LoGerfo, F.W. (2010). Endothelial cells are susceptible to rapid siRNA transfection and gene silencing ex vivo. *J. Vasc. Surg.* *52*, 1608–1615.
- Andonova, V. (2017). Synthetic Polymer-Based Nanoparticles: Intelligent Drug Delivery Systems. *Acrylic Polym. Healthc.*
- Balasubramanian, G., Neumann, P., Twitchen, D., Markham, M., Kolesov, R., Mizuochi, N., Isoya, J., Achard, J., Beck, J., Tissler, J., et al. (2009). Ultralong spin coherence time in isotopically engineered diamond. *Nat. Mater.* *8*, 383–387.
- Bashkirov, P.V., Akimov, S.A., Evseev, A.I., Schmid, S.L., Zimmerberg, J., and Frolov, V.A. (2008). GTPase Cycle of Dynamin Is Coupled to Membrane Squeeze and Release, Leading to Spontaneous Fission. *Cell* *135*, 1276–1286.
- Bertrand, J.-R., Pioche-Durieu, C., Ayala, J., Petit, T., Girard, H.A., Malvy, C.P., Le Cam, E., Treussart, F., and Arnault, J.-C. (2015). Plasma hydrogenated cationic detonation nanodiamonds efficiently deliver to human cells in culture functional siRNA targeting the Ewing sarcoma junction oncogene. *Biomaterials* *45*, 93–98.
- Boucrot, E., Howes, M.T., Kirchhausen, T., and Parton, R.G. (2011). Redistribution of caveolae during mitosis. *J Cell Sci* *124*, 1965–1972.
- Boudou, J.-P., Curmi, P.A., Jelezko, F., Wrachtrup, J., Aubert, P., Mohamed Sennour, Balasubramanian, G., Reuter, R., Thorel, A., and Gaffet, E. (2009). High yield fabrication of fluorescent nanodiamonds. *Nanotechnology* *20*, 235602.
- Boyer, C., Priyanto, P., Davis, T.P., Pissuwan, D., Bulmus, V., Kavallaris, M., Teoh, W.Y., Amal, R., Carroll, M., Woodward, R., et al. (2009). Anti-fouling magnetic nanoparticles for siRNA delivery. *J. Mater. Chem.* *20*, 255–265.
- Castan, L., Silva, C.J. da, Molina, E.F., and Santos, R.A. dos (2018). Comparative study of cytotoxicity and genotoxicity of commercial Jeffamines® and polyethylenimine in CHO-K1 cells. *J. Biomed. Mater. Res. B Appl. Biomater.* *106*, 742–750.
- Chan, M.S., Liu, L.S., Leung, H.M., and Lo, P.K. (2017). Cancer-Cell-Specific Mitochondria-Targeted Drug Delivery by Dual-Ligand-Functionalized Nanodiamonds Circumvent Drug Resistance. *ACS Appl. Mater. Interfaces* *9*, 11780–11789.
- Chang, B.-M., Lin, H.-H., Su, L.-J., Lin, W.-D., Lin, R.-J., Tzeng, Y.-K., Lee, R.T., Lee, Y.C., Yu, A.L., and Chang, H.-C. (2013). Highly Fluorescent Nanodiamonds Protein-Functionalized for Cell Labeling and Targeting. *Adv. Funct. Mater.* *23*, 5737–5745.

- Chatterjee, M., Ben-Josef, E., Robb, R., Vedaie, M., Seum, S., Thirumoorthy, K., Palanichamy, K., Harbrecht, M., Chakravarti, A., and Williams, T.M. (2017). Caveolae-Mediated Endocytosis Is Critical for Albumin Cellular Uptake and Response to Albumin-Bound Chemotherapy. *Cancer Res.* *77*, 5925–5937.
- Chu, Z., Zhang, S., Zhang, B., Zhang, C., Fang, C.-Y., Rehor, I., Cigler, P., Chang, H.-C., Lin, G., Liu, R., et al. (2014). Unambiguous observation of shape effects on cellular fate of nanoparticles. *Sci. Rep.* *4*, 4495.
- Chu, Z., Miu, K., Lung, P., Zhang, S., Zhao, S., Chang, H.-C., Lin, G., and Li, Q. (2015). Rapid endosomal escape of prickly nanodiamonds: implications for gene delivery. *Sci. Rep.* *5*, 11661.
- Cocucci, E., Aguet, F., Boulant, S., and Kirchhausen, T. (2012). The First Five Seconds in the Life of a Clathrin-Coated Pit. *Cell* *150*, 495–507.
- Cordina, N.M., Sayyadi, N., Parker, L.M., Everest-Dass, A., Brown, L.J., and Packer, N.H. (2018). Reduced background autofluorescence for cell imaging using nanodiamonds and lanthanide chelates. *Sci. Rep.* *8*, 4521.
- Cunningham, S.L., Maradudin, A.A., and Wallis, R.F. (1974). Effect of a charge layer on the surface-plasmon-polariton dispersion curve. *Phys. Rev. B* *10*, 3342–3355.
- Daumke, O., Roux, A., and Haucke, V. (2014). BAR Domain Scaffolds in Dynamin-Mediated Membrane Fission. *Cell* *156*, 882–892.
- Elbashir, S.M., Harborth, J., Lendeckel, W., Yalcin, A., Weber, K., and Tuschl, T. (2001). Duplexes of 21-nucleotide RNAs mediate RNA interference in cultured mammalian cells. *Nature* *411*, 494–498.
- Faklaris, O., Garrot, D., Treussart, F., Joshi, V., Curmi, P., Boudou, J.-P., and Sauvage, T. (2009). Comparison of the photoluminescence properties of semiconductor quantum dots and non-blinking diamond nanoparticles. Observation of the diffusion of diamond nanoparticles in living cells. *ArXiv Prepr. ArXiv09042648*.
- Faklaris, O., Botsoa, J., Sauvage, T., Roch, J.-F., and Treussart, F. (2010). Photoluminescent nanodiamonds: Comparison of the photoluminescence saturation properties of the NV color center and a cyanine dye at the single emitter level, and study of the color center concentration under different preparation conditions. *Diam. Relat. Mater.* *19*, 988–995.
- Fang, C.-Y., Vijayanthimala, V., Cheng, C.-A., Yeh, S.-H., Chang, C.-F., Li, C.-L., and Chang, H.-C. (2011). The Exocytosis of Fluorescent Nanodiamond and Its Use as a Long-Term Cell Tracker. *Small* *7*, 3363–3370.
- Ford, M.G.J., Mills, I.G., Peter, B.J., Vallis, Y., Praefcke, G.J.K., Evans, P.R., and McMahon, H.T. (2002). Curvature of clathrin-coated pits driven by epsin. *Nature* *419*, 361–366.
- Fotin, A., Cheng, Y., Sliz, P., Grigorieff, N., Harrison, S.C., Kirchhausen, T., and Walz, T. (2004). Molecular model for a complete clathrin lattice from electron cryomicroscopy. *Nature* *432*, 573–579.
- Fox, M.E., Szoka, F.C., and Fréchet, J.M.J. (2009). Soluble Polymer Carriers for the Treatment of Cancer: The Importance of Molecular Architecture. *Acc. Chem. Res.* *42*, 1141–1151.
- Frank-Kamenetsky, M., Grefhorst, A., Anderson, N.N., Racie, T.S., Bramlage, B., Akinc, A., Butler, D., Charisse, K., Dorkin, R., Fan, Y., et al. (2008). Therapeutic RNAi targeting PCSK9 acutely lowers

plasma cholesterol in rodents and LDL cholesterol in nonhuman primates. *Proc. Natl. Acad. Sci. U. S. A.* *105*, 11915–11920.

Garbuzenko, O.B., Winkler, J., Tomassone, M.S., and Minko, T. (2014). Biodegradable Janus Nanoparticles for Local Pulmonary Delivery of Hydrophilic and Hydrophobic Molecules to the Lungs. *Langmuir* *30*, 12941–12949.

Georgatos, S.D., Pyrpasopoulou, A., and Theodoropoulos, P.A. (1997). Nuclear envelope breakdown in mammalian cells involves stepwise lamina disassembly and microtubule-drive deformation of the nuclear membrane. *J. Cell Sci.* *110*, 2129–2140.

Gerion, D., Herberg, J., Bok, R., Gjersing, E., Ramon, E., Maxwell, R., Kurhanewicz, J., Budinger, T.F., Gray, J.W., Shuman, M.A., et al. (2007). Paramagnetic Silica-Coated Nanocrystals as an Advanced MRI Contrast Agent. *J. Phys. Chem. C* *111*, 12542–12551.

Gibson, N., Shenderova, O., Luo, T.J.M., Moseenkov, S., Bondar, V., Puzyr, A., Purtov, K., Fitzgerald, Z., and Brenner, D.W. (2009). Colloidal stability of modified nanodiamond particles. *Diam. Relat. Mater.* *18*, 620–626.

Gilleron, J., Querbes, W., Zeigerer, A., Borodovsky, A., Marsico, G., Schubert, U., Manygoats, K., Seifert, S., Andree, C., Stöter, M., et al. (2013). Image-based analysis of lipid nanoparticle-mediated siRNA delivery, intracellular trafficking and endosomal escape. *Nat. Biotechnol.* *31*, 638–646.

González-Domínguez, I., Cervera, L., Gòdia, F., and Roldán, M. (2019). Quantitative colocalization analysis of DNA delivery by PEI-mediated cationic polymers in mammalian cells. *J. Microsc.* *273*, 53–64.

Goode, B.L., Eskin, J.A., and Wendland, B. (2015). Actin and Endocytosis in Budding Yeast. *Genetics* *199*, 315–358.

Gracio, J.J., Fan, Q.H., and Madaleno, J.C. (2010). Diamond growth by chemical vapour deposition. *J. Phys. Appl. Phys.* *43*, 374017.

Grodzik, M., Sawosz, E., Wierzbicki, M., Orłowski, P., Hotowy, A., Niemiec, T., Szmids, M., Mitura, K., and Chwalibog, A. (2011). Nanoparticles of carbon allotropes inhibit glioblastoma multiforme angiogenesis in ovo. *Int. J. Nanomedicine* *6*, 3041–3048.

Harush-Frenkel, O., Debotton, N., Benita, S., and Altschuler, Y. (2007). Targeting of nanoparticles to the clathrin-mediated endocytic pathway. *Biochem. Biophys. Res. Commun.* *353*, 26–32.

Havlik, J., Petrakova, V., Rehor, I., Petrak, V., Gulka, M., Stursa, J., Kucka, J., Ralis, J., Rendler, T., Lee, S.-Y., et al. (2013). Boosting nanodiamond fluorescence: towards development of brighter probes. *Nanoscale* *5*, 3208–3211.

Havlik, J., Raabova, H., Gulka, M., Petrakova, V., Krecmarova, M., Masek, V., Lousa, P., Stursa, J., Boyen, H.-G., Nesladek, M., et al. (2016). Benchtop Fluorination of Fluorescent Nanodiamonds on a Preparative Scale: Toward Unusually Hydrophilic Bright Particles. *Adv. Funct. Mater.* *26*, 4134–4142.

Havlik, J., Petrakova, V., Kucka, J., Raabova, H., Panek, D., Stepan, V., Cilova, Z.Z., Reineck, P., Stursa, J., Kucera, J., et al. (2018). Extremely rapid isotropic irradiation of nanoparticles with ions generated in situ by a nuclear reaction. *Nat. Commun.* *9*, 4467.

- He, K., Yan, X., Li, N., Dang, S., Xu, L., Zhao, B., Li, Z., Lv, Z., Fang, X., Zhang, Y., et al. (2015). Internalization of the TGF- β type I receptor into caveolin-1 and EEA1 double-positive early endosomes. *Cell Res.* *25*, 738–752.
- He, Y., Zhou, J., Ma, S., Nie, Y., Yue, D., Jiang, Q., Wali, A.R.M., Tang, J.Z., and Gu, Z. (2016). Multi-Responsive “Turn-On” Nanocarriers for Efficient Site-Specific Gene Delivery In Vitro and In Vivo. *Adv. Healthc. Mater.* *5*, 2799–2812.
- Hemelaar, S.R., Nagl, A., Bigot, F., Rodríguez-García, M.M., de Vries, M.P., Chipaux, M., and Schirhagl, R. (2017). The interaction of fluorescent nanodiamond probes with cellular media. *Microchim. Acta* *184*, 1001–1009.
- Hemelaar, S.R., Saspaanithy, B., L’Hommelet, S.R.M., Perona Martinez, F.P., van der Laan, K.J., and Schirhagl, R. (2018). The Response of HeLa Cells to Fluorescent NanoDiamond Uptake. *Sensors* *18*.
- Hinde, E., Thammasiraphop, K., Duong, H.T.T., Yeow, J., Karagoz, B., Boyer, C., Gooding, J.J., and Gaus, K. (2017). Pair correlation microscopy reveals the role of nanoparticle shape in intracellular transport and site of drug release. *Nat. Nanotechnol.* *12*, 81–89.
- Huang, H., Pierstorff, E., Osawa, E., and Ho, D. (2007). Active Nanodiamond Hydrogels for Chemotherapeutic Delivery. *Nano Lett.* *7*, 3305–3314.
- Itaka, K., Yamauchi, K., Harada, A., Nakamura, K., Kawaguchi, H., and Kataoka, K. (2003). Polyion complex micelles from plasmid DNA and poly(ethylene glycol)–poly(l-lysine) block copolymer as serum-tolerable polyplex system: physicochemical properties of micelles relevant to gene transfection efficiency. *Biomaterials* *24*, 4495–4506.
- Jagannadham, K., Verghese, K., and Butler, J.E. (2014). Thermal conductivity changes upon neutron transmutation of 10B doped diamond. *J. Appl. Phys.* *116*, 083706.
- Jana, N.R., Earhart, C., and Ying, J.Y. (2007). Synthesis of Water-Soluble and Functionalized Nanoparticles by Silica Coating. *Chem. Mater.* *19*, 5074–5082.
- Jovic, M., Sharma, M., Rahajeng, J., and Caplan, S. (2010). The early endosome: a busy sorting station for proteins at the crossroads. *Histol. Histopathol.* *25*, 99–112.
- Kadlecova, Z., Spielman, S.J., Loerke, D., Mohanakrishnan, A., Reed, D.K., and Schmid, S.L. (2017). Regulation of clathrin-mediated endocytosis by hierarchical allosteric activation of AP2. *J. Cell Biol.* *216*, 167–179.
- Kaksonen, M., and Roux, A. (2018). Mechanisms of clathrin-mediated endocytosis. *Nat. Rev. Mol. Cell Biol.* *19*, 313–326.
- Kapur, N., Thakral, D., Durgapal, H., and Panda, S.K. (2012). Hepatitis E virus enters liver cells through receptor-dependent clathrin-mediated endocytosis. *J. Viral Hepat.* *19*, 436–448.
- Karlsson, H.L., Cronholm, P., Gustafsson, J., and Möller, L. (2008). Copper Oxide Nanoparticles Are Highly Toxic: A Comparison between Metal Oxide Nanoparticles and Carbon Nanotubes. *Chem. Res. Toxicol.* *21*, 1726–1732.
- Kim, M.-C., Lin, M.M., Sohn, Y., Kim, J.-J., Kang, B.S., and Kim, D.K. (2017). Polyethyleneimine-associated polycaprolactone—Superparamagnetic iron oxide nanoparticles as a gene delivery vector. *J. Biomed. Mater. Res. B Appl. Biomater.* *105*, 145–154.

- Kostan, J., Salzer, U., Orlova, A., Törö, I., Hodnik, V., Senju, Y., Zou, J., Schreiner, C., Steiner, J., Meriläinen, J., et al. (2014). Direct interaction of actin filaments with F-BAR protein paccin2. *EMBO Rep.* *15*, 1154–1162.
- Lee, G.-J., Kim, C.K., Bae, Y., and Rhee, C.K. (2012). Surface modification to improve hydrophobicity of detonation nanodiamond. *J. Nanosci. Nanotechnol.* *12*, 5995–5999.
- Lee, J.-S., Green, J.J., Love, K.T., Sunshine, J., Langer, R., and Anderson, D.G. (2009). Gold, Poly(β -amino ester) Nanoparticles for Small Interfering RNA Delivery. *Nano Lett.* *9*, 2402–2406.
- Liang, Y., Meinhardt, T., Jarre, G., Ozawa, M., Vrdoljak, P., Schöll, A., Reinert, F., and Krueger, A. (2011). Deagglomeration and surface modification of thermally annealed nanoscale diamond. *J. Colloid Interface Sci.* *354*, 23–30.
- Lim, D.G., Prim, R.E., Kim, K.H., Kang, E., Park, K., and Jeong, S.H. (2016). Combinatorial nanodiamond in pharmaceutical and biomedical applications. *Int. J. Pharm.* *514*, 41–51.
- Lin, Y.-C., Wu, K.-T., Lin, Z.-R., Perevedentseva, E., Karmenyan, A., Lin, M.-D., and Cheng, C.-L. (2016). Nanodiamond for biolabelling and toxicity evaluation in the zebrafish embryo in vivo. *J. Biophotonics* *9*, 827–836.
- Lin, Y.-W., Raj, E.N., Liao, W.-S., Lin, J., Liu, K.-K., Chen, T.-H., Cheng, H.-C., Wang, C.-C., Li, L.Y., Chen, C., et al. (2017). Co-delivery of paclitaxel and cetuximab by nanodiamond enhances mitotic catastrophe and tumor inhibition. *Sci. Rep.* *7*, 9814.
- Liu, J., Valencia-Sanchez, M.A., Hannon, G.J., and Parker, R. (2005). MicroRNA-dependent localization of targeted mRNAs to mammalian P-bodies. *Nat. Cell Biol.* *7*, 719–723.
- Liu, L., Brown, D., McKee, M., LeBrasseur, N.K., Yang, D., Albrecht, K.H., Ravid, K., and Pilch, P.F. (2008). Deletion of Cavin/PTRF causes global loss of caveolae, dyslipidemia and glucose intolerance. *Cell Metab.* *8*, 310–317.
- Livak, K.J., and Schmittgen, T.D. (2001). Analysis of relative gene expression data using real-time quantitative PCR and the 2⁻($\Delta\Delta C_T$) Method. *Methods San Diego Calif* *25*, 402–408.
- Macia, E., Ehrlich, M., Massol, R., Boucrot, E., Brunner, C., and Kirchhausen, T. (2006). Dynasore, a Cell-Permeable Inhibitor of Dynamin. *Dev. Cell* *10*, 839–850.
- Maeda, H. (2001). The enhanced permeability and retention (EPR) effect in tumor vasculature: the key role of tumor-selective macromolecular drug targeting. *Adv. Enzyme Regul.* *41*, 189–207.
- Maeda, H., Nakamura, H., and Fang, J. (2013). The EPR effect for macromolecular drug delivery to solid tumors: Improvement of tumor uptake, lowering of systemic toxicity, and distinct tumor imaging in vivo. *Adv. Drug Deliv. Rev.* *65*, 71–79.
- Marcon, L., Riquet, F., Vicogne, D., Szunerits, S., Bodart, J.-F., and Boukherroub, R. (2010). Cellular and in vivo toxicity of functionalized nanodiamond in *Xenopus* embryos. *J. Mater. Chem.* *20*, 8064–8069.
- Matsumura, Y., and Maeda, H. (1986). A New Concept for Macromolecular Therapeutics in Cancer Chemotherapy: Mechanism of Tumorotropic Accumulation of Proteins and the Antitumor Agent Smancs. *Cancer Res.* *46*, 6387–6392.
- McCaffrey, A.P., Meuse, L., Pham, T.-T.T., Conklin, D.S., Hannon, G.J., and Kay, M.A. (2002). RNA interference in adult mice. *Nature* *418*, 38.

- Meister, G., Landthaler, M., Patkaniowska, A., Dorsett, Y., Teng, G., and Tuschl, T. (2004). Human Argonaute2 Mediates RNA Cleavage Targeted by miRNAs and siRNAs. *Mol. Cell* *15*, 185–197.
- Miller, S.E., Mathiasen, S., Bright, N.A., Pierre, F., Kelly, B.T., Kladt, N., Schauss, A., Merrifield, C.J., Stamou, D., Höning, S., et al. (2015). CALM Regulates Clathrin-Coated Vesicle Size and Maturation by Directly Sensing and Driving Membrane Curvature. *Dev. Cell* *33*, 163–175.
- Mochalin, V.N., Shenderova, O., Ho, D., and Gogotsi, Y. (2012). The properties and applications of nanodiamonds. *Nat. Nanotechnol.* *7*, 11–23.
- Moore, L., Yang, J., Lan, T.T.H., Osawa, E., Lee, D.-K., Johnson, W.D., Xi, J., Chow, E.K.-H., and Ho, D. (2016). Biocompatibility Assessment of Detonation Nanodiamond in Non-Human Primates and Rats Using Histological, Hematologic, and Urine Analysis. *ACS Nano* *10*, 7385–7400.
- Neburkova, J., Hajek, M., Rehor, I., Schimer, J., Sedlak, F., Stursa, J., Hruby, M., and Cigler, P. (2018). Targeting Glioma Cancer Cells with Fluorescent Nanodiamonds via Integrin Receptors. In *Integrin Targeting Systems for Tumor Diagnosis and Therapy*, E. Patsenker, ed. (New York, NY: Springer New York), pp. 169–189.
- Nichols, J.W., and Bae, Y.H. (2014). EPR: Evidence and fallacy. *J. Controlled Release* *190*, 451–464.
- Nöbauer, T., Buczak, K., Angerer, A., Putz, S., Steinhauser, G., Akbarzadeh, J., Peterlik, H., Majer, J., Schmiedmayer, J., and Trupke, M. (2013). Creation of ensembles of nitrogen-vacancy centers in diamond by neutron and electron irradiation. *ArXiv Prepr. ArXiv13090453*.
- Pelkmans, L., Bürli, T., Zerial, M., and Helenius, A. (2004). Caveolin-stabilized membrane domains as multifunctional transport and sorting devices in endocytic membrane traffic. *Cell* *118*, 767–780.
- Petrakova, V., Rehor, I., Stursa, J., Ledvina, M., Nesladek, M., and Cigler, P. (2015). Charge-sensitive fluorescent nanosensors created from nanodiamonds. *Nanoscale* *7*, 12307–12311.
- Petrakova, V., Benson, V., Buncek, M., Fiserova, A., Ledvina, M., Stursa, J., Cigler, P., and Nesladek, M. (2016). Imaging of transfection and intracellular release of intact, non-labeled DNA using fluorescent nanodiamonds. *Nanoscale* *8*, 12002–12012.
- Petros, R.A., and DeSimone, J.M. (2010). Strategies in the design of nanoparticles for therapeutic applications. *Nat. Rev. Drug Discov.* *9*, 615–627.
- Phadke, M.S., Krynetskaia, N.F., Mishra, A.K., and Krynetskiy, E. (2009). Glyceraldehyde 3-Phosphate Dehydrogenase Depletion Induces Cell Cycle Arrest and Resistance to Antimetabolites in Human Carcinoma Cell Lines. *J. Pharmacol. Exp. Ther.* *331*, 77–86.
- Pham, M.D., Epperla, C.P., Hsieh, C.-L., Chang, W., and Chang, H.-C. (2017). Glycosaminoglycans-Specific Cell Targeting and Imaging Using Fluorescent Nanodiamonds Coated with Viral Envelope Proteins. *Anal. Chem.* *89*, 6527–6534.
- Pichot, V., Comet, M., Fousson, E., Baras, C., Senger, A., Le Normand, F., and Spitzer, D. (2008). An efficient purification method for detonation nanodiamonds. *Diam. Relat. Mater.* *17*, 13–22.
- Prabhakar, N., Khan, M.H., Peurla, M., Chang, H.-C., Hänninen, P.E., and Rosenholm, J.M. (2017). Intracellular Trafficking of Fluorescent Nanodiamonds and Regulation of Their Cellular Toxicity. *ACS Omega* *2*, 2689–2693.

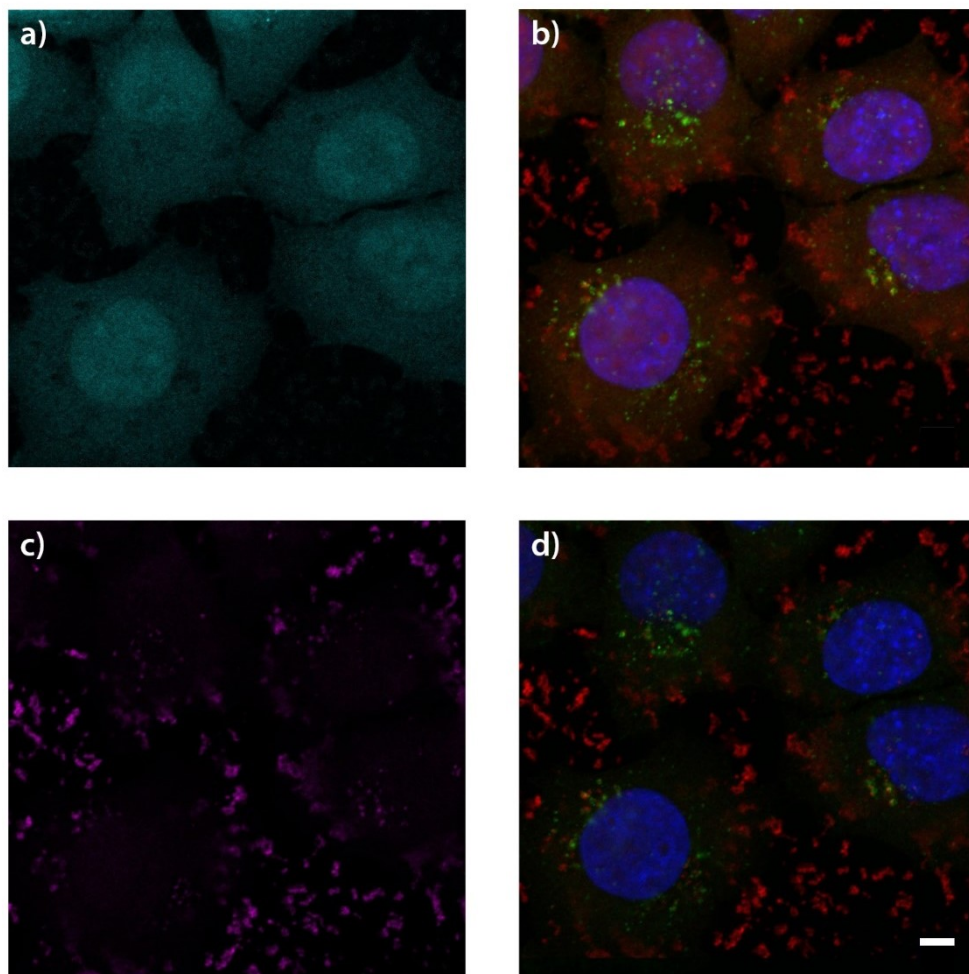
- Rao, A.M., Eklund, P.C., Bandow, S., Thess, A., and Smalley, R.E. (1997). Evidence for charge transfer in doped carbon nanotube bundles from Raman scattering. *Nature* 388, 257–259.
- Rausch, V., Bostrom, J.R., Park, J., Bravo, I.R., Feng, Y., Hay, D.C., Link, B.A., and Hansen, C.G. (2019). The Hippo Pathway Regulates Caveolae Expression and Mediates Flow Response via Caveolae. *Curr. Biol.* 29, 242-255.e6.
- Rehor, I., Mackova, H., Filippov, S.K., Kucka, J., Proks, V., Slegerova, J., Turner, S., Van Tendeloo, G., Ledvina, M., Hruby, M., et al. (2014). Fluorescent Nanodiamonds with Bioorthogonally Reactive Protein-Resistant Polymeric Coatings. *ChemPlusChem* 79, 21–24.
- Reubold, T.F., Faelber, K., Plattner, N., Posor, Y., Ketel, K., Curth, U., Schlegel, J., Anand, R., Manstein, D.J., Noé, F., et al. (2015). Crystal structure of the dynamin tetramer. *Nature* 525, 404–408.
- Rim, K.-T., Song, S.-W., and Kim, H.-Y. (2013). Oxidative DNA Damage from Nanoparticle Exposure and Its Application to Workers' Health: A Literature Review. *Saf. Health Work* 4, 177–186.
- Rodal, S.K., Skretting, G., Garred, Ø., Vilhardt, F., Deurs, B. van, and Sandvig, K. (1999). Extraction of Cholesterol with Methyl- β -Cyclodextrin Perturbs Formation of Clathrin-coated Endocytic Vesicles. *Mol. Biol. Cell* 10, 961–974.
- Roh, J., Sim, S.J., Yi, J., Park, K., Chung, K.H., Ryu, D., and Choi, J. (2009). Ecotoxicity of Silver Nanoparticles on the Soil Nematode *Caenorhabditis elegans* Using Functional Ecotoxicogenomics. *Environ. Sci. Technol.* 43, 3933–3940.
- Rojas, S., Gispert, J.D., Martín, R., Abad, S., Menchón, C., Pareto, D., Víctor, V.M., Álvaro, M., García, H., and Herance, J.R. (2011). Biodistribution of Amino-Functionalized Diamond Nanoparticles. In Vivo Studies Based on ^{18}F Radionuclide Emission. *ACS Nano* 5, 5552–5559.
- Roth, T.F., and Porter, K.R. (1964). Yolk Protein Uptake in the Oocyte of the Mosquito *Aedes Aegypti*. *L. J. Cell Biol.* 20, 313–332.
- Roy, I., Ohulchansky, T.Y., Bharali, D.J., Pudavar, H.E., Mistretta, R.A., Kaur, N., and Prasad, P.N. (2005). Optical tracking of organically modified silica nanoparticles as DNA carriers: A nonviral, nanomedicine approach for gene delivery. *Proc. Natl. Acad. Sci.* 102, 279–284.
- Rubio, A.S. (2015). *Modified Au-Based Nanomaterials Studied by Surface Plasmon Resonance Spectroscopy* (Springer International Publishing).
- Ryu, T.-K., Baek, S.W., Lee, G.-J., Rhee, C.-K., and Choi, S.-W. (2017). Targeted Tumor Therapy Based on Nanodiamonds Decorated with Doxorubicin and Folic Acid. *Macromol. Biosci.* 17, 1600180.
- Schnitzer, J.E., Oh, P., Pinney, E., and Allard, J. (1994). Filipin-sensitive caveolae-mediated transport in endothelium: reduced transcytosis, scavenger endocytosis, and capillary permeability of select macromolecules. *J. Cell Biol.* 127, 1217–1232.
- Schrand, A.M., Huang, H., Carlson, C., Schlager, J.J., Ōsawa, E., Hussain, S.M., and Dai, L. (2007). Are Diamond Nanoparticles Cytotoxic? *J. Phys. Chem. B* 111, 2–7.
- Schrand, A.M., Hens, S.A.C., and Shenderova, O.A. (2009). Nanodiamond Particles: Properties and Perspectives for Bioapplications. *Crit. Rev. Solid State Mater. Sci.* 34, 18–74.

- Schrand, A.M., Lin, J.B., Hens, S.C., and Hussain, S.M. (2011). Temporal and mechanistic tracking of cellular uptake dynamics with novel surface fluorophore-bound nanodiamonds. *Nanoscale* *3*, 435–445.
- Seemann, E., Sun, M., Krueger, S., Tröger, J., Hou, W., Haag, N., Schüler, S., Westermann, M., Huebner, C.A., Romeike, B., et al. (2017). Deciphering caveolar functions by syndapin III KO-mediated impairment of caveolar invagination. *ELife* *6*, e29854.
- Senju, Y., Itoh, Y., Takano, K., Hamada, S., and Suetsugu, S. (2011). Essential role of PACSIN2/syndapin-II in caveolae membrane sculpting. *J Cell Sci* *124*, 2032–2040.
- Setyawati, M.I., Mochalin, V.N., and Leong, D.T. (2016). Tuning Endothelial Permeability with Functionalized Nanodiamonds. *ACS Nano* *10*, 1170–1181.
- Shah, M., Bourner, L., Ali, S., Al-Enazy, S., and Rytting, E. (2017). Cytotoxicity of Endocytosis and Efflux Inhibitors in the BeWo Cell Line. *J. Pharm. Res. Int.* *17*.
- Shenderova, O., Petrov, I., Walsh, J., Grichko, V., Grishko, V., Tyler, T., and Cunningham, G. (2006a). Modification of detonation nanodiamonds by heat treatment in air. *Diam. Relat. Mater.* *15*, 1799–1803.
- Shenderova, O. A., Zhirnov, V. V., Brenner, D. W. (2002) Carbon Nanostructures, *Critical Reviews in Solid State and Materials Sciences*, *27*:3-4, 227-356
- Shvets, E., Bitsikas, V., Howard, G., Hansen, C.G., and Nichols, B.J. (2015). Dynamic caveolae exclude bulk membrane proteins and are required for sorting of excess glycosphingolipids. *Nat. Commun.* *6*.
- Slowing, I.I., Vivero-Escoto, J.L., Wu, C.-W., and Lin, V.S.-Y. (2008). Mesoporous silica nanoparticles as controlled release drug delivery and gene transfection carriers. *Adv. Drug Deliv. Rev.* *60*, 1278–1288.
- Solarska, K., Gajewska, A., Kaczorowski, W., Bartosz, G., and Mitura, K. (2012). Effect of nanodiamond powders on the viability and production of reactive oxygen and nitrogen species by human endothelial cells. *Diam. Relat. Mater.* *21*, 107–113.
- Spagnou, S., Miller, A.D., and Keller, M. (2004). Lipidic Carriers of siRNA: Differences in the Formulation, Cellular Uptake, and Delivery with Plasmid DNA. *Biochemistry* *43*, 13348–13356.
- Stehlik, S., Varga, M., Ledinsky, M., Jirasek, V., Artemenko, A., Kozak, H., Ondic, L., Skakalova, V., Argentero, G., Pennycook, T., et al. (2015). Size and Purity Control of HPHT Nanodiamonds down to 1 nm. *J. Phys. Chem. C Nanomater. Interfaces* *119*, 27708–27720.
- Stoeber, M., Stoeck, I.K., Hänni, C., Bleck, C.K.E., Balistreri, G., and Helenius, A. (2012). Oligomers of the ATPase EHD2 confine caveolae to the plasma membrane through association with actin. *EMBO J.* *31*, 2350–2364.
- Stursa, J., Havlik, J., Petrakova, V., Gulka, M., Ralis, J., Zach, V., Pulec, Z., Stepan, V., Zargaleh, S.A., Ledvina, M., et al. (2016). Mass production of fluorescent nanodiamonds with a narrow emission intensity distribution. *Carbon* *96*, 812–818.
- Sun, Y., Martin, A.C., and Drubin, D.G. (2006). Endocytic Internalization in Budding Yeast Requires Coordinated Actin Nucleation and Myosin Motor Activity. *Dev. Cell* *11*, 33–46.

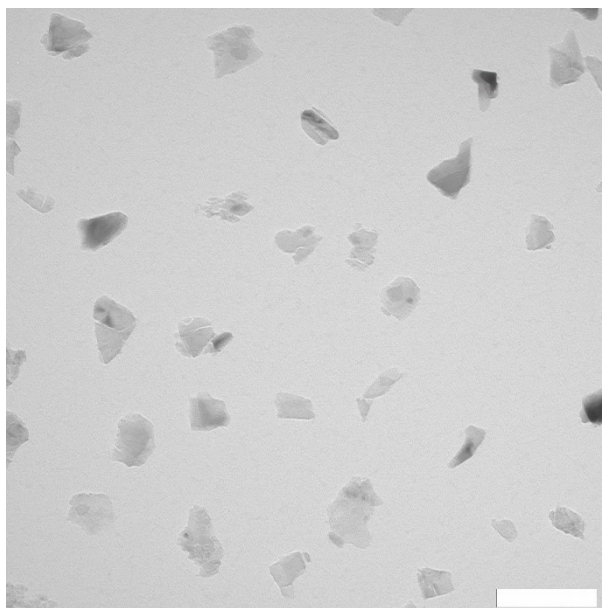
- Sweitzer, S.M., and Hinshaw, J.E. (1998). Dynamin Undergoes a GTP-Dependent Conformational Change Causing Vesiculation. *Cell* 93, 1021–1029.
- Thomsen, P., Roepstorff, K., Stahlhut, M., and van Deurs, B. (2002). Caveolae Are Highly Immobile Plasma Membrane Microdomains, Which Are not Involved in Constitutive Endocytic Trafficking. *Mol. Biol. Cell* 13, 238–250.
- Tinwala, H., and Wairkar, S. (2019). Production, surface modification and biomedical applications of nanodiamonds: A sparkling tool for theranostics. *Mater. Sci. Eng. C* 97, 913–931.
- Tsai, L.-W., Lin, Y.-C., Perevedentseva, E., Lugovtsov, A., Priezzhev, A., and Cheng, C.-L. (2016). Nanodiamonds for Medical Applications: Interaction with Blood in Vitro and in Vivo. *Int. J. Mol. Sci.* 17, 1111.
- Turcheniuk, K., and Mochalin, V.N. (2017). Biomedical applications of nanodiamond (Review). *Nanotechnology* 28, 252001.
- Vaijayanthimala, V., Tzeng, Y.-K., Chang, H.-C., and Li, C.-L. (2009). The biocompatibility of fluorescent nanodiamonds and their mechanism of cellular uptake. *Nanotechnology* 20, 425103.
- Vaijayanthimala, V., Cheng, P.-Y., Yeh, S.-H., Liu, K.-K., Hsiao, C.-H., Chao, J.-I., and Chang, H.-C. (2012). The long-term stability and biocompatibility of fluorescent nanodiamond as an in vivo contrast agent. *Biomaterials* 33, 7794–7802.
- Waldermann, F.C., Olivero, P., Nunn, J., Surmacz, K., Wang, Z.Y., Jaksch, D., Taylor, R.A., Walmsley, I.A., Draganski, M., Reichart, P., et al. (2007). Creating diamond color centers for quantum optical applications. *Diam. Relat. Mater.* 16, 1887–1895.
- Wang, Z., Tirupathi, C., Minshall, R.D., and Malik, A.B. (2009). Size and Dynamics of Caveolae Studied Using Nanoparticles in Living Endothelial Cells. *ACS Nano* 3, 4110–4116.
- Wang, Z., Tian, Z., Dong, Y., Li, L., Tian, L., Li, Y., and Yang, B. (2015). Nanodiamond-conjugated transferrin as chemotherapeutic drug delivery. *Diam. Relat. Mater.* 58, 84–93.
- Wee, T.-L., Tzeng, Y.-K., Han, C.-C., Chang, H.-C., Fann, W., Hsu, J.-H., Chen, K.-M., and Yu, Y.-C. (2007). Two-photon Excited Fluorescence of Nitrogen-Vacancy Centers in Proton-Irradiated Type Ib Diamond †. *J. Phys. Chem. A* 111, 9379–9386.
- West, M.A., Bretscher, M.S., and Watts, C. (1989). Distinct endocytotic pathways in epidermal growth factor-stimulated human carcinoma A431 cells. *J. Cell Biol.* 109, 2731–2739.
- Wierzbicki, M., Sawosz, E., Grodzik, M., Hotowy, A., Prasek, M., Jaworski, S., Sawosz, F., and Chwalibog, A. (2013). Carbon nanoparticles downregulate expression of basic fibroblast growth factor in the heart during embryogenesis. *Int. J. Nanomedicine* 8, 3427–3435.
- Wierzbicki, M., Jaworski, S., Kutwin, M., Grodzik, M., Strojny, B., Kurantowicz, N., Zdunek, K., Chodun, R., Chwalibog, A., and Sawosz, E. (2017). Diamond, graphite, and graphene oxide nanoparticles decrease migration and invasiveness in glioblastoma cell lines by impairing extracellular adhesion. *Int. J. Nanomedicine* 12, 7241–7254.
- Wilhelm, S., Tavares, A.J., Dai, Q., Ohta, S., Audet, J., Dvorak, H.F., and Chan, W.C.W. (2016). Analysis of nanoparticle delivery to tumours. *Nat. Rev. Mater.* 1, 16014.
- Xing, Y., Xiong, W., Zhu, L., Ōsawa, E., Hussin, S., and Dai, L. (2011). DNA Damage in Embryonic Stem Cells Caused by Nanodiamonds. *ACS Nano* 5, 2376–2384.

- Yamano, S., Dai, J., and Moursi, A.M. (2010). Comparison of Transfection Efficiency of Nonviral Gene Transfer Reagents. *Mol. Biotechnol.* *46*, 287–300.
- Yeow, I., Howard, G., Chadwick, J., Mendoza-Topaz, C., Hansen, C.G., Nichols, B.J., and Shvets, E. (2017). EHD Proteins Cooperate to Generate Caveolar Clusters and to Maintain Caveolae during Repeated Mechanical Stress. *Curr. Biol.* *27*, 2951-2962.e5.
- Yuan, Y., Wang, X., Jia, G., Liu, J.-H., Wang, T., Gu, Y., Yang, S.-T., Zhen, S., Wang, H., and Liu, Y. (2010). Pulmonary toxicity and translocation of nanodiamonds in mice. *Diam. Relat. Mater.* *19*, 291–299.
- Zhang, L.W., and Monteiro-Riviere, N.A. (2009). Mechanisms of Quantum Dot Nanoparticle Cellular Uptake. *Toxicol. Sci.* *110*, 138–155.
- Zhang, B., Feng, X., Yin, H., Ge, Z., Wang, Y., Chu, Z., Raabova, H., Vavra, J., Cigler, P., Liu, R., et al. (2017). Anchored but not internalized: shape dependent endocytosis of nanodiamond. *Sci. Rep.* *7*, 46462.
- Zhang, T., Cui, H., Fang, C.-Y., Cheng, K., Yang, X., Chang, H.-C., and Forrest, M.L. (2015). Targeted nanodiamonds as phenotype-specific photoacoustic contrast agents for breast cancer. *Nanomed.* *10*, 573–587.
- Zhang, X., Hu, W., Li, J., Tao, L., and Wei, Y. (2012). A comparative study of cellular uptake and cytotoxicity of multi-walled carbon nanotubes, graphene oxide, and nanodiamond. *Toxicol. Res.* *1*, 62–68.
- Zhao, L., Xu, Y.-H., Akasaka, T., Abe, S., Komatsu, N., Watari, F., and Chen, X. (2014). Polyglycerol-coated nanodiamond as a macrophage-evading platform for selective drug delivery in cancer cells. *Biomaterials* *35*, 5393–5406.
- Zhao, W., Wei, S., Zhao, H., Li, Y., Wu, R., and Wang, J. (2017). Enhanced anticancer activity of an intracellularly activatable nanomedicine based on GLYlated nanodiamond. *Diam. Relat. Mater.* *77*, 171–180.
- Zheng, T., Perona Martínez, F., Storm, I.M., Rombouts, W., Sprakel, J., Schirhagl, R., and de Vries, R. (2017). Recombinant Protein Polymers for Colloidal Stabilization and Improvement of Cellular Uptake of Diamond Nanosensors. *Anal. Chem.* *89*, 12812–12820.

8. SUPPLEMENTARY DATA



Supplementary fig. 1: Linear unmixing. a) Residual channel which during regular scan (b) contains for example cells' autofluorescence in red part of light spectrum. c) Channel with only ND signal. d) Final image, after discarding of residual channel. White scale bar equals 5 μm .



Supplementary fig. 2: TEM image of NDs before polymerization. Kindly provided by Marek Kindermann from P. Cigler group at IOCB, CAS.

Supplementary script 1:

```
function uprav() {
//naming
//priprava hyperstacku
nI=nImages;
closeChannel=newArray(nI);
for (i=1; i<=nI; i++) {
    selectImage(i);
    closeChannel[i-1]=getTitle();
}

if (nI==8) {
    selectImage(closeChannel[6]); close();
    selectImage(closeChannel[4]); close();
    selectImage(closeChannel[1]); close();
    run("Merge Channels...", "c1=["+closeChannel[3]+"]
c2=["+closeChannel[2]+"] c3=["+closeChannel[0]+"] c4=["+closeChannel[7]+"]
c5=["+closeChannel[5]+"] create ignore");
}

if (nI==7) {
    selectImage(closeChannel[4]); close();
    selectImage(closeChannel[1]); close();
}
```

```

        run("Merge Channels...", "c1=["+closeChannel[3]+"
c2=["+closeChannel[2]+" c3=["+closeChannel[0]+" c4=["+closeChannel[6]+"
c5=["+closeChannel[5]+" create ignore");
    }

    if (nI==6) {
        selectImage(closeChannel[1]); close();
        selectImage(closeChannel[4]); close();
        run("Merge Channels...", "c1=["+closeChannel[3]+"
c2=["+closeChannel[2]+" c3=["+closeChannel[0]+" c4=["+closeChannel[5]+"
create ignore");
    }

//contrast
Stack.getDimensions(width, height, channels, slices, frames);
Stack.setSlice(slices/2);
Stack.setDisplayMode("color");
for (c=1; c<=channels; c++) {
    Stack.setChannel(c);
    if (c==1) setMinAndMax(0, 20500);
    else if (c==2) setMinAndMax(0, 16500);
    else if (c==3) setMinAndMax(0, 9200);
    else resetMinAndMax;
}
Stack.setDisplayMode("composite");
}

```

Supplementary script 2:

```

function FindEdges() {
// Split channels
run("Split Channels");
selectWindow("C4-"+file[f]);
run("Duplicate...", " ");

//subtract background
//run("Subtract Background...", "rolling=100 sliding disable");

// based on original article
run("Enhance Contrast...", "saturated=0 equalize");
// Canny edge detection
run("Canny Edge Detector", "gaussian = 1.75 low=0.1 high=8");
run("Maximum...", "radius=5");
run("Options...", "iterations=10 count=3 black pad edm=Overwrite
do=Close");
    run("Options...", "iterations=20 count=3 black pad edm=Overwrite
do=Open");
}

```

```

}

function FindCellEdgeInRed(){
//run("Split Channels");
selectwindow("C1-"+file[f]);
run("Duplicate...", " ");
run("Make Binary");
run("Maximum...", "radius=1");
run("Options...", "iterations=10 count=3 black pad do=Close");
run("Invert LUT");
run("Fill Holes");
run("Convert to Mask");
if (roiManager("count")>0){
    run("Select All");
    roiManager("Deselect");
    roiManager("Delete")}
run("Analyze Particles...", "size=0-Infinity pixel show=Nothing add");
if (roiManager("count")>1){
    Area=newArray(roiManager("count"));
    AreaLargest = 0;
    for (i=0; i<roiManager("count");i++){
        roiManager("select", i);
        getStatistics(Area[i]);
        if (Area[i]>AreaLargest){
            AreaLargest=Area[i];
            largest = i;
        }
    }
}
roiManager("select", largest)
run("Clear Outside");
}

function FindCellEdgeInGreen(){
//run("Split Channels");
selectwindow("C2-"+file[f]);
run("Duplicate...", " ");
run("Make Binary");
run("Options...", "iterations=10 count=5 black pad do=Erode");
run("Maximum...", "radius=5");
run("Options...", "iterations=20 count=3 black pad do=Close");
run("Fill Holes");
run("Convert to Mask");
if (roiManager("count")>0){
    run("Select All");
    roiManager("Deselect");
    roiManager("Delete")}
}

```

```
run("Analyze Particles...", "size=0-Infinity pixel show=Nothing add");
if (roiManager("count")>1){
    Area=newArray(roiManager("count"));
    AreaLargest = 0;
    for (i=0; i<roiManager("count");i++){
        roiManager("select", i);
        getStatistics(Area[i]);
        if (Area[i]>AreaLargest){
            AreaLargest=Area[i];
            largest = i;
        }
    }
}
roiManager("select", largest)
run("Clear Outside");
}
```